



AD _____

GRANT NO: DAMD17-94-J-4133

TITLE: A Study of Ultrasonic Wavefront Distortion Compensation

PRINCIPAL INVESTIGATOR(S): Qing Zhu, Ph.D.

CONTRACTING ORGANIZATION: University of Pennsylvania
Philadelphia, Pennsylvania
19104-3246

REPORT DATE: September 1995

TYPE OF REPORT: Annual

PREPARED FOR: Commander
U.S. Army Medical Research and Materiel Command
Fort Detrick, Maryland 21702-5012

DISTRIBUTION STATEMENT: Approved for public release;
distribution unlimited

The views, opinions and/or findings contained in this report are those of the author(s) and should not be construed as an official Department of the Army position, policy or decision unless so designated by other documentation.

19951211 098

DTIC QUALITY INSPECTED 1

REPORT DOCUMENTATION PAGE			Form Approved OMB No. 0704-0188	
Public reporting burden for this collection of information is estimated to average 1 hour per response, including the time for reviewing instructions, searching existing data sources, gathering and maintaining the data needed, and completing and reviewing the collection of information. Send comments regarding this burden estimate or any other aspect of this collection of information, including suggestions for reducing this burden, to Washington Headquarters Services, Directorate for Information Operations and Reports, 1215 Jefferson Davis Highway, Suite 1204, Arlington, VA 22202-4302, and to the Office of Management and Budget, Paperwork Reduction Project (0704-0188), Washington, DC 20503.				
1. AGENCY USE ONLY (Leave blank)		2. REPORT DATE September 1995		3. REPORT TYPE AND DATES COVERED Annual (9/1/94-8/31/95)
4. TITLE AND SUBTITLE A Study of Ultrasonic Wavefront Distortion Compensation			5. FUNDING NUMBERS DAMD17-94-J-4133	
6. AUTHOR(S) Qing Zhu, Ph.D.				
7. PERFORMING ORGANIZATION NAME(S) AND ADDRESS(ES) University of Pennsylvania Philadelphia, Pennsylvania 19104-3246			8. PERFORMING ORGANIZATION REPORT NUMBER	
9. SPONSORING / MONITORING AGENCY NAME(S) AND ADDRESS(ES) U.S. Army Medical Research and Materiel Command Fort Detrick, Maryland 21702-5012			10. SPONSORING / MONITORING AGENCY REPORT NUMBER	
11. SUPPLEMENTARY NOTES				
12a. DISTRIBUTION / AVAILABILITY STATEMENT Approved for public release; distribution unlimited			12b. DISTRIBUTION CODE	
13. ABSTRACT (Maximum 200 words) The requirement for higher ultrasound resolution needed for early detection of breast tumors is to compensate distorted ultrasonic wavefronts. We have found that two types of algorithms are necessary to fully deaberrate ultrasonic waves in breast. One is a global algorithm for isotropic scattering, an example of which is time delay correction (TDC). In the last year we found that applying TDC type algorithms to <i>in vitro</i> breast data suppressed scattered energy and folded it into the target image, increasing contrast resolution by 10-15 dB. Recently, we have discovered that amplitude compression in addition to phase deaberration (App.A), is akin to inverse filter, improves contrast resolution to 10 dB more than that of TDC type algorithms, and 5 dB more than that of backpropagation and phase deaberration. Preliminary studies also show that diverse images obtained from different spatial locations of a large 2-D aperture are likely to provide the identification information of true targets vs. image artifacts. Once the real targets are identified, nonlinear deconvolution techniques and interference cancellation techniques are applicable to reconstruct the refractive artifact-free scene or to cancel image artifacts. The initial results are encouraging.				
14. SUBJECT TERMS Ultrasound, wavefront compensation, signal processing Breast Cancer			15. NUMBER OF PAGES 79	
			16. PRICE CODE	
17. SECURITY CLASSIFICATION OF REPORT Unclassified	18. SECURITY CLASSIFICATION OF THIS PAGE Unclassified	19. SECURITY CLASSIFICATION OF ABSTRACT Unclassified	20. LIMITATION OF ABSTRACT Unlimited	

GENERAL INSTRUCTIONS FOR COMPLETING SF 298

The Report Documentation Page (RDP) is used in announcing and cataloging reports. It is important that this information be consistent with the rest of the report, particularly the cover and title page. Instructions for filling in each block of the form follow. It is important to *stay within the lines* to meet *optical scanning requirements*.

Block 1. Agency Use Only (Leave blank).

Block 2. Report Date. Full publication date including day, month, and year, if available (e.g. 1 Jan 88). Must cite at least the year.

Block 3. Type of Report and Dates Covered. State whether report is interim, final, etc. If applicable, enter inclusive report dates (e.g. 10 Jun 87 - 30 Jun 88).

Block 4. Title and Subtitle. A title is taken from the part of the report that provides the most meaningful and complete information. When a report is prepared in more than one volume, repeat the primary title, add volume number, and include subtitle for the specific volume. On classified documents enter the title classification in parentheses.

Block 5. Funding Numbers. To include contract and grant numbers; may include program element number(s), project number(s), task number(s), and work unit number(s). Use the following labels:

C - Contract	PR - Project
G - Grant	TA - Task
PE - Program Element	WU - Work Unit Accession No.

Block 6. Author(s). Name(s) of person(s) responsible for writing the report, performing the research, or credited with the content of the report. If editor or compiler, this should follow the name(s).

Block 7. Performing Organization Name(s) and Address(es). Self-explanatory.

Block 8. Performing Organization Report Number. Enter the unique alphanumeric report number(s) assigned by the organization performing the report.

Block 9. Sponsoring/Monitoring Agency Name(s) and Address(es). Self-explanatory.

Block 10. Sponsoring/Monitoring Agency Report Number. (If known)

Block 11. Supplementary Notes. Enter information not included elsewhere such as: Prepared in cooperation with...; Trans. of...; To be published in.... When a report is revised, include a statement whether the new report supersedes or supplements the older report.

Block 12a. Distribution/Availability Statement. Denotes public availability or limitations. Cite any availability to the public. Enter additional limitations or special markings in all capitals (e.g. NOFORN, REL, ITAR).

DOD - See DoDD 5230.24, "Distribution Statements on Technical Documents."

DOE - See authorities.

NASA - See Handbook NHB 2200.2.

NTIS - Leave blank.

Block 12b. Distribution Code.

DOD - Leave blank.

DOE - Enter DOE distribution categories from the Standard Distribution for Unclassified Scientific and Technical Reports.

NASA - Leave blank.

NTIS - Leave blank.

Block 13. Abstract. Include a brief (*Maximum 200 words*) factual summary of the most significant information contained in the report.

Block 14. Subject Terms. Keywords or phrases identifying major subjects in the report.

Block 15. Number of Pages. Enter the total number of pages.

Block 16. Price Code. Enter appropriate price code (*NTIS only*).

Blocks 17. - 19. Security Classifications. Self-explanatory. Enter U.S. Security Classification in accordance with U.S. Security Regulations (i.e., UNCLASSIFIED). If form contains classified information, stamp classification on the top and bottom of the page.

Block 20. Limitation of Abstract. This block must be completed to assign a limitation to the abstract. Enter either UL (unlimited) or SAR (same as report). An entry in this block is necessary if the abstract is to be limited. If blank, the abstract is assumed to be unlimited.

FOREWORD

Opinions, interpretations, conclusions and recommendations are those of the author and are not necessarily endorsed by the US Army.

Where copyrighted material is quoted, permission has been obtained to use such material.

Where material from documents designated for limited distribution is quoted, permission has been obtained to use the material.

Citations of commercial organizations and trade names in this report do not constitute an official Department of Army endorsement or approval of the products or services of these organizations.

In conducting research using animals, the investigator(s) adhered to the "Guide for the Care and Use of Laboratory Animals," prepared by the Committee on Care and Use of Laboratory Animals of the Institute of Laboratory Resources, National Research Council. (NIH Publication No. 86-23, Revised 1985).


For the protection of human subjects, the investigator(s) adhered to policies of applicable Federal Law 45 CFR 46.

In conducting research utilizing recombinant DNA technology, the investigator(s) adhered to current guidelines promulgated by the National Institutes of Health.

In the conduct of research utilizing recombinant DNA, the investigator(s) adhered to the NIH Guidelines for Research Involving Recombinant DNA Molecules.

In the conduct of research involving hazardous organisms, the investigator(s) adhered to the CDC-NIH Guide for Biosafety in Microbiological and Biomedical Laboratories.

Accession For	
NTIS CRA&I	<input checked="checked" type="checkbox"/>
DTIC TAB	<input type="checkbox"/>
Unannounced	<input type="checkbox"/>
Justification	
By	
Distribution/	
Availability Codes	
Dist	Avail and/or Special
A-1	

 9/28/95
PI - Signature Date

1 INTRODUCTION.....	1
2. EXPERIMENTS AND RESULTS.....	2
2.1 EXPERIMENTS.....	2
2.2 EXPERIMENTAL RESULTS	2
2.2.1. MODELLING OF SCATTERING.....	2
2.2.2. MODELLING OF SCATTERING AND REFRACTION.....	5
2.2.3. CORRECTION UPON SAMPLES WITH SCATTERING AND WELL-DEFINED MULTIPATH.....	6
2.2.4. CORRECTION STATISTICS	8
2.2.5. DEPTH-DEPENDENT DISTORTION AND CORRECTION	9
3. CURRENT AND FUTURE WORK.....	11
3.1. CORRECTION OF REFRACTION.....	11
3.2. IDENTIFICATION OF TRUE TARGETS.....	12
3.3 CANCELLATION OF FALSE TARGETS.....	14
4. CONCLUSIONS	17
5. REFERENCE	17
6. PUBLICATIONS.....	20
APPENDICES	
ANNUAL REPORT OF "A STUDY OF ULTRASONIC WAVEFRONT DISTORTION COMPENSATION"	

1 INTRODUCTION

The major obstacle to achieving the high ultrasound resolution needed for early detection of breast tumors is the acoustic wavefront distortion arising from the *in vivo* breast. The distortion inside breast falls into two categories, scattering and multipath interference. Pure scattering approximates a spatially stationary stochastic process. It reduces target strength, broadens image lobe (Trahey et al., 1991, Moshfeghi and Waag, 1988) and produces a halo around a target image that degrades contrast resolution (Zhu and Steinberg 1994, Steinberg, 1995). In the last year we found that applying a time delay type compensation (TDC) descattering algorithm to *in vitro* 2-D breast data suppressed scattered energy and folded it into the target image, increasing contrast resolution (CR) by 10-20 dB (Hinkelman et al, 1995, Zhu and Steinberg, 1994). Such adaptive algorithms have been developed in many fields in the last 20 years (optics, Muller, 1974; radar, Steinberg, 1973, 1981; radio astronomy, Cornwell, 1989; ultrasound, Flax and O'Donnell, 1988, Nock *et al.*, 1989, Fink, 1992, Liu and Waag, 1994). These are global algorithms that correct time delay errors in wavefronts caused by statistically stationary random processes. This type of algorithm is well understood and can be applied to echoscanners with modest success.

The coherent interference problem, however, is unsolved. It is not a spatially stationary stochastic process. It produces image artifacts that appear as false targets. In our large aperture 2-D *in vitro* experiments to date using 1-way pulsed transmission through 1.5-4 cm breast samples, we measured the average level of refracted multipath to be -10 dB relative to the source image and the typical arrival angle to be 1-3° from the

target direction therefore in the sidelobe region of the array (Zhu and Steinberg, 1995c, preprint is Appe.). The 1-way sidelobe level may be as large as ~ 30 dB. Thus the average multipath signal level entering an imaging system is $\sim (10+30)$ or about -40 dB below the echo strength of the illuminated target. Since high resolution, high dynamic range imaging requires seeing a target 70 dB weaker than a bright target and in close proximity to it, deaberration must further suppress the multipath signal 30 dB to meet the 70 dB CR or dynamic range requirement.

False targets must first be identified in an image before they can be attacked. We have learned that the solution to this problem must be local and not global. Our approach is given in §3 (Zhu and Steinberg 1995a, 1995b). Briefly, after applying a global descattering algorithm, we then apply a spatial diversity technique to identify the false targets and a cancellation technique to reduce multipath energy. This increases CR by ~ 5 dB. This increase was achieved narrowband, i.e., processing the signals with only a single frequency component of the wideband source, and with a simple, single pole cancellor. Wideband processing and more sophisticated nulling (will be studied) are expected to further increase CR 3-5 dB. The sum of these enhancements due to descattering and derefraction is ~ 18 -28 dB, which approached the requirement with no margin for error.

Recently, we have had a leap in understanding as to how to properly treat the global problem. Our newest measurements, reported herein (§2) and submitted for publication, show an additional increase in CR improvement of ~ 10 dB (see preprint App. A of Zhu and Steinberg, 1995c). This is the first indication that we may meet the CR requirement **with** margin. We will thoroughly evaluate these results in this coming year.

2. EXPERIMENTS AND RESULTS

To develop an understanding of deaberration, our studies have concentrated on one-way propagation modelling, measurements and corrections of point source fields. §2.1 describes the 2-D *in vitro* experiments with breast samples. §2.2 reports our recent results of correction of the scattering effect upon point source images.

2.1 EXPERIMENTS

The 2-D measurement system and procedure were described in Hinkelman et al. (1995). A breast specimen was placed between hemispherical source and receiving array. The 2-D array consisted of a 92-mm 1-D linear array translated 46 mm perpendicular to its axis to form a synthetic 2-D array 92 mm x 46 mm. Element pitch in the receiving transducer was 0.72 mm and a reflecting mask reduced the receiving elevation to 1.44 mm. Frequency was 3.7 MHz. Bandwidth was 2 MHz. Waveforms were measured at each element, from which 2-D wavefronts were reconstructed as functions of time. 3-D image data were calculated by using the angular spectrum technique. The final 2-D image is obtained by detecting the peak pressure value at each position in the image plane within the transient period.

2.2 EXPERIMENTAL RESULTS

In §2.2.1 - §2.2.3 we analyze, through modelling and experiment, image distortion caused by scattering and coherent interference, and the extent to which image quality improvements are affected by deaberration. In vitro correction statistics using different correction methods are reported in §2.2.4 and depth-dependent distortion and correction in §2.2.5.

2.2.1. MODELLING OF SCATTERING

A distributed random distortion medium can be represented as a cascade of thin distortion layers (Fig.1a) or phase screens (Ishimaru, 1978). At the i th layer, the field can be written as $E_i = A_i \exp(j\phi_i)$. Phasefront distortion is developed due to time shift through each layer. Wavefront amplitude distortion evolves as the phase-aberrated wavefront propagates through the medium to successive layers (Fig.1b). Let $E_0 = A_0 \exp(j\phi_0)$ be the reference field. The distorted field is then a product of contributions from each layer

$$E(x) = E_0 E_1 E_2 \dots E_i \dots E_N \quad (1)$$

The amplitude of $\frac{E(x)}{E_0(x)}$ denoted as A_t is $A_t = A_1 A_2 \dots A_i \dots A_N$ and the phase $\phi_t = \phi_1 + \phi_2 + \dots \phi_i \dots \phi_N$. Assume that the layers are statistically independent and have common statistics; therefore $A_i = \bar{A} + \delta A_i$ and

$$A_t = (\bar{A})^N \prod_{i=1}^N \left(1 + \frac{\delta A_i}{\bar{A}}\right) = (\bar{A})^N \left(1 + \sum_{i=1}^N \frac{\delta A_i}{\bar{A}} + \text{higher order products}\right) \quad (2)$$

Since, \bar{A} is close to unity, $\frac{\delta A_i}{\bar{A}}$, $i=1,2,\dots,N$ are independent variables, the amplitude variance $\sigma_{A_t}^2 \approx N \sigma_{\frac{\delta A}{\bar{A}}}^2$, where $\sigma_{\frac{\delta A}{\bar{A}}}^2$ is the normalized amplitude variance of a single screen. $\sigma_{A_t}^2$ grows linearly with the total number of phase screens N and therefore with the propagation distance D . The phase variance $\sigma_{\phi_t}^2 = N \sigma_{\phi}^2$, where σ_{ϕ}^2 is the variance of a single phase screen; therefore $\sigma_{\phi_t}^2$ grows linearly with N and D .

The overall angular spectrum, which is the sum of coherent and scattered spectra, is broadened (Fig.2a) and reduced in strength. The background level is increased and therefore image contrast is reduced. The scattered energy increases with the propagation depth. The energy ratio (ER), which is the energy outside the main image lobe of a distorted image to the energy inside the main image lobe of the distortion-free image, is a useful tool to quantitatively evaluate the depth-dependence distortion upon image contrast. The relationship between ER and propagation depth D is (App. A)

$$ER = C(\sigma_{\phi_t}^2 + \sigma_{A_t}^2) = CN(\sigma_{\phi}^2 + \sigma_{\frac{\delta A}{\bar{A}}}^2) = C \frac{D}{d} (\sigma_{\phi}^2 + \sigma_{\frac{\delta A}{\bar{A}}}^2) \quad (3)$$

where C is a function of source illumination profile and d is the thickness of screen which is approximately the correlation distance of the medium. ER grows linearly with distance.

As long as certain correlation properties exist in the wavefront, phase compensation algorithms are still useful in strong scattering to partially remove phase distortion and build up the strength of the coherent field (Fig.2b). Wavefront amplitude distortion remains, as does residual phase distortion, and produces a significantly high incoherent background level in the spectrum. Any phase-deaberration procedures that provide a better phase error estimate than that of basic algorithms (Fax and O'Donnell, 1988, Attia and Steinberg, 1989, Nock *et al.*, 1989) can reduce this background level. Wavefront-deaberration

algorithms that take amplitude distortion into account and reduce wavefront amplitude variance can further reduce this background level.

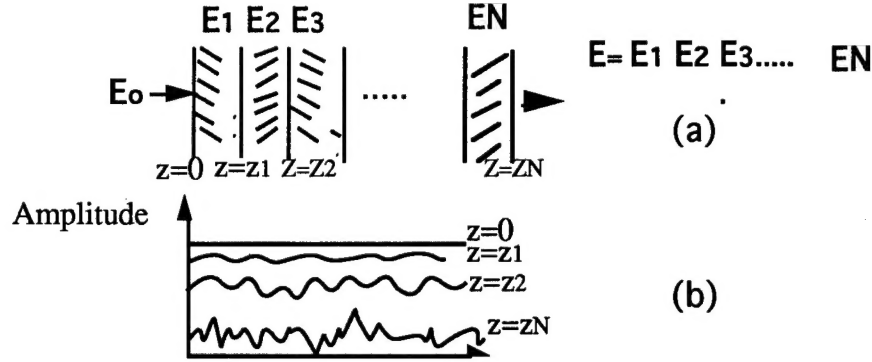


Fig.1 The field is the product of contributions from each layer. Wavefront amplitude fluctuation increases as wave propagates.

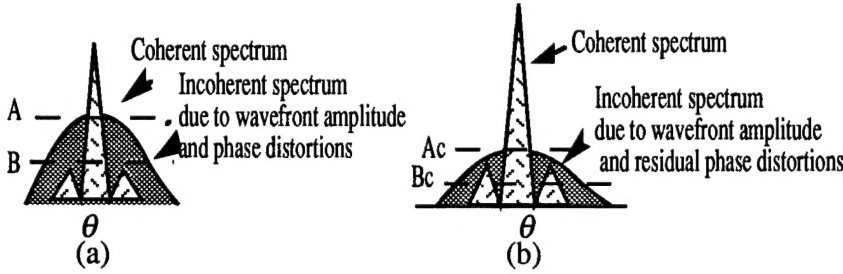


Fig.2. Statistical models of angular source intensity distribution. (a) Before phase correction. (b) After phase correction.

The optimum weight vector W compensates exactly for amplitude and phase distortion. Assume a complex signal vector S is received instead of S_0 which would have been received had the medium been homogeneous. The distortion vector is $S_0/S = A \exp(j\phi)$. Then, $W_{\text{opt}} = A^{-1} \exp(-j\phi)$ making the corrected signal vector $S_0' = S_0 A^{-1} \exp(-j\phi) = S$. This is theoretically ideal for fidelity but has drawbacks. Phase is corrected exactly and in a stable manner. However, because W_{opt} adjusts the channel gain to be the reciprocal of the signal strength, at points in the receiving aperture where signal strength is weak, the enhanced channel gain raises the noise to the point where SNR can be impaired. This is particularly troublesome when there is coherent refractive interference in the receiving array. A compromise weight vector is one that nearly but not quite reciprocates the received amplitude. We demonstrate below the improvement obtained with $S_0' = A^{1/2} S$ and $S_0' = A^{1/4} S$. We call the first operation 'square rooter' or 'rooter' and the second 'fourth rooter'.

Square rooter changes eq. (2) to

$$A_i^{1/2} = (\bar{A})^{N/2} \prod_{i=1}^N \left(1 + \frac{\delta A_i}{\bar{A}}\right)^{1/2} = (\bar{A})^{N/2} \left(1 + \sum_{i=1}^N \frac{\delta A_i}{2\bar{A}} + \text{higher order products}\right) \quad (4)$$

The amplitude variance $\sigma_{A_i}^2 \approx \frac{N\sigma_{\delta A}^2}{4}$ which is 4 times less than that with unit amplitude

weight. Assuming phase error $\sigma_{\phi_i}^2$ is compensated, ER reduces from $C \frac{D}{d} \sigma_{\delta A}^2$ to

$C \frac{D}{4d} \sigma_{\delta A}^2$ which gives about a 6 dB increase in image contrast if the energy is uniformly

distributed. Mth rooter will reduce the amplitude variance by 2M. This nonlinear transformation upon wavefront amplitude is a compression operation, and it is an intermediate step between matched filtering ($M=1/2$) and inverse filtering ($M \rightarrow \infty$) (Fig.3). Inverse filtering at the aperture corresponds to a deconvolution operation in the image plane, and it is optimal but noisy when the SNR is low. However, as shown in Appendix A, low order rooters (2nd and 4th order), in addition to phase deaberration at the aperture or in addition to backpropagation and phase deaberration at an optimal backpropagation distance (Liu and Waag, 1994), can significantly improve ER without encountering the noise problem. The detailed evaluation of the effects of this nonlinear compression upon the image will be performed by studying the amplitude distributions of images before and after the operation. This is a subject of future study.

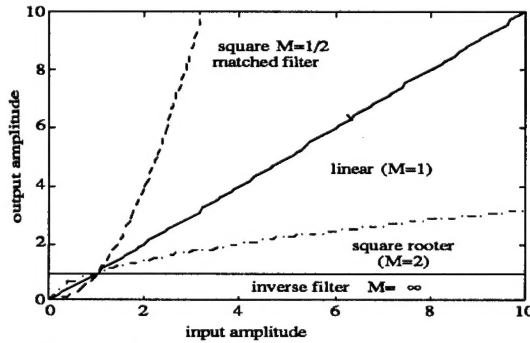


Fig.3. Plots of the input and output amplitude transforms.

2.2.2. MODELLING OF SCATTERING AND REFRACTION

In a refractive medium coherent rays can be bent and split after they pass through tissue beds with different sound speeds (Zhu and Steinberg, 1992). The interference of refracted coherent ray bundles with incident rays produces image artifacts which appear as false targets (Fig.4)

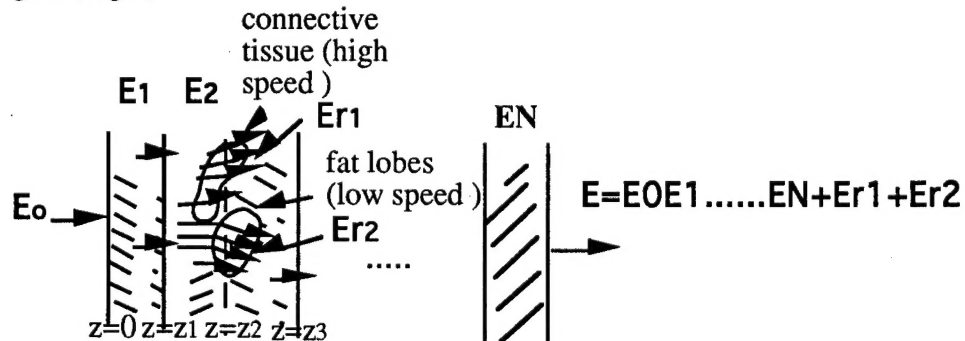


Fig.4. The field is the original field plus refracted fields.

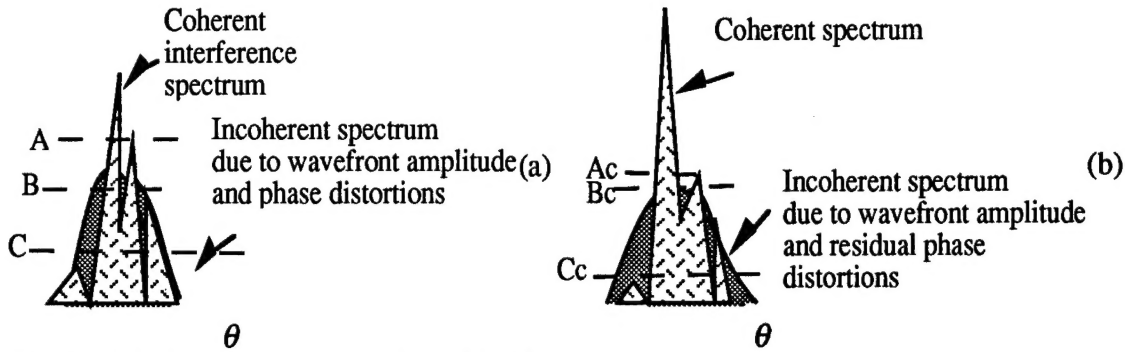


Fig. 5. (a) Before phase compensation. (b) After.

The angular source intensity distribution is the superposition of the intensity image lobe, coherent interference lobes and scattering spectrum (Fig.5a). The strengths and the numbers of interference lobes depend on orientations, curvatures, sizes and numbers of refractive bodies in the insonified medium, and may not be directly related to propagation depth. Although the chance of incident rays passing through more refractive bodies increases with propagation depth, the strengths of interference lobes resulting from multiple refraction may not be significant compared with those from single refraction.

The correction mechanism in a strong scattering and refraction medium is as follows: If the primary field is stronger than secondary refraction fields, the scattered energy removed by deaberration process strengthens the primary field by folding the removed scattered energy into the primary field. As a result the ratio of image lobe to interference lobe is improved (Fig.5b). If, however, the primary field is weaker than the refracted field, the scattered energy removed by deaberration process may strengthen the refracted field. The corrected result could then be worse than without correction. However, we have seen no evidence of this so far in our experiments reported in App.A.

2.2.3. CORRECTION UPON SAMPLES WITH SCATTERING AND WELL-DEFINED MULTIPATH

In most breast samples, scattering and coherent interference are both present. Fig.6 are -10 dB contour plots of images obtained from water path and 4-cm breast tissue path (brs006). Contour spacing is 2 dB. In tissue image (b), three lobes instead of one central image lobe appear. Inner contours of the image lobe are close to the system diffraction pattern (Fig.6a) while the outer contours are highly irregular due to scattering. Point resolution is worsened in azimuth/elevation by approximately 2:1 and 3:1. Two refractive lobes with strengths -6 and -8 dB appear at (-4, -2.5) and (3.5, 1.5).

A symmetric scattering pattern generally appears when the threshold is reduced, as shown Fig.6c with a -16 dB threshold contour and contour spacings of approximately 1.5 dB. The outer contours show a roughly symmetric pattern typical of scattering while the inner contours show an asymmetric lobular interference pattern.

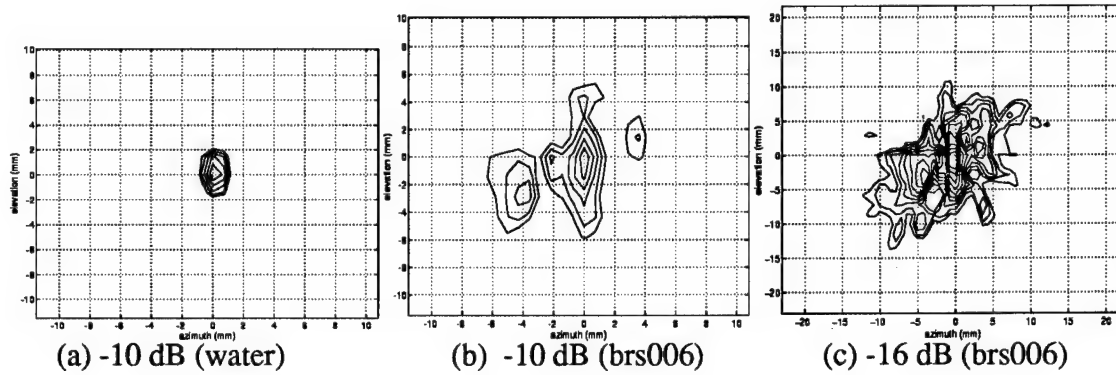


Fig.6. 2-D contour maps of point source images. (a) water data showing diffraction pattern of system. Outer contour is -10 dB level. (b) measured through the 4-cm tissue (brs006), showing highly asymmetric interference pattern. Outer contour is -10 dB level. (c) Image brs006 at -16 dB contour level. The outer contour shows more symmetrical scattering pattern. Note the change of scale from (a) and (b).

Fig.7 shows correction results of the sample image brs006 after applying different methods. The contour spacings are the outer contour levels divided by 10. Part a is the -16 dB contour map of applying TDC (see Fig.6c for comparison)). Image quality improved significantly because of the minimization of the phasefront distortion caused by scattering. The area within the -16 dB inner contour is reduced by a factor of 11. The mainlobe pattern is close to the system diffraction pattern although the area is still 1.6 times larger than the area in water at the same level. Two large lobes remain as expected and appear as two additional sources. Fig.7h is the correction result at a -16 dB level of applying wideband DSA. It is evident that the procedure enhances interference in this example; the artifacts are 5 dB higher than in Fig.7a. Parts b and c show -25 and -30 dB contour plots of TDC. In Fig.7b the outer contours show an asymmetric interference pattern with scattered energy distributed around the two interference lobes. In Fig.7c the outer contours show the more symmetric scattering pattern caused by incoherent wavefront amplitude distortion and residual phase distortion. Fig.7d is the result of phase conjugation at -30 dB. The approximately symmetric scattering pattern outlined by outer contours in (c) is improved due to better phase deaberration. The energy is more concentrated around the image lobe and interference lobes. Part e is the result of backpropagation and phase conjugation at the optimum backpropagation distance. The scattering pattern is further improved as compared with the result of phase conjugation at the aperture. The backpropagation distance of this sample is 50 mm. Part f is the result of phase conjugation and square rooter at -30 dB. The pattern is very close to the system diffraction pattern. Phase conjugation and 4th order rooter shown in part g restores the diffraction-limited image to a -30 dB level.

It is interesting to note that the strengths of the two interference lobes are also reduced by 8 dB after TDC and phase conjugation. They are further reduced by 5, 7 and 15 dB after backpropagation and phase conjugation, phase conjugation and square rooter and phase conjugation and 4th order rooter, respectively. The improvement comes from the scattered energy which is originally distributed around the mainlobe and each of the refracted multipath lobes. This energy is coherently added back, by the deaberration process, to the dominant lobe, which in this case is the mainlobe. The overall result is an improvement of the image lobe to the interference lobe ratio. In nine samples that have well defined refraction, we have found an average of a 10 dB (std. 4dB) improvement in the range of 5-16 dB after TDC, due to the coherent strengthening of the mainlobe.

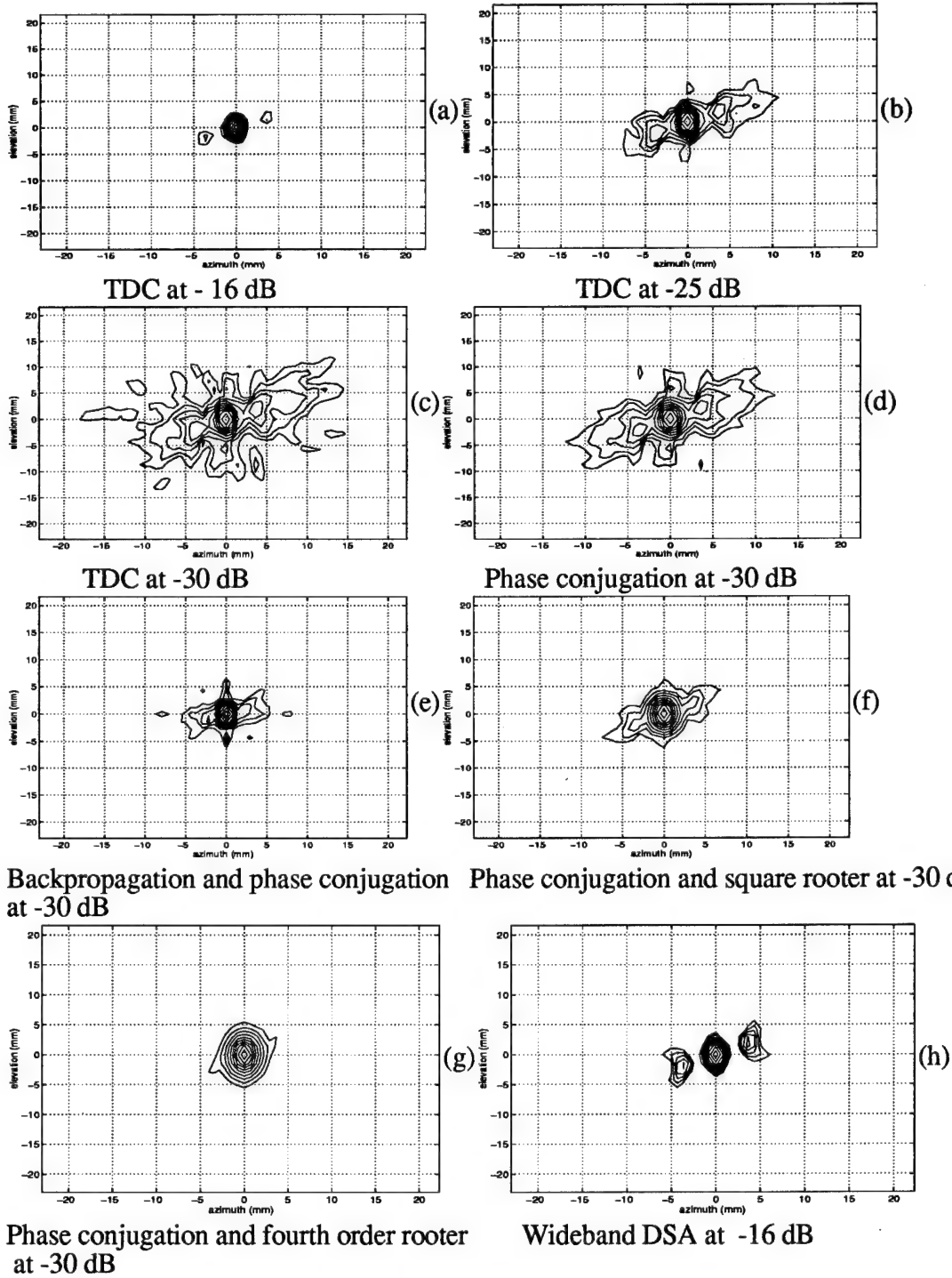


Fig. 7. Distortion corrected contour maps of the sample image brs006 (a) TDC at -16 dB level. (b) at -25 dB level and (c) at -30 dB level. (d) PC at -30 dB level. (e) Back-propagation and PC at -30 dB. (f) PC and square root amplitude correction at -30 dB. (g) PC and fourth order rooter at -30 dB. (h) Wideband DSA at -16 dB. Artifacts are 5 dB higher than time-delayed correction shown in (a).

2.2.4. CORRECTION STATISTICS

A simple metric, the lowest level of mainlobe diffraction shape, is used here to quantitatively evaluate improvement upon image quality by using different correction

algorithms. The mainlobe diffraction shape is identified when the elevation-image width to the horizontal width is approximately a 2 to 1 ratio and the outermost image contour has an elliptical shape. This metric is closely related to contrast resolution (level A in Figs.2 and 5). The net improvement due to correction is A-Ac.

The average levels (std. dev) of the restored mainlobe diffraction shape before and after corrections of three groups are given in Table I. The mainlobe shape is restored up to -19.3 (2.3) and -19.4 dB(2.7 dB) by using two phase-deaberration algorithms, TDC and phase conjugation, respectively. The fact that the correction result of TDC is very close to that of phase conjugation suggests that the limit of phase correction with respect to the selected metric has been achieved by TDC. Further improvement requires correction algorithms that can take wavefront amplitude distortion into account. Wideband DSA is able to restore the mainlobe shape to -14.8 dB(2.2 dB). This result is about 5 dB worse than that of using two phase-deaberration algorithms. The reason is the improper wavefront amplitude weighting because the amplitude variance is increased. Phase conjugation and square rooter on wavefront amplitude further restores the mainlobe diffraction shape to -25.3 dB (2.4 dB). Phase conjugation and 4th order rooter achieves a -31.2 dB (1.8 dB) level, which is about a 12 dB improvement more than that of using two phase deaberration algorithms. This level is very desirable for a high quality ultrasound echo scanner. Backpropagation and phase conjugation at an optimal backpropagation distance improves the performance of phase conjugation at aperture by 5 dB. Square rooter further improves the procedure by another 5 dB. The correction result of backpropagation and phase conjugation is similar to phase conjugation and square rooter.

The restored mainlobe diffraction levels among different groups are similar when different correction methods are used. But the improvements shown in Table I are, in general, 6 dB larger in the scatter group than that of the other two groups because the mainlobe shape is distorted at zero dB in the former group.

Table I Statistics of restored mainlobe diffraction shape level

Diffraction pattern (dB)		Diffraction pattern after correction (dB)					
w/o correction	TDC	Phase conj.	Wideband DSA	Phase conj. & square rooter	Phase conj. & 4th order rooter	BP & phase conj.	BP & phase conj. & square rooter
A -0(0)	-18.8 (1.9)	-19.0 (2.2)	-14.8 (2.6)	-25.3(3.0)	-32.3(2.8)	-24.3(2.06)	-29.5 (2.7)
B -5.8(1.3)	-19.7 (2.3)	-19.7 (3.5)	-14.7 (1.5)	-25.3(2.1)	-30.7(1.2)	-23.7(0.58)	-29.3(2.31)
C -6.1(3.5)	-19.3 (2.7)	-19.6 (2.5)	-14.8 (2.5)	-25.4(2.5)	-30.7(1.4)	-23.9(2.37)	-29.3(2.96)

A. Primarily scatter

B. More scatter than refraction

C. Scatter plus well-defined refraction

BP: backpropagation

2.2.5. DEPTH-DEPENDENT DISTORTION AND CORRECTION

The scattered energy increases with the propagation depth D in the breast; therefore the performance of descattering algorithms is expected to deteriorate with D. Finding useful algorithms that can provide good focusing throughout the average propagation depth in the breast, which is approximately 100 mm, is extremely valuable for the next generation high quality breast scanners.

A quantitative measure of scattered energy at the image plane is the energy ratio ER introduced in eq. (3), which is the energy outside the main image lobe of a distorted image to the energy inside the main image lobe of the distortion-free image. ER is directly related to image contrast. Fig.8a upper curve is the linear regression plot of ER vs. D. The correlation coefficient is 0.67 and the linear relationship is significant as predicted by equation (1). ER in water image is 0.088, which is included in the data points to represent system performance at zero depth. The rest of the regression curves in Fig.8a show ER vs. propagation depth obtained by using five different correction methods. ER in water image after phase conjugation is 0.004 which is included in all data sets to represent the calibrated ER at zero depth. The correlation coefficients of regression curves are indicated in the figure by R. The average values of ER (std. dev.) are given in Table II. The linear relationships are statistically significant for all curves.

Table II Statistics of ER before and after corrections

w/o Corr.	TDC	phase conj.	Wideband DSA	BP & phase conj.	Phase conj & square rooter	BP & phase conj. & square rooter	Phase conj. & 4th order rooter
0.58(0.11)	0.23(0.05)	0.18(0.04)	0.28(0.08)	0.11(0.02)	0.09(0.03)	0.04(0.01)	0.03(0.01)

BP: Backpropagation.

The performance of wideband DSA is the worst among all correction procedures. Regression curves of wideband DSA and phase conjugation are approximately parallel to each other but phase conjugation reduces ER by an average of 10%. The average ratio of ER after DSA over ER after phase conjugation is 1.6 which is about 2.4 times less than that predicted by eq.(5). However, the theory is derived for narrowband and can only be used as an approximation for wideband. At 100 mm depth, ER after phase conjugation reaches 0.57, which is about the average of ER without correction (see first column of Table II). Therefore, the best linear phase correction procedure at the aperture is unlikely to be useful at this depth. The average ER after TDC is 5% more than that of phase conjugation while the averages of the lowest level at which mainlobe diffraction shape is maintained are the same when TDC and phase conjugation are used. This implies that the residual phase error due to imperfect phase correction contributes primarily to energy in the sidelobe region. Backpropagation and phase conjugation reduces the average ER by 7% below that of phase conjugation at the aperture and is the best among the linear operations. The performance of phase conjugation and square rooter at the aperture is slightly better than that of backpropagation and phase conjugation. At 100 mm, both curves reach 0.30 which is about the average level of wideband DSA (see second and third columns of Table II) obtained from the average 2.7 cm propagation depth. This energy ratio is only useful for good image contrast beyond -15 dB (see Table I).

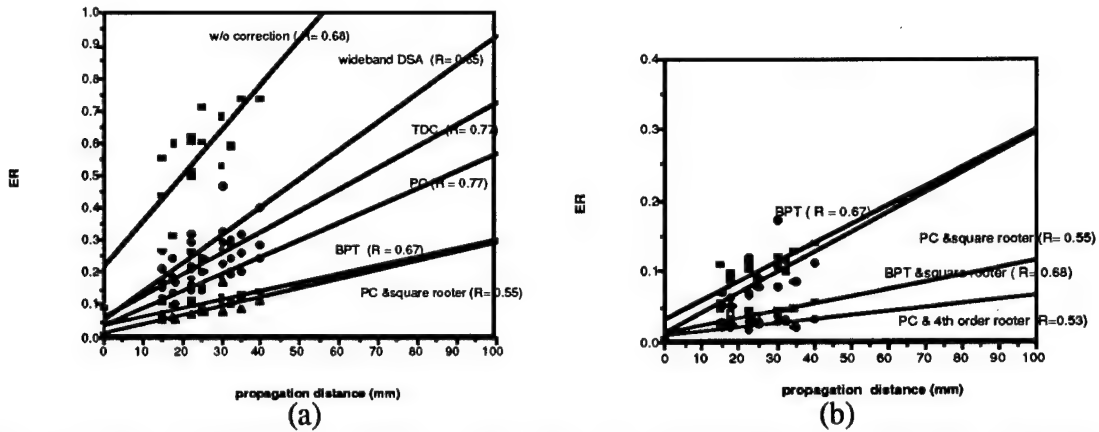


Fig.8. (a) Linear regression curves of ER vs. propagation depth obtained from five correction procedures. (b) Results of ER vs. propagation depth obtained from four correction procedures. PC: Phase conjugation. BPT: Backpropagation and phase conjugation.

Fig. 8b shows the results of ER by using backpropagation and phase conjugation and square rooter and phase conjugation and 4th order rooter at the aperture. Regression curves obtained from phase conjugation and square rooter and backpropagation and phase conjugation are also included in (b) for comparison. At 100 mm depth, the regression curves of backpropagation and phase conjugation and square rooter and phase conjugation and 4th order rooter reach 0.12 and 0.07, respectively. These ERs are about the average levels of backpropagation and phase conjugation and phase conjugation and square rooter obtained from the average 2.7 cm propagation depth (see Table II). The result indicates that focusing with very high image contrast beyond -25 dB (Table I) throughout the 100 mm propagation depth is achievable by taking the low order root on wavefront amplitude plus (1) phase deaberration at the aperture or (2) backpropagation and phase deaberration at an optimal backpropagation distance.

3. CURRENT AND FUTURE WORK

To further increase CR, false targets produced by coherent multipath have to be cancelled. Multipath interference, however, is a much more difficult problem than scattering. Because it is not a stationary, stochastic process, two distinct steps are required to deaberrate refraction-contaminated data. It is first necessary to recognize which energy is simple scattering and which is not. The second is to remove nonisotropic, coherent interference energy. §3.1 discusses the significance of multipath interference. §3.2 provides in vitro evidence that subarray diversity images are useful for identification and §3.3 introduces our approaches to removing multipath energy.

3.1. CORRECTION OF REFRACTION

A coherent interference phenomenon was demonstrated in the 1-way transmission model and experiments. The descattering algorithms can reduce the interference level down to -30 dB region on reception. The impact of interference upon 2-way echo scanning is significant as illustrated in Fig.9. A transmitting beam illuminates a tumor or target T (part a). Because of refraction, a subbeam is split from the original beam and insonifies targets along θ_1 . On reception, if no echo signal is coming back from the targets illuminated by the subbeam (simplest case), the receiving beam upon T (part b) may split in the same fashion as the transmitting beam (reciprocity) and a dual image may result. This simplest case corresponds exactly to the situation in the 1-way transmission model described in Figs.1 and 4 and experiments reported in Appendix A, where an active point source instead

of a passive point target is used. In reality, refracted energy from the targets insonified by the subbeam will arrive at angles of $1 - 3^\circ$ from the target direction and therefore in the sidelobe region of array. The sidelobe level of receiving beam will be ~ 30 dB. The average level of refracted multipath is to be -10 dB relative to the target image and therefore the average multipath signal level entering the system is $\sim (10+30)$ dB below the echo strength of the illuminated target. The cancellation algorithms must suppress multipath signals to achieve a ~ 70 dB contrast resolution, which is essential for preventing contamination of otherwise black cysts with scattered and/or refracted echo energy and thereby causing them to look like speckled tumors.

3.2. IDENTIFICATION OF TRUE TARGETS

We have found that geometric techniques may be able to separate nonisotropic from isotropic scattered energy. Fig.10 illustrates the case where a single source and 1-D reception are used for descriptive convenience. The same principle is applicable to a multiple source distribution and 2-D configuration. A source radiates into a scattering and refractive medium and its radiation field is received by a receiving aperture. The source image obtained from any aperture is the superposition of the image lobe, image artifacts caused by coherent interference and an incoherent scatter spectrum. The location and shape of the image lobe generally remains the same when viewed from different apertures, such as the left and right halves of the aperture, while the locations, sizes and shapes of the image artifacts are likely to change because the fields intercepted by different subapertures encounter refractive bodies with different orientations, curvatures and sizes. The incoherent spectrum is statistically the same in each subaperture image. Therefore, the locations and shapes of the large lobes in different subaperture images can be used to distinguish the image lobe from image artifacts. Fig. 11 shows such an example. Part a is the -10 dB contour plot of the 2-D image obtained from the entire aperture (92 mm by 46 mm) while (b)-(e) are obtained from four subapertures. The breast sample is 3-cm.. The real target remains in the same locations. Its shape is unchanged. False targets move and change size and shapes when viewed from different subapertures. For example, there are two lobes appearing in (a) (centered at $(-2.5, 0.6)$, $(5.4, 0.6)$), which do not appear in part b. Therefore they are false targets and should be removed. Fig.12 shows an example of two targets which are separated by 12 mm and viewed from the entire aperture and four subapertures. Again, real targets remain in the same locations and false targets move and change appearances. In this example, one false target located at $(0, -5)$ appears in both left and right aperture images and can not be resolved by upper and low aperture images. The remaining four artifacts can be identified as false targets.

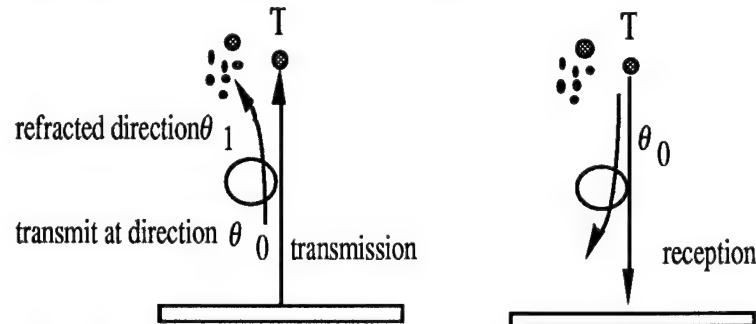


Fig.9. Illustration of effect of refraction upon pulse echo imaging (simplest case with no interference echo signal coming back from targets insonified by subbeam).

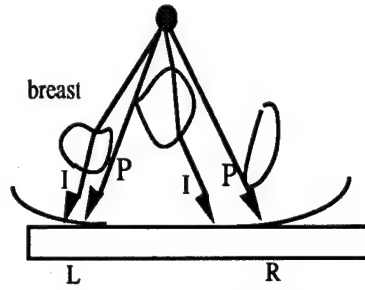


Fig.10 Illustration of diversity. P refers primary field and I interference field. The interference fields change with propagation path.

From our *in vitro* samples (9 out of 16) that have well-defined multipath, we found that 2-D subarray diversity images in general are useful for identification while 1-D subarray images fail to provide identification most of the time because of incomplete distortion information. From our three pairs of measurements with two sources located 12 mm apart, we also found 2-D subarray diversity images are useful for identification. However, when two sources are located close to each other, the constructive and destructive interference of real targets with the multipath targets may create difficulty in identification. More *in vitro* measurements with multiple source configuration (sources are located close to each other) and diverse tissue types will be made to thoroughly test the effectiveness of subaperture diversity for identification of false targets.

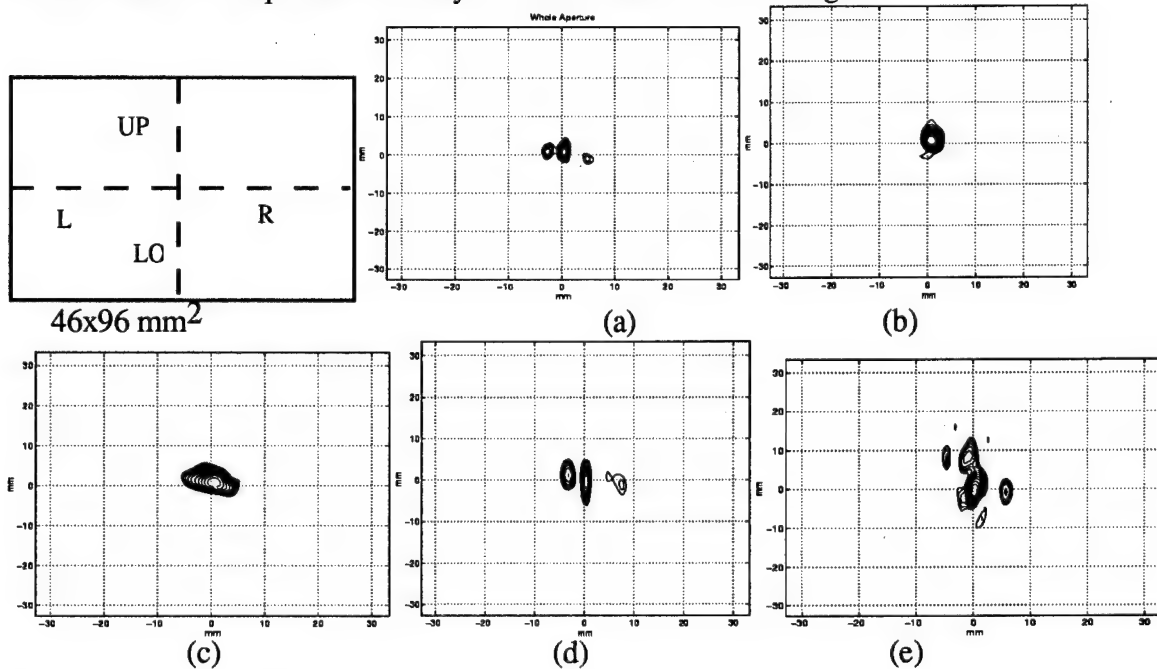


Fig.11 Quadruple spatial diversity discloses false targets. Images are obtained at central frequency. Real target remains in place in subarray images while multipath target changes location, size and shape. Outer contour is at -10 dB level. Image (a) Image of entire aperture (46x92 mm). (b) Image from left half of array. 46x46 mm. (c) From right half. (d) From upper half (23x92mm). (e) From low half. Point source remains in center in all images. Shape change is due to the change of aperture size. Being geometrically stable, it is identified as real target. Two questionable secondary sources appear in (a) (centered at (-2.5, 0.6) and (5.4, 0.6)), but not in (b). Therefore they are image artifacts, false targets, which will be removed by adaptive interference cancellation [From Zhu and Steinberg 1995b].

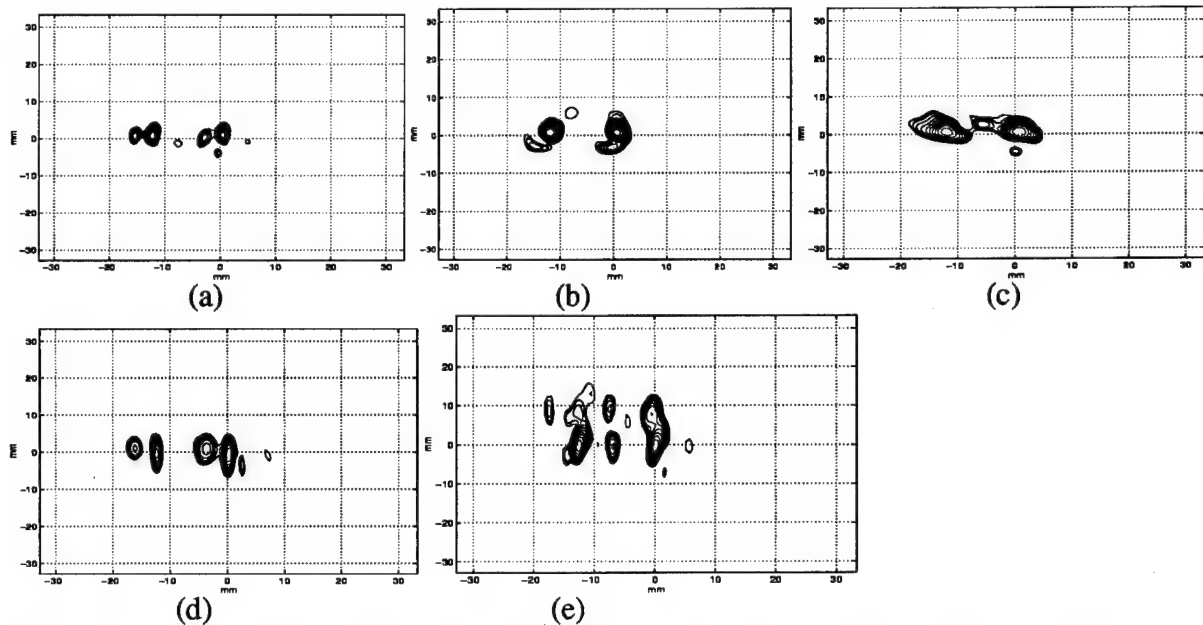


Fig.12. Quadruple spatial diversity discloses false targets. Images are obtained at central frequency. Two real targets remain in place in subarray images while multipath target changes location, size and shape. Outer contour is at -10 dB level. (a) Image of entire aperture. (b) Left half. (c) Right half. (d) Upper half. (e) Low half. Being geometrically stable, it is identified as real target. Four questionable secondary sources appear in (a), centered at $(-16.2, 0.6)$, $(-7.62, 1.14)$, $(-2.5, 0.6)$ and $(5.4, 0.6)$, can be identified as false targets and be cancelled. The false target at $(0, -5)$ appears in both left and right aperture images and can not be resolved by upper and low aperture images. [From Zhu and Steinberg 1995b]

3.3 CANCELLATION OF FALSE TARGETS

Once the true targets are distinguished from the false ones, CLEAN or some other cancellation procedure has to be performed to reconstruct the original refractive-artifact-free scene or to cancel the false targets.

COHERENT CLEAN

CLEAN is a nonlinear deconvolution procedure originated in radio astronomy in the 1960s (Hobbom, 1974), extended to radar by Tsao and Steinberg (1988) and applied to ultrasound by Cohen (1992). The diffraction pattern $f(u)$ is shown upper left in Fig.13. The procedure begins with the original dirty image $A_0(u)$ (Fig.13a). The strongest source is found and its complex amplitude a_0 and coordinates u_0 are measured. An image of that source is found by convolving the radiation pattern with a δ -function of strength a_0 located at u_0 (Fig.13a). Some fraction of this image is subtracted from $A_0(u)$. The result of this first iteration is a new image, $A_1(u)$, from which all energy from the strongest source has been removed, including its sidelobe energy (Fig.13b). The process continues until the subtraction procedure produces images with negative values. The result at this stage is a list of detected sources. The next step is to calculate a CLEAN beam that has the resolving power of $f(u)$ but without its sidelobe distortion. The final image is the convolution of the CLEAN beam and each of the detected sources (Fig.13c).

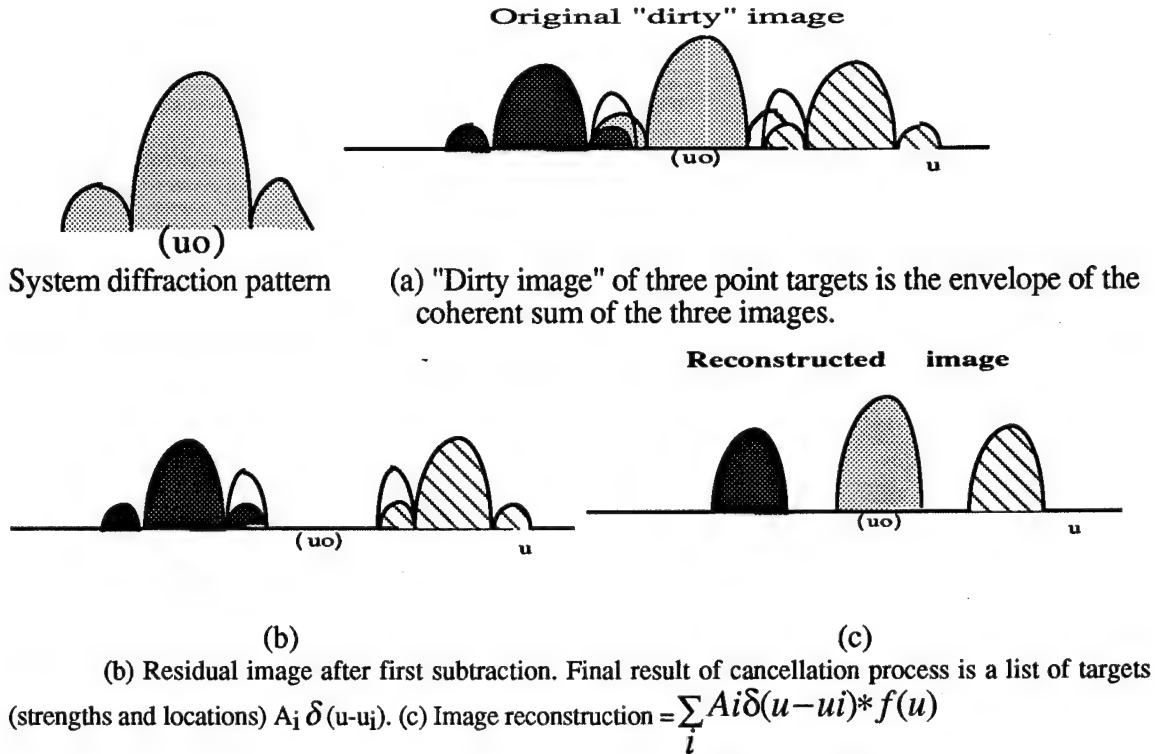


Fig. 13. Illustration of the clean procedure. (a) Dirty image (left) and system diffraction pattern (right). (b) After the first iteration of the clean procedure. The strongest target is subtracted out as well as its sidelobes. (c) Final reconstructed image.

However, the above CLEAN procedure cannot be directly applied to an image that is contaminated by image artifacts, because CLEAN will pick up true targets as well as false targets. A clever use of CLEAN is to apply it to false targets only after first identifying true targets, which are found by the diversity technique described above. Also, CLEAN is modified to change the diffraction pattern to produce better subtraction result.

We have also found that multiplication of diversity images can significantly simplify target identification. Fig.14 is the contour plot at -40 dB level of the multiplication image of the five diversity images shown in Fig.12. The artifacts are suppressed because they appear at different locations in each diversity image while the targets are enhanced because they appear at the same locations. Fig.15(a) is the CLEANed image of Fig.12(a). The residual image which contains all the refractive artifacts is shown in part (b). The improvement is significant.

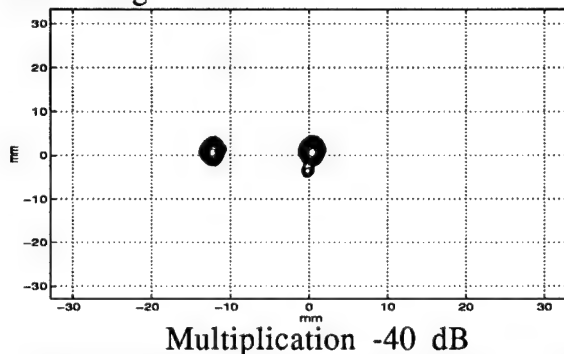
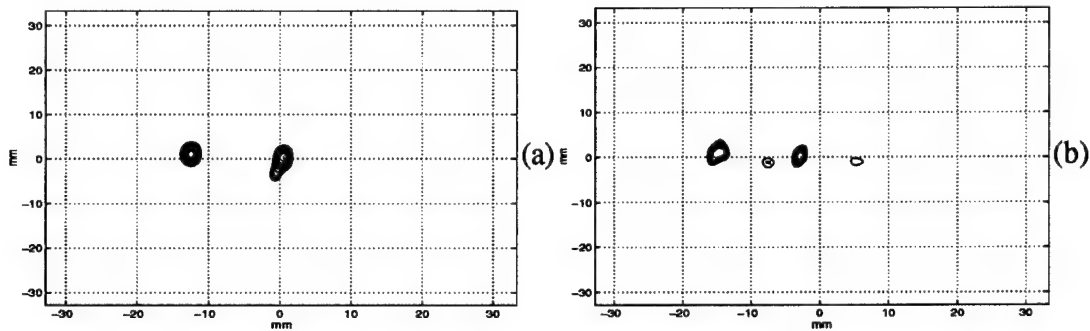


Fig. 14. Multiplication of five images of Fig.12. Two true sources with equal strength are located at (0,0) and (-12, 0) (From Zhu and Steinberg 1995b).



Cleaned image of Fig.12(a)
Fig.15. -10 dB contour plots of cleaned image (a) and residual image after clean (b).

COHERENT CANCELLATION

The CLEAN procedure produces relatively artifact free images as shown in Fig.15a. The limitation so far is the threshold imposed on the multiplication image which restricts the target dynamic range. Coherent cancellation of false targets can avoid the problem. Our first 1-D, narrowband cancellation experiments have been conducted. Preliminary experiments on *in vitro* breast samples show considerable improvement in terms of contrast resolution. Fig.16 is an example. The scattered energy is first corrected by phase conjugation. Part (a) shows the original phase deaberrated image with two large refractive lobe pairs (-10 and -16 dB strengths) identified by location diversity. Part b shows the cancellation result on the inner artifact lobe-pair alone. This target has been reduced to -40 dB, a reduction of 30 dB. The remainder of the pattern is hardly disturbed, which implies that a repetition of the procedure on the -16 dB target pair would do about the same. Successive iterations should reduce the background to about the residual scatter level, which is estimated at -24 dB. Thus at least 14 dB contrast resolution improvement would be obtained.

2-D cancellation is more difficult than 1-D because incomplete cancellation can produce a crater around the false target. The simple procedure used for Fig.17 matched only position, amplitude and a single curvature parameter of the cancellation beam. Effectively it is a single zero solution to a problem of higher dimensionality. However, we are now studying more sophisticated cancellation procedures and anticipate significant superior results.

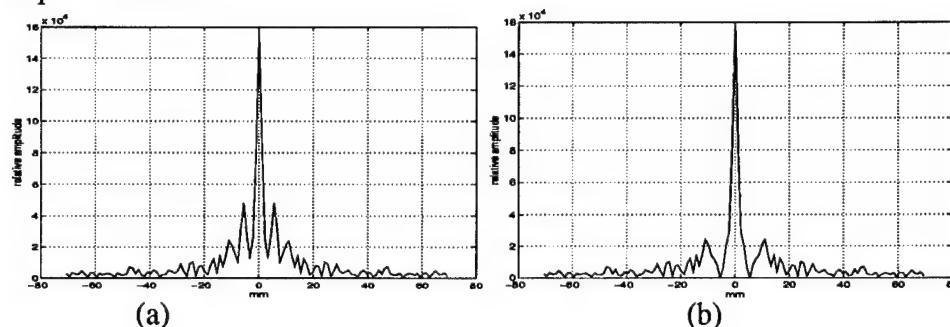


Fig.16. An example of coherent cancellation. (a) Original image after phase conjugation for correction of scattered energy. (b) After coherent cancellation of inner false-target pair. The improvement is about 30 dB in artifact strength.

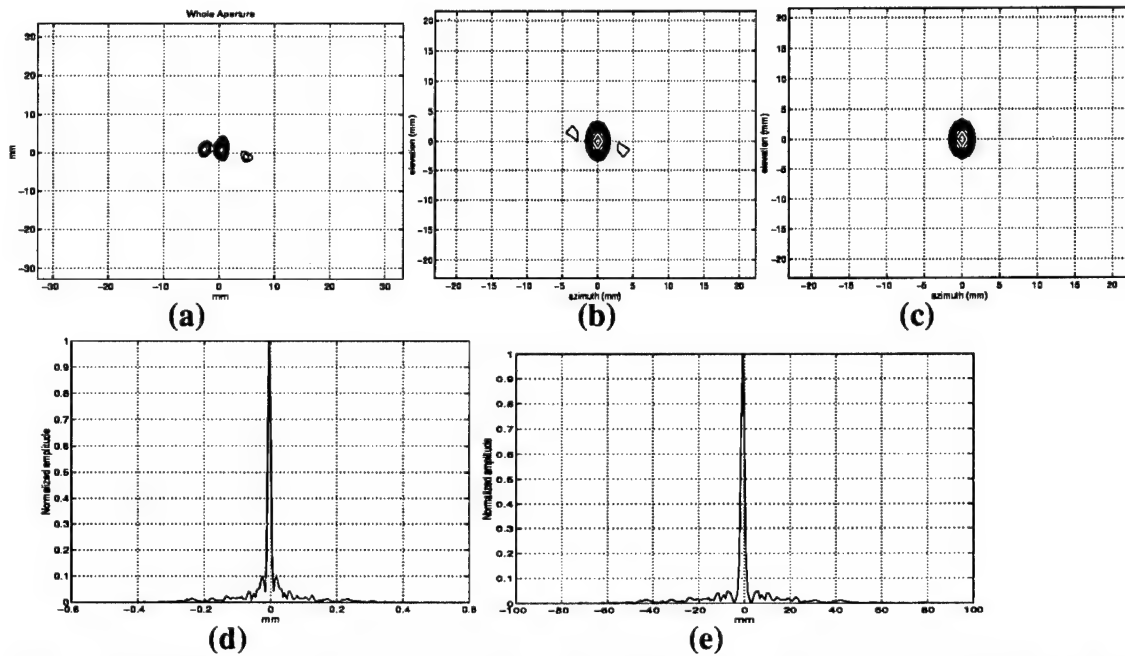


Fig.17. (a-c) Contour plots of 2-D image (brs001) at central frequency. (a) -10 dB contour of original image (brs001) shown in Fig.11 (a). (b) Descattering result of part (a) at -22 dB. The contrast improvement is 12 dB. (c) -22 dB contour of descattering and cancellation result. Refractive lobes are cancelled but the crater appears at -27 dB. The overall 2-D contrast improvement is 5 dB. (d) and (e) show 1-D cuts of brs001 image before and after descattering and cancellation. (d) a 1-D cut of Fig.17 (b) at -16° . (e) 1-D cut of Fig.17(c) at -16° . The refracted energy is reduced significantly. The contrast improvement in this cut due to cancellation is 7 dB.

4. CONCLUSIONS

The long-term objective of this research is the ultrasonic echo-scanning demonstration of the detection and diagnosis of small breast tumors of a few mm (~ 2 mm) in size. The tools that have been investigated are signal processing techniques for compensation of the ultrasonic wavefront distortion produced by scattering and multipath interference arising from the female breast.

Recent 2-D wavefront compensation studies show that amplitude compression in addition to phase deaberration (Zhu and Steinberg, 1995, preprint App.A), is akin to inverse filter, improves contrast resolution to 10 dB more than that of existing time-delay type phase deaberration algorithms (Flax and O'Donnell, 1988, Nock et al., 1989), and 5 dB more than that of backpropagation and phase deaberration (Liu and Waag, 1994). Preliminary studies also show that diverse images obtained from different spatial locations of a large 2-D aperture are likely to provide the identification information (Zhu and Steinberg, 1995b) of true targets vs. image artifacts. Once the real targets are identified, nonlinear deconvolution techniques and interference cancellation techniques are applicable to reconstruct the original refractive artifact-free scene or to cancel image artifacts. The initial results are encouraging. Currently, we are evaluating these techniques.

5. REFERENCE

Atia, E.H. and Steinberg, B.D. (1989), "Self-Cohering Large Antenna Arrays Using the Spatial Correlation Properties of Radar Clutter," IEEE Trans. Antennas Prop., AP-37(1), 30-38.

Cohen, N., "Practical real-time deconvolution and image enhancement of medical ultrasound," Biological Image Processing and 3D Microscopy, ed. by R. Acharya, C. Cogswell and D. Goldgof, SPIE, Bellingham WA 1992.

Cornwell, T. J., "The Application of Closure Phase to Astronomical Imaging," *Science* **245**, 4915 (1989).

Fink, M., "Time reversal of ultrasonic fields – part I: basic principles," *IEEE Trans. Ultrason. Ferroelec. Freq. Contr.*, vol. 39, pp. 555-566, 1992.

Flax, S. W. and O'Donnell, M. "Phase Aberration Correction using Signals from Point Reflectors and Diffuse Scatterers: Measurements," *IEEE Trans. Ultrason. Ferroelec. Freq. Cont.*, **35**(6):768-774, Nov. 1988.

Freiburger, P.D., Sullivan, D.C., LeBlanc, B. H., Smith, S. W., and Trahey, G.E., "Two Dimensional Ultrasonic Beam Distortion in the Breast: In vivo measurements and effects," *Ultrason. Imag.* **14**(4), 398-414 (1992).

Hinkleman, L.M., Liu, D-L., Waag, R.C., Q. Zhu and B.D.Steinberg, "Measurement and correction of ultrasonic pulse distortion produced by the human breast," *JASA* (97) No.3, 1958-1969 (1995).

Hobbom, J. A., "Aperture Synthesis with Non-Regular Distribution of Interferometer Baselines," *Astron. Astrophys. Suppl.*, Vol. 15, pp. 417-426, 1974.

Ishimaru, A. (1978), *Wave Propagation and Scattering in Random Media*, Academic Press, New York.

Liu D-L and Waag, R.C., "Correction of Ultrasonic Wavefront Distortion Using Backpropagation and Reference Waveform Method for Time-shift Compensation," *J. Acoust. Soc. Am.* **96**, 649-660 (1994).

Muller R.A., and Buffington, A., "Real-Time Correction of Atmospherically Degraded Telescope Images through Image Sharpening," *J.Opt. Soc. Am.*, **64**(9) 1200-1210 (September 1974).

Moshfeghi, M. and Waag, R.C., In Vivo and in Vitro Ultrasound Beam Distortion Measurements of a Large Aperture and a Conventional Aperture Focused Transducer, *Ultrasound Med. Biol.* **5**, 415-428 (1988).

Nock, L., Trahey, G. E., and Smith, S.W., "Phase Aberration Correction in Medical Ultrasound Using Speckle Brightness as a Quality Factor," J. Acoust. Soc. Am., **85**(5) 1819-1833 (1989).

Steinberg, B.D., "Design approach for a high resolution microwave imaging radio camera," J. Franklin Inst. (Dec. 1973).

Steinberg, B.D. and H. Subbaram, *Microwave Imaging Techniques*, John Wiley and Sons, New York, 1991.

Steinberg, B.D., "Radar Imaging from a Distorted Array: The Radio Camera Algorithm and Experiments," IEEE. Trans. Antennas Propag., **AP-29**(5) 740-748 (Sept. 1981).

Steinberg, B.D., *Microwave Imaging with Large Antenna Arrays: Radio Camera Principles and Techniques*, Wiley 1981.

Steinberg, B.D., "Scattering from a Multiple Random Phase Screen Model of a Random Inhomogeneous Medium," Accepted subject to revision by JASA (June 1995).

Trahey, G.E., Freiburger, P.D., Nock, L.F., and Sullivan, D.C., "*In Vivo* Measurements of Ultrasonic Beam Distortion in the Breast," Ultrason. Imag. **13**, 71-90 (1991).

Tsao, J. and B.D. Steinberg, "Reduction of Sidelobe and Speckle Artifacts in Microwave Imaging: The Clean Technique," IEEE Trans. Antennas and Prop., Vol. 36, No. 4, April 1988, pp. 543- 556.

Zhu, Q. and B. D. Steinberg, "Large-Transducer Measurements of Wavefront Distortion in the Female Breast," Ultrasonic Imaging **14**: 276-299 (1992).

Zhu, Q. and Steinberg, B. D., "Modeling, Measurement and Correction of Wavefront Distortion Produced By Breast Specimens," Proc. IEEE Int'l Symp. Ultrason. Ferroelec. Freq. Cont., Cannes, Nov. 1994.

Zhu, Q. and B. Steinberg, (1995a) "First experiment of coherent cancellation of refractive artifacts," AIUM, San Fransisco, March 1995.

Zhu, Q. and Steinberg, B.D. (1995b), "Coherent Cancellation of Refraction Artifacts," 20 Int. Symp. on Ultrasonic Imaging and Tissue Characterization (June 1995).

Zhu,Q. and Steinberg,B.D., (1995c)"Correction of Incoherent Wavefront Distortion by Amplitude Compression and Phase Deaberration," Invited paper, submitted to Int'l. J. Sci. Tech. Imaging, Wiley.

6. PUBLICATIONS

Journal Publications

1. Zhu, Q., Steinberg, B. D., "Correction of Incoherent Wavefront Distortion by Amplitude Compression," submitted to the special issue of International Journal of Imaging Systems and Technology (Sept 1. 1995). Invited.
2. Zhu, Q., Steinberg, B. D. and Arenson, R, "Correlation Distance Measurements of the Female Breast," J. Acoust. Soc. Am, 694-705 (August 1995).
3. Zhu, Q. and Steinberg, B.D., "Modeling, Measurement and Correction of Wavefront Distortion Produced by Breast Specimens," Proc. IEEE Ultrasonic Symp. 1613-1617 (December 1994).
4. Hinkelman, L. M., Liu, D-L., Zhu, Q., Steinberg, B. D. and Waag, R. C., "Measurement and Correction of Ultrasonic Pulse Distortion Produced by the Human Breast," J. Acoust. Soc. Am. (97) 1958-1969 (March 1995)

Conference Abstracts

Zhu, Q. and B. Steinberg, (1995a) "First experiment of coherent cancellation of refractive artifacts," AIUM, San Fransisco, March 1995.

Zhu,Q. and Steinberg,B.D. (1995b), "Coherent Cancellation of Refraction Artifacts," 20 Int. Symp. on Ultrasonic Imaging and Tissue Characterization (June 1995).

Correction of Incoherent Wavefront Distortion by Amplitude Compression and Phase Deaberration

Qing Zhu, Department of Radiology and Valley Forge Research Center
Bernard Steinberg, Valley Forge Research Center, The Moore School of Electrical
Engineering, University of Pennsylvania, Philadelphia, PA 19104

ABSTRACT — There are two wavefront distortion problems inside the female breast that are caused by aberration sources of two distinct types, incoherent scattering and coherent interference. Scattering reduces the target strength, broadens the image lobe and raises the background level and therefore lowers the image contrast, while refraction creates coherent multipath interference that produces false targets or image artifacts in addition to true targets in the image. Scattered energy increases with the propagation depth while refracted energy does not seem to change with the depth. Phase deaberration algorithms partially remove scattered energy and coherently adds it back to the primary field. As a result, the mainlobe diffraction shape is restored to -19.4 dB (std. 2.5 dB) level on average with a net 15 dB (std. 3 dB) improvement compared with that without correction. Because of the strengthening of the primary field and consequently the target strength by the phase-deaberration process, the ratio of peak image artifact to target strength is also improved by an average of 10 dB (std. 4dB) from breast samples that have well-defined multipath artifacts. Backpropagation in addition to phase deaberration can further strengthen the primary field and improve the above numbers by another 5 dB. A compression operation upon wavefront amplitude in addition to phase deaberration or to backpropagation and phase deaberration is introduced in this paper. The operation can further restore the mainlobe diffraction shape to a -30 dB region. Linear regression analysis of sidelobe energy vs. propagation depth indicates that high quality focusing throughout 10 cm thick breast tissue is possible.

I. INTRODUCTION

In principle, high ultrasound resolution can be achieved with very large ultrasound transducers. However, large transducers are more prone to wavefront distortion caused by inhomogeneous tissue because the transducers cover large volumes of tissue and the beams interact with more spatial variations in tissue compositions. The distortion inside the female breast falls into two categories; incoherent scattering reduces the target strength, broadens the image lobe [1-2] and raises the background level and therefore lowers the image contrast [3-4]. Refraction creates coherent multipath interference that produces false targets or image artifacts in addition to true targets in the image [10],[4]. The interference problem is more severe when the aperture is large.

Numerous efforts have been made to correct wavefront distortion produced by breast, liver and abdominal wall [9],[13-17]. Basic deaberration algorithms [5-7] are recognized to be suitable only for weak scattering that can be modeled as a thin random phase screen located in the plane of the receiving aperture [8-9],[18]. Extensions of the basic algorithms are made to correct amplitude distortion caused by strong scattering or distributed scattering [8-9]. A model-based approach, that used *a priori* information of the speeds of the rectus muscle layers inside the abdominal wall, has been developed to correct double image artifacts caused by refraction [17].

The motivation of this study stems from the following. The algorithms [5-9] that require no *a priori* knowledge about the propagating medium function differently upon incoherent scattering and coherent interference; therefore it is important to understand the effects of the two distortion processes upon the image and then apply suitable correction mechanisms to the algorithms. The scattered energy increases with the propagation depth in the breast; therefore the performance of descattering algorithms [5-9] is expected to deteriorate with depth. Finding useful algorithms that can provide good focusing throughout the average propagation depth in the breast, which is approximately 100 mm, is extremely valuable for the next generation high of quality breast scanners.

In this paper we analyze and quantify, through modeling and experiment, image distortion caused by scattering and coherent interference, and the extent to which image quality improvements affected by deaberration. A compression operation on wavefront amplitude, akin to inverse filtering, which can significantly reduce wavefront amplitude variance is introduced. The experimental results show that a combination of the amplitude compression and either phase-deaberration at the aperture or backpropagation plus phase-deaberration at some optimal distance from the aperture can restore the mainlobe diffraction shape to a -30 dB level. Linear regression analysis of sidelobe energy vs. propagation depth indicates that good focusing throughout the 100 mm propagation depth is possible.

Wavefront distortion models as well as the amplitude compression operation are introduced in Section II. Measurement, data processing and correction methods are described in Section III. The experimental results are reported in Section IV. Discussion and conclusion are in Sections V and VI.

II. WAVEFRONT DISTORTION MODELS

A Scattering Models

The wave propagation problem is formulated similarly to the line-of-sight propagation problem through a tenuous distribution of particles [19]. A narrowband wave is used to simplify the description and derivation. An ultrasound wave (either spherical or planar) propagates in an inhomogeneous medium (Fig.1). It consists of coherent and incoherent waves. The incoherent wave is also called a scattered wave. As the wave propagates, the coherent intensity I_c is attenuated due to absorption and scatter, and the incoherent intensity I_i is scattered broadly.

1) Weak scattering

The field E at a receiving aperture is predominantly coherent and the magnitude of the incoherent field is much smaller than that of the coherent field. E is the sum of the coherent and incoherent fields.

$$E(x) = E_c(x) + E_i(x) \quad (1)$$

$$E_c(x) \gg E_i(x) \quad \langle E_c(x_1)E_i(x_2) \rangle = 0 \text{ and } \langle E_i(x) \rangle = 0 \quad (2)$$

where $\langle \rangle$ is the ensemble average and x is the spatial variable at the receiving aperture.

The spatial correlation function or mutual coherence function of the field at the aperture is given by $\Gamma = \langle E(x_1)E(x_2) \rangle$. Since $\langle E_i(x) \rangle = 0$ and $\langle E_c(x_1)E_i(x_2) \rangle = 0$, the spatial correlation function satisfies $\Gamma = \Gamma_c + \Gamma_i$. If the receiver is located in the far field or within the focal region of the source, the angular source intensity distribution or intensity image is the Fourier transform of the spatial correlation function and equals the summation of the coherent and *statistically* smoothed symmetric incoherent spectra (Fig.2(a)). For each realization, however, the incoherent spectrum can have valleys and hills. The Fourier relationship between the incoherent spatial correlation function Γ_i and incoherent spectrum is commonly known as the Van-Cittert Zernike theory [20].

The wavefront distortion is primarily in the phasefront and can be modeled approximately as due to a thin, random phase screen located in the plane of the receiving aperture and defined by a spatial correlation distance. Such distortion is correctable by phase-deaberration or time-delay compensation algorithms [5-7]. The algorithms operate upon the incoherent field. They fold the scattered energy into the coherent field and thereby restore the full diffraction-limited image (Fig.2(b)).

The most relevant wavefront measurement in a weak scattering field is the spatial correlation function of the phasefront or time-delay profile as reported by several groups [1],[16],[21-22]. From this information, the performance of the phase deaberration process can be predicted.

2) Strong scattering or distributed scattering

The coherent component is attenuated and the incoherent component is scattered broadly. Wavefront amplitude is distorted in addition to phasefront distortion. A more suitable representation of the field is the Rytov model. A distributed random distortion medium can be represented as a cascade of thin distortion layers (Fig.3(a)) or phase screens [19]. At the i th layer, the field can be written as $E_i = A_i \exp(j\phi_i)$. Phasefront distortion is developed due to time shift through each layer. Wavefront amplitude distortion is developed as the phase-aberrated wavefront propagates through the medium to successive layers (Fig.3(b)). Let $E_0 = A_0 \exp(j\phi_0)$ be the reference field. The distorted field is then a product of contributions from each layer

$$E(x) = E_0 E_1 E_2 \dots E_i \dots E_N \quad (3)$$

The amplitude of $\frac{E(x)}{E_0(x)}$ denoted as A_t is $A_t = A_1 A_2 \dots A_i \dots A_N$ and the phase $\phi_t = \phi_1 + \phi_2 + \dots \phi_i \dots \phi_N$. Assume that the layers are statistically independent and have common statistics; therefore $A_i = \bar{A} + \delta A_i$ and

$$A_t = (\bar{A})^N \prod_{i=1}^N \left(1 + \frac{\delta A_i}{\bar{A}}\right) = (\bar{A})^N \left(1 + \sum_{i=1}^N \frac{\delta A_i}{\bar{A}} + \text{higher order products}\right) \quad (4)$$

Since \bar{A} is close to unity and $\frac{\delta A_i}{\bar{A}}$, $i=1,2,\dots,N$, are independent variables, the amplitude variance $\sigma_{A_t}^2 \approx N \sigma_{\frac{\delta A}{\bar{A}}}^2$, where $\sigma_{\frac{\delta A}{\bar{A}}}^2$ is the normalized amplitude variance of a single screen. $\sigma_{A_t}^2$ grows linearly with the total number of phase screens N and therefore with the propagation distance D . The phase variance $\sigma_{\phi_t}^2 = N \sigma_{\phi}^2$, where σ_{ϕ}^2 is the variance of a single phase screen; therefore $\sigma_{\phi_t}^2$ grows linearly with N and D .

The overall spectrum (sum of coherent and incoherent spectra) is broadened (see outline of Fig.4(a)) and reduced in strength. The background level is increased and therefore image contrast is reduced. The scattered energy increases with the propagation depth. The energy ratio (ER), which is the energy outside the main image lobe of a distorted image to

the energy inside the main image lobe of the distortion-free image, is a useful tool to quantitatively evaluate the depth-dependence distortion upon image contrast. The relationship between ER and propagation depth D (see Appendix for derivation) is

$$ER = C(\sigma_{\phi}^2 + \sigma_A^2) = CN(\sigma_{\phi}^2 + \sigma_{\frac{\delta A}{A}}^2) = C \frac{D}{d} (\sigma_{\phi}^2 + \sigma_{\frac{\delta A}{A}}^2) \quad (5)$$

where C is a function of the source illumination profile and d is the thickness of the screen and is approximately the correlation distance of the medium. ER linearly grows with the propagation distance. This relationship is analogous to the average sidelobe floor in the radiation pattern of an array with errors [23] and to the average sidelobe floor in an arbitrary source distribution imaged through a distorting medium [18]. Eq. (5) can be adapted to wideband as an approximation.

So long as certain correlation properties exist in the wavefront, phase compensation algorithms are still useful in strong scattering to partially remove phase distortion and build up the strength of the coherent field (Fig.4(b)). Wavefront amplitude distortion remains, as does residual phase distortion, and produces a significantly high incoherent background level in the spectrum. Any phase-deaberration procedure that provides a better phase error estimate than that of the basic algorithms [5-7] can reduce this background level. Wavefront-deaberration algorithms that take amplitude distortion into account can further reduce this background level if the algorithms reduce wavefront amplitude variance.

The dominant scatterer algorithm (DSA) developed in narrowband radar [24] is designed for adaptively focusing a large distorted receiving array upon a point target and is a matched filter process in space. DSA creates a compensating weight vector w from the complex conjugate of the received echo, i.e., $w = A_t \exp(-j\phi_t)$. The DSA corrected receiving beam is the Fourier transform of $w A_t \exp(j\phi_t) = A_t^2$. Consequently, DSA uses wavefront amplitude to provide additional SNR gain than phase conjugation only, for which $w = \exp(-j\phi_t)$. However, when the wavefront amplitude is distorted, the amplitude weight further increases the sidelobe level in the beam. The measure in the increase is the increased wavefront amplitude variance. Since $A_t^2 = A_1^2 A_2^2 \dots A_i^2 \dots A_N^2$, therefore eq. (4) is changed to

$$A_t^2 = (\bar{A})^{2N} \prod_{i=1}^N (1 + \frac{\delta A_i}{\bar{A}})^2 = (\bar{A})^{2N} (1 + \sum_{i=1}^N 2 \frac{\delta A_i}{\bar{A}} + \text{higher order products}) \quad (6)$$

The variance of square amplitude $\sigma_{A_t^2}^2 \approx 4N\sigma_{\frac{\delta A}{A}}^2$ which is 4 times larger than without amplitude weight. Assuming phase error $\sigma_{\phi_t}^2$ is compensated. ER will raise from $C \frac{D}{d} \sigma_{\frac{\delta A}{A}}^2$ to $C \frac{D}{d} 4\sigma_{\frac{\delta A}{A}}^2$ which is about a 6 dB increase in image contrast if the energy is uniformly distributed.

The time reversal mirror (TRM) developed by Fink [8] provides optimal focusing of a wideband transducer upon a target through a scattering medium and is a matched filter process in both space and time (waveform). The operation reverses the received

waveforms, retransmits them through the medium and then focuses the array on the target. The transmitting beam pattern is the convolution of the received waveforms and their time-reversed version. In the frequency domain, TRM is a phase conjugation procedure (with amplitude weight) at each frequency within the signal band. It is anticipated that TRM focusing produces poorer illumination in the neighborhood of the target than phase conjugation focusing does for the reason discussed in the previous paragraph. In the time domain, phase conjugation focusing can be approximated by synthesizing the time-reversed waveforms from sinc waveforms. The spectrum of a sinc waveform is a rectangular function within the signal band.

Square root amplitude weighting changes eq. (4) to

$$A_i^{1/2} = (\bar{A})^{N/2} \prod_{i=1}^N \left(1 + \frac{\delta A_i}{\bar{A}}\right)^{1/2} = (\bar{A})^{N/2} \left(1 + \sum_{i=1}^N \frac{\delta A_i}{2\bar{A}} + \text{higher order products}\right) \quad (7)$$

The amplitude variance $\sigma_{A_i}^2 \approx \frac{N\sigma_{\frac{\delta A}{\bar{A}}}^2}{4}$ which is 4 times less than with unit amplitude weight.

Assuming phase error $\sigma_{\phi_i}^2$ is compensated. ER will reduce from $C \frac{D}{d} \sigma_{\frac{\delta A}{\bar{A}}}^2$ to $C \frac{D}{4d} \sigma_{\frac{\delta A}{\bar{A}}}^2$

which is about a 6 dB decrease in image contrast. Mth rooter will reduce the amplitude variance by 2M. This nonlinear transformation upon wavefront amplitude is a compression operation, and it is an intermediate step between the matched filter process ($M=1/2$) and the inverse filter process ($M \rightarrow \infty$, see Fig.5). The inverse filter process at the aperture corresponds to a deconvolution operation in the image plane, and it is optimal but not stable when the SNR is low. However, as shown in Section IV, low order rooters (square rooter and 4th order rooter), in addition to phase deaberration at the aperture or to backpropagation and phase deaberration at an optimal backpropagation distance can significantly improve ER without encountering stability problem. The detailed evaluation of the effects of this compression operation upon image can be performed by studying the amplitude distributions of images before and after the operation. This is a subject of a later study.

A method recently developed by Liu and Waag [9] backpropagates received wavefronts before the application of time-shift compensation at the distance of back-propagation (BPT). It is a first order correction of waveform distortion produced by propagation. As a result, the waveform similarity increases with the backpropagation distance and reaches its maximum value at the medium surface. The performance of correlation-based algorithms at this backpropagation distance is improved and the residual phase error is reduced.

The relevant measurement in a strong scattering region is wavefront amplitude variance [15] (narrowband) or wavefront energy fluctuation [16],[21] (wideband) in addition to arrival time variance. Since wideband waveforms can be Fourier decomposed into a set of narrowband complex wavefronts within a signal band, waveform distortion therefore implies complex wavefront amplitude distortion and vice versa. In the following text, waveform distortion and wavefront amplitude distortion are used indistinguishably.

B. Strong Scattering and Refraction Model

In a refractive medium coherent rays can be bent and split after they pass through tissue beds with different sound speeds [10]. The interference of refracted coherent ray

bundles with incident rays produces image artifacts which appear as false targets. A simple representation of such a field is

$$E(x) = E_o E_1 E_2 \dots E_i \dots E_N + E_{r1}(x)e^{j f_1(x)} + E_{r2}(x)e^{j f_2(x)} \quad (8)$$

where $f_1(x)$ and $f_2(x)$ define directions of secondary fields caused by refraction (see Fig.6).

The angular source intensity distribution is the superposition of the intensity image lobe, coherent interference lobes and incoherent spectrum (Fig.7(a)). The strengths and the numbers of interference lobes depend on orientations, curvatures, sizes and numbers of refractive bodies in the insonified medium, and may not be directly related to propagation depth. Although the chance of incident rays passing through more refractive bodies increases with the propagation depth, the strengths of interference lobes resulting from multiple refraction may not be significant compared with those resulting from single refraction.

The correction mechanism in a strong scattering and refraction medium is interesting. If the primary field is stronger than secondary refraction fields, the scattered energy removed by the deaberration process strengthens the primary field by folding the removed scattered energy into the primary field. As a result the ratio of image lobe to interference lobe is improved (Fig.7(b)). If, however, the primary field is weaker than the refracted field, the scattered energy removed by the deaberration process may strengthen the refracted field. The corrected result could then be worse than without correction. However, we have seen no evidence of this so far in our experiments reported in Section IV.

TRM or wideband DSA on reception is a matched filter process in both space and time, resulting in maximization of the signal relative to the background white noise. Correlation-based time-delay compensation algorithms, on the other hand, perform a different function; they adjust time-delay to maximize image sharpness or image contrast. In a refractive medium, the problem is more complicated. Neither TRM or wideband DSA nor time-delay algorithms have a way of knowing which signal is real and which is an artifact caused by coherent multipath. Because TRM or wideband DSA is a spatial matched filter its weight vector forms a lobular radiation pattern that matches the sum of both the real and false signals. Hence all targets, whether real or false, are enhanced. In our experiments reported in Section IV, with nine samples that have well-defined multipath artifacts, we found an average 5 dB (std.2.5 dB) increase in peak artifact to image lobe ratio by using wideband DSA rather than by using time-delay compensation.

BPT backpropagates waveforms to the optimum distance before applying time-delay compensation. It removes wavefront amplitude distortion caused by propagation and reduces residual phase distortion by improving the performance of time-delay correction, but will not remove large lobes caused by refraction. A simple thought experiment is convincing: Backpropagating two plane waves produces two plane waves at whatever distance the waves are backpropagated.

Thus it is important to understand the deaberration operations and to design appropriate algorithms that offer optimal performance in the corresponding distorting medium. Aperture measurement alone can not distinguish between wavefront distortions caused by refraction or by strong scattering. Distinction can be made in the image domain where refraction appears as large, coherent interference lobes while strong scattering spreads into an incoherent background. While the refracted energy may or may not be

significantly larger than the energy in the incident wave, it nevertheless produces image artifacts which will destroy the quality of a high resolution image.

III. METHODS

A. *In Vitro Measurement*

The 2-D wavefront measurement system and procedure were described in detail in [16] and are summarized here for convenience. A breast tissue specimen was placed in the specimen holder with the skin facing the direction of the receiving transducer. The source was a hemispherical transducer emulating a virtual point source. The 2-D array consisted of a 92-mm 1-D linear array translated 46 mm perpendicular to its axis to form a synthetic 2-D array 92 mm x 46 mm. The element pitch in the receiving transducer was 0.72 mm and a reflecting mask reduced the receiving elevation to 1.44 mm. Transmission was one-way. Frequency was 3.7 MHz. Bandwidth was 2 MHz. Waveforms were measured at each element, from which 2-D wavefronts were reconstructed as functions of time.

Breast tissue specimens were obtained fresh from reduction mammoplasty surgery and were stored frozen; they were later defrosted and degassed for the experiments. Each specimen was essentially planar and had a surface area of at least $7 \times 11 \text{ cm}^2$. The average thickness was 26.9 mm. The tissue donors were women ranging in age from 18 to 65 with a mean age of 34 years.

Three groups of measurements were made. The primary set consisted of independent measurements using nine different specimens. In addition, two specimens were employed for sequential measurements in which an approximately 1-cm layer was removed from the bottom of the specimen before each subsequent measurement. For three other specimens, a pair of measurements was made with the source in each of two positions located 12 mm apart in the array direction. A total of 16 measurements were made. Water measurement was also made for comparison. In the following analysis, the sequential measurements were treated as measurements from different samples because the samples resulting from approximately 1-cm removal from the original samples were replaced into the sample holder after cutting, and their relative positions to the 2-D transducer aperture was changed unpredictably. The pair measurements resulting from 12 mm lateral source translation were also treated as measurements from different samples because the measured parameters and the point-source image properties were changed due to the highly inhomogeneous nature of the breast tissue.

B. *Data Processing*

Pulse arrival time at each element was calculated by using a differential edge detector to locate the first negative peak of the pulse. Geometric effects were removed by fitting a two-dimensional, fourth-order polynomial to the calculated arrival time surface and subtracting the result. The reasons for using fourth-order polynomial fitting were given in [9]. 3-D image data were calculated by (1) Fourier decomposition of the temporal waveforms at each (x,y) position in the aperture, (2) calculation of a complex CW 2-D image at each Fourier frequency in the focal plane by using the angular spectrum technique [26], and (3) summation of the 2-D images to form the 3-D transient image. The final 2-D image used in this report was obtained by detecting the peak pressure value at each (xf,yf) position in the image plane within the transient period.

The system bandwidth is about 50%; therefore $Q = \frac{f_0}{\Delta f} \approx 2$, where f_0 is the central frequency. For such Q , the first sidelobes (due to finite aperture size) in both principal axes remain [27], and are reduced to about -30 dB level by employing spatial raised cosine taper in step (2)[23].

C. Correction Methods

Two basic phase deaberration algorithms, time-delay compensation (TDC) and phase conjugation (PC), and two wavefront compensation algorithms, wideband DSA and BPT, were applied to each measured 2-D wavefront set and their effects upon focusing were compared. Square rooter and 4th order rooter on wavefront amplitude in addition to PC and square rooter in addition to BPT were also implemented and their effects upon focusing were compared with the other four deaberration algorithms.

TDC: Arrival time fluctuations at the aperture are obtained from cross-correlation peaks of geometrically corrected waveforms and a reference waveform, and are compensated. The selection procedure of the reference waveform is similar to the one developed in [9]. The initial reference waveform with good signal to noise ratio is selected from the geometrically corrected pulses and continuously modified to reduce the effect of the arbitrariness in the selection of the initial reference pulse as waveforms in the aperture are cross-correlated with it. The modification is accomplished by time shifting and adding a new waveform to the reference pulse if the peak value of the correlation function between the new waveform and the current reference pulse is greater than 0.8.

PC: Phase conjugation at each frequency within the signal band (without amplitude weight) provides perfect phase compensation except for a 2π phase jump. The result is better than TDC because of the removal of residual phase error. The wavefront amplitude distortion remains, however. The objective here is to evaluate the limit of phase compensation and the extent of the wavefront amplitude distortion effect. Phase conjugation is implemented at each frequency after Fourier decomposition.

Wideband DSA: Wideband DSA is an approximation of the TRM receive mode developed in [28]. The difference between wideband DSA and TRM receive mode is the scanning procedure. At target position A (Fig.8), wideband DSA and TRM receive mode produce exactly the same responses, because of the reciprocity principle. At non-target position B, wideband DSA uses linear geometry between A and B to scan the beam while the TRM receive mode could backpropagate the wave to the aberrator position, and then use linear geometry to scan the beam [28]. However, for points that are within the correlation distance of A, wideband DSA and the TRM receive mode should produce similar responses. The correlation distance of the breast is about 4-5 mm [16],[29-30]. Therefore within a 4 - 5 mm radius, we should expect similar performances of wideband DSA and TRM receive mode. The objective of using wideband DSA here is to evaluate the possible improvement of deaberration due to the additional SNR gain provided by amplitude weighting. In our experiments, wideband DSA is implemented by using DSA at each frequency after Fourier decomposition.

BPT: BPT developed in [9] is implemented by backpropagating the wavefront to the optimal distance and then using *phase conjugation* at the optimal distance. The use of phase conjugation instead of TDC at the backpropagation distance reduces the complexity in the calculation. The backpropagation distances are taken from [16].

Rooter: PC and square rooter was implemented by conjugation of phase and square root of wavefront amplitude at each frequency after Fourier decomposition. PC and 4th order rooter was implemented by taking 4th root on wavefront amplitude instead of square root. BPT and square rooter was implemented the same as PC and square rooter but the procedure was done at the optimal back propagation distance.

IV. EXPERIMENTAL RESULTS

A. Effects of Scattering and Coherent Interference upon Image

Both scattering and coherent interference phenomena were observed from images of *in vitro* breast samples and their effects upon image quality were evaluated from contour maps of 2-D point source images at different thresholds.

1) Effect of scattering

Figs.9 (a) and (b) show -6 dB contour plots of images obtained from the water path and the 3.5-cm breast tissue path (brs005). Contour spacing is 1 dB. Abscissa and ordinate are azimuth and elevation in mm in the image plane. Fig.9(a) shows the system diffraction pattern at -6 dB. The azimuthal beamwidth is about 1.5 mm (at a distance of 180 mm) meaning that the point (or lateral) resolution is $1.5/180$ or 8.3 mrad. Because the size of the receiving array in elevation is half the size in the array direction, the width of the image in elevation is twice as large as in azimuth. When tissue is present (b), the image lobe is broadened. In (b) the beamwidth has grown from 1.5 mm to 3 mm in azimuth and 3.1 mm to 9.3 mm in elevation and the point resolution has worsened approximately 2:1 in azimuth and 3:1 in elevation. A symmetrical scattering pattern appears when the threshold is reduced. Fig.9 (c) shows a -20 dB contour plot of the sample image brs005. Contour spacing is 2 dB. Energy is spread out over a large area. No distinct structure or multipath lobe can be identified from the image.

2) Effect of scattering and coherent interference

In most breast samples, scattering and coherent interference are both present. Fig.10 (a) and (b) are -10 dB contour plots of images obtained from the water path and the 4-cm breast tissue path (brs006). Contour spacing is 2 dB. In tissue image (b), three lobes instead of one central image lobe appear. Inner contours of the image lobe are close to the system diffraction pattern (Fig.10(a)) while the outer contours are highly irregular due to scattering. The point resolution is worsened by approximately 2:1 in azimuth and 3:1 in elevation. Two refractive lobes appear at (-4, -2.5) and (3.5, 1.5), and their strengths are -6 and -8 dB. A closer examination is obtained from 45 degree cuts (Fig.11) of the Fig.10 (a) and (b) images. In Fig.11 (a), the peak sidelobe is -36dB, which is the best we can obtain from the measurement system. In the tissue image, two large sidelobes (-6 dB and -8 dB) appear on either side of the mainlobe. The two nulls between the lobes are deep (left: -13 dB below peak, right: -15 dB), which is a typical coherent interference phenomenon. The asymmetric interference pattern in Fig.10(b) corresponds to a cut at level B in Fig.7(a).

A symmetric scattering pattern generally appears when the threshold is reduced, as shown Fig.10(c) with a -16 dB threshold contour and contour spacings of approximately 1.5 dB. The outer contours show a roughly symmetric pattern typical of scattering while the inner contours show an asymmetric lobular interference pattern.

We analyzed images at different contour levels and classified the total of 16 samples into three categories: 1) Primarily scatter (4 samples); 2) More scatter than refraction (3 samples); and 3) Scatter plus well-defined refraction (9 samples). Statistics of -6 dB point resolution of three groups is given in Table I. The average beam-broadening as compared with water is 70% in azimuth and 57% in elevation. These numbers are larger than the result reported in [30] where an 18% increase in beamwidth at the same threshold is observed. This is likely due to the different aperture sizes used. For the samples with refractive artifacts, the point resolution is evaluated upon the central image lobe. The percentage increase in beamwidth of the scatter group is significantly larger than that of the other two groups. It is obvious that point resolution is not enough to evaluate image distortion when multiple lobes are present. Statistics of refractive lobes of the third group is given in Table II. In this group, we found 1-3 refractive lobes at levels between -4 and -17 dB (peak value), all within a radius of $1-3^\circ$.

B. Correction of Scattered Energy

1) Correction upon scattering samples

Fig.12 (a)-(g) shows the correction result of the sample image brs005 by using different methods. Part (h) is the -30 dB level contour of a water path image. The contour spacings in Fig.12 are the outer contour levels divided by 10. Fig. 12 (a)-(c) shows TDC at -6, -20 and -30 dB levels (see Fig.9(b) and (c) for comparison). Image quality improved significantly and the system diffraction pattern is restored up to -20 dB level. The symmetric scattering pattern outlined by outer contours at the -30 dB level is caused by residual phase errors after phase deaberration and incoherent amplitude distortion. Fig.12 (d) is the correction result of PC at the -30 dB level. Because of the complete removal of phase errors except for a 2π jump, the scattering pattern is further improved as compared to (c). Fig. 12 (e) is the result of BPT, and the scattering pattern is much better than that of PC at the aperture. The optimum backpropagation distance of this tissue sample is 30 mm. It is interesting to note that the beamwidth is narrower than that obtained through other methods. The reason is that the actual aperture is moved 30 mm closer to the source and the beamwidth is $(R\text{-optimal backpropagation distance})\frac{\lambda}{L}$ instead of $R\frac{\lambda}{L}$, where R is the distance between source and the receiving aperture, and L is the aperture size. Fig.12 (f) is the correction result of PC and square rooter on wavefront amplitude at -30 dB. The pattern is very close to the system diffraction pattern (see (h) for comparison). Fig.12(g) is the result of wideband DSA at the -30 dB level. The correction result is worse than those of other methods. This suggests that amplitude weighting in strong scattering does more harm than good, as discussed in Section II.

2) Correction upon samples with well-defined multipath

Fig.13 shows correction results of the sample image brs006 after applying different methods. The contour spacings are the outer contour levels divided by 10. Fig.13(a) is the -16 dB contour map of applying TDC (see Fig.10(c) for comparison)). Image quality improved significantly because of the minimization of the phasefront distortion caused by scattering. The area within the -16 dB inner contour is reduced by a factor of 11. The mainlobe pattern is close to the system diffraction pattern although the area is still 1.6 times larger than the area in water at the same level. Two large lobes remain as expected and appear as two additional sources. Fig.13(h) is the correction result at a -16 dB level of applying wideband DSA. It is evident that the procedure enhances interference in this example; the artifacts are 5 dB higher than in Fig.13(a). Figs.13(b) and (c) show -25 and -30 dB contour plots of TDC. In Fig.13(b) the outer contours show an asymmetric interference pattern with scattered energy distributed around the two interference lobes. In Fig.13(c) the outer contours show the more symmetric scattering pattern caused by incoherent wavefront amplitude distortion and residual phase distortion. Fig.13(d) is the result of PC at -30 dB. The approximately symmetric scattering pattern outlined by outer contours in (c) is improved due to better phase deaberration. The energy is more concentrated around the image lobe and interference lobes. Part (e) is the result of BPT, and the scattering pattern is further improved as compared with the result of PC at the aperture. The backpropagation distance of this sample is 50 mm. Part (f) is the result of PC and square rooter at -30 dB. The pattern is very close to the system diffraction pattern. PC and 4th order rooter shown in Fig.13(g) restores the diffraction-limited image to a -30 dB level.

It is interesting to note that the strengths of the two interference lobes are also reduced by 8 dB after TDC and PC. They are further reduced by 5, 7 and 15 dB after BPT, PC and square rooter and PC and 4th order rooter, respectively. The improvement comes from the scattered energy which is originally distributed around the mainlobe and each of the

refracted multipath lobes. This energy is coherently added back, by the deaberration process, to the dominant lobe, which in this case is the mainlobe. The overall result is an improvement of the image lobe to the interference lobe ratio.

Determination of whether interference was coherent or scattered was based upon whether or not large lobes could be removed by applying phase-deaberration algorithms. Another indicator is whether or not a lobe location moves (scattering) or remains relatively the same (refraction) after the phase deaberration process. Both means were used to identify whether these lobes were produced by refraction or scattering. Large lobes in nine samples are believed to be caused by the interference process. In these samples, we have found an average of a 10 dB (std. 4dB) improvement in the range of 5-16 dB after TDC, due to the coherent strengthening of the mainlobe.

C. Correction statistics

A simple metric, the lowest level at which mainlobe diffraction shape is maintained, is used here to quantitatively evaluate improvement upon image quality by using different correction algorithms. The mainlobe diffraction shape is identified when the elevation-image width to the horizontal width is approximately a 2 to 1 ratio and the outermost image contour has an elliptical shape. This metric is closely related to contrast resolution. For a simple scattering case, the mainlobe is broadened and deformed in shape (see the outline of Fig.4 (a)). The descattering algorithms partially remove the scattered energy and coherently add it back to the primary field, and therefore restore the mainlobe diffraction shape or beamwidth to a certain level (level A_c in Fig.4 (b)). The difference between A and A_c in Fig.4 is the net improvement. For a complicated scattering and multipath case, the descattering algorithms can restore the mainlobe shape to a certain level (see B_c in Fig.7(b)) but the strength of the large interference lobe may be higher than this level. Therefore a meaningful level of mainlobe diffraction shape should be the level above the artifact which is A_c in Fig.7(b). The net improvement is $A - A_c$ in Fig.7.

The average levels (std. dev) of the restored mainlobe diffraction shape before and after corrections of the three groups classified earlier are given in Table III. The mainlobe shape is restored up to -19.3 (2.4) and -19.5 dB(2.6 dB) by using two phase-deaberration algorithms, TDC and PC, respectively. The fact that the correction result of TDC is very close to that of PC suggests that the limit of phase correction with respect to the selected metric has been achieved by TDC. Further improvement requires correction algorithms that can take wavefront amplitude distortion into account. Wideband DSA is able to restore the mainlobe shape to -14.8 dB(2.3 dB). This result is about 5 dB worse than that of using two phase-deaberration algorithms. The reason is the improper wavefront amplitude weighting. BPT at an optimal backpropagation distance improves the performance of PC at aperture by 5 dB. PC and square rooter on wavefront amplitude restores the mainlobe diffraction shape to -25.4 dB (2.6 dB). The correction result of BPT is similar to PC and square rooter. PC and 4th order rooter achieves a -31.1 dB (1.7 dB) level, which is about a 12 dB improvement more than that of using two phase deaberration algorithms. This level is very desirable for a high quality ultrasound echo scanner. BPT and square rooter at an optimal backpropagation distance further improves the BPT by another 5 dB.

The restored mainlobe diffraction levels among different groups are similar when different correction methods are used. But the improvements are, in general, 6 dB larger in the scatter group than that of the other two groups because the mainlobe shape is distorted at zero dB in the scatter only group.

C. Depth-dependent Distortion and Correction

The scattered energy increases with the propagation depth D . The quantitative measures at the aperture are wavefront amplitude variance $\sigma_{A_t}^2$, and phase variance or arrival time variance σ_t^2 . $\sigma_{A_t}^2$ is calculated as follows: 1) calculate energy at each (x,y) position at the aperture by summing up the energy over the time window; 2) calculate amplitude at each (x,y) position by taking the square root of the energy; 3) calculate the reference amplitude profile which is the fourth order polynomial fit of the measured amplitude profile; and 4) calculate normalized amplitude variance of the measured amplitude profile divided by the reference amplitude profile. The calculation of σ_t^2 is described in Section III.C. Fig.14 shows the linear regression plots of $\log(\sigma_t^2)$ and $\log(\sigma_{A_t}^2)$ vs. $\log(D)$. The correlation coefficients are 0.55 and 0.74, respectively. Two outliers are removed from (a). The slopes are in the order of unity. In both plots, the linear relationships are statistically significant*.

A quantitative measure of scattered energy at the image plane is the energy ratio ER introduced in eq. (5). ER is directly related to image contrast and is measured by: 1) measure the energy outside the mainlobe region in each tissue image; 2) measure the energy inside the mainlobe region of the distortion-free water image; and 3) calculate the ratio. The energy in both tissue and water data sets are equalized. The mainlobe region is identified by linear extrapolation between the peak image value and the outer contour of the mainlobe diffraction pattern at the lowest recognizable level. Fig.15 illustrates the measurement procedure. Fig.16(a) upper curve is the linear regression plot of ER vs. D . The correlation coefficient is 0.68 and the linear relationship is significant. ER in water image is 0.088, which is included in the data points to represent system performance at zero depth.

The performances of descattering algorithms deteriorate with propagation depth. The rest of the regression curves in Fig.16 (a) show ER vs. propagation depth obtained by using five different correction methods. ER in water image after PC is 0.004 which is included in all data sets to represent the calibrated ER at zero depth. The correlation coefficients of regression curves are indicated in the figure by R. The average values of ER (std. dev.) are given in Table IV. The linear relationships are statistically significant for all curves.

The performance of wideband DSA is the worst among all correction procedures. Regression curves of wideband DSA and PC are approximately parallel to each other but PC reduces ER by an average of 10%. The average ratio of ER after DSA over ER after PC is 1.6 which is about 2.4 times less than that predicted by eq.(5). However, the theory is derived for narrowband and can only be used as an approximation for wideband. At 100 mm depth, ER after PC reaches 0.57, which is about the average of ER without correction (see first column of Table IV). Therefore, the best linear phase correction procedure at the aperture is unlikely to be useful at this depth. The average ER after TDC is 5% more than that of PC while the averages of the lowest level at which mainlobe diffraction shape is maintained are the same when TDC and PC are used. This implies that the residual phase

* The linear relationship is statistically significant ($\alpha=0.05$) if the correlation coefficient is greater than 0.53 for sample size 14 and 0.497 for sample size 16.

error due to imperfect phase correction contributes primarily to energy in the sidelobe region. BPT reduces the average ER by 7% below that of PC and is the best among the linear operations. The performance of PC and square rooter at the aperture is slightly better than that of BPT. At 100 mm, both curves reach 0.30 which is about the average level of wideband DSA (see second and third columns of Table IV) obtained from the average 2.7 cm propagation depth. This energy ratio is only useful for good image contrast beyond -15 dB (see Table III).

Fig. 16 (b) shows the results of ER by using BPT and square rooter and PC and 4th order rooter at the aperture. Regression curves obtained from PC and square rooter and BPT are also included in (b) for comparison. At 100 mm depth, the regression curves of BPT and square rooter and PC and 4th order rooter reach 0.12 and 0.07, respectively. These ERs are about the average levels of BPT and PC and square rooter obtained from the average 2.7 cm propagation depth (see Table IV). The result indicates that focusing with very high image contrast beyond -25 dB throughout the 100 mm propagation depth is achievable by taking the low order root on wavefront amplitude in addition to phase deaberration at the aperture or in addition to BPT.

Refracted energy exhibits a different depth distortion effect than scattered energy. The refracted energy may not increase with propagation depth as discussed before. One quantitative measure of coherent interference phenomenon is the ratio of a large interference lobe or artifact to image lobe. For nine samples that were determined to have significant levels of coherent interference, the ratio varied randomly from sample to sample and showed no increase with thickness. The average strength (peak value) is 10 dB (std. 4dB). Another quantitative measure is the total number of large refractive lobes in each image. The average is 2 and standard deviation is 0.53. The lobe number is independent of propagation depth. The refractive lobes are tightly clustered around the main lobe with an average radius of 5.6 mm (std. 1.8 mm) which is about 2 degrees. This is because the speed variations across glandular tissue and fat boundaries are small (5-10%).

Lastly, the significance of appropriate amplitude weighting discussed in Section II is experimentally demonstrated. When phase error is removed, ER is proportional to $\sigma_{A_t}^2$. Fig.17 shows regression plots of ER, measured after reducing the phase error using PC, wideband DSA and PC and square rooter, vs. $\sigma_{A_t}^2$. Three methods compensate phase errors. The linear relationships are statistically significant. An approximate factor of 2 reduction in ER from amplitude squaring (wideband DSA) to square root of amplitude is approximately achieved throughout the entire 100 propagation depth. The results indicate that intelligent use of amplitude weighting is crucial for improving image contrast.

IV. DISCUSSION

A. Application to diffuse scattering medium

The compression operation upon wavefront amplitude, in addition to phase deaberration or BPT, introduced in the paper is applicable to a diffuse scattering medium. Experiments with square root amplitude weighting and TDC show that ER can be reduced by 3% on average relating to using TDC alone. Further comparison studies of image amplitude distributions before and after compression will be performed to quantify the nonlinear effects upon image quality.

B. Significance of Coherent Interference upon Pulse-echo Imaging

A coherent interference phenomenon was demonstrated in the 1-way transmission model and experiments. Its impact upon 2-way echo scanning is illustrated in Fig.18. A transmitting beam illuminates a tumor or target T (part a). Because of refraction, a

subbeam is split from the original beam and insonifies targets along θ_1 . On reception, if no echo signal is coming back from the targets illuminated by the subbeam (simplest case), the receiving beam upon T (part b) may split in the same fashion as the transmitting beam (reciprocity) and a dual image may result. This simplest case corresponds exactly to the situation in the 1-way transmission model described in Figs. 3 and 6 and experiments reported in this paper, and in [1],[16],[21],[30], where an active point source instead of a passive point target is used. In reality, refracted energy from the targets insonified by the subbeam will arrive at angles of $1 - 30^\circ$ from the target direction and therefore in the sidelobe region of array. The sidelobe level of the receiving beam will be ~ -30 dB as achieved by the procedure described in this paper. The average level of refracted multipath is found to be -10 dB relative to the target image and therefore the average multipath signal level entering the system is $\sim (10+30)$ dB below the echo strength of the illuminated target. The cancellation algorithms [11-12] must suppress these multipath signals to achieve a -60 dB contrast resolution, which is essential for preventing contamination of otherwise black cysts with scattered and/or refracted echo energy and thereby causing them to look like speckled tumors.

V. CONCLUSIONS

The evidence of both scattering and refraction is observed from point source images obtained from *in vitro* breast samples with thickness varied from 1-4 cm. Scattering reduces target strength, broadens the mainlobe and increases background level and therefore lowers the image contrast. Refraction creates coherent multipath interference that produces false targets in addition to the true target in the image. Scattered energy increases with the propagation depth while refracted energy does not appear to increase with the depth.

Phase deaberration algorithms are useful to partially remove scattered energy and build up the strength of the coherent image. As a result, the diffraction-limited image is restored up to -20 dB level for average thickness of 2.7 cm. Better phase deaberration procedures are valuable to improve energy ratio and therefore image contrast. Improvement of a diffraction-limited image to the -30 dB region requires wavefront-deaberration algorithms that can further remove scattered energy caused by wavefront amplitude distortion and consequently strengthen the coherent image. BPT reduces wavefront amplitude variance and provides 5 dB improvement in addition to that of using phase deaberration procedures at the aperture. Wideband DSA increases wavefront amplitude variance and the result is 5 dB worse than that of using phase-deaberration procedures for the tissue thickness studied. A low order root on wavefront amplitude in addition to phase-deaberration at the aperture or BPT can further reduce the amplitude variance and restore the diffraction-limited image to the -30 dB region. Linear regression analysis of ER vs propagation depth indicates that high quality focusing throughout 100 mm propagation depth is possible.

The ratio of multipath artifact to image lobe is improved by an average of 10 dB when phase deaberration is used and further improved by another 10 dB when the low order root upon wavefront amplitude in addition to phase deaberration or in addition to backpropagation and phase deaberration is used. The improvement comes from the coherent build up of the target strength by descattering processes.

ACKNOWLEDGMENTS

The *in vitro* measurements were done with the collaboration of Ms. Laura M. Hinkelman and Prof. Robert C. Waag, Departments of Electrical Engineering and Radiology, University of Rochester, Rochester, who also provided the backpropagation

distance. Invaluable consultation was provided by Dr. Kai Thomenius, Director of Research, Interspec, Inc., Ambler, PA., a division of ATL, in the course of this study. Funding was provided by the Army (DAMD 17-93-J-3014 and DAMD 17-94-J-4133), NSF (BCS92-09680).

APPENDIX

Let $s(u)$ represent the complex angular source distribution, where $u = \sin(\theta)$ and θ is the angle from the array normal. Its complex radiation field in the axis of the receiving array in a homogeneous medium is the inverse Fresnel transform of $s(u)$ or inverse Fourier transform of $s(u)$ after correcting for near-field curvature and is denoted as $E_o(x)$. In an inhomogeneous medium, the radiation field is $i(x) = \alpha W(x)E_o(x)M(x)$ where $w(x)$ is the aperture weighting function, $M(x) = A_t \exp(j\phi_t)$ is the medium induced distortion and α is a constant to reflect any signal loss. The complex image is

$$\hat{s}_i(u) = \alpha F[W(x)E_o(x)M(x)] = \alpha f(u) * s(u) * F(M(x)) \quad (1)$$

where $F(M(x)) = \mu(u)$ is the angular impulse response of the medium. F denotes Fourier transform. The subscript i denotes inhomogeneous medium. For $\alpha = 1$ and $M(x) = 1$, the complex image corresponds to the image in homogeneous medium and is denoted as $\hat{s}_h(u)$.

The derivation is made with discrete rather than continuous variables. Thus x is replaced by $n=1, 2, \dots, N$, where N = number of elements in the array. The following assumptions are made:

1. Medium induced amplitude and phase errors are uncorrelated.
2. The phase errors of $\phi_t(n)$, $n=1, 2, \dots, N$, are statistically uncorrelated random variables with a common probability density function (pdf).
3. The amplitude errors of $A_t(n)$, $n=1, 2, \dots, N$, are statistically uncorrelated random variables with a common pdf.

The complex image $\hat{s}_i(u)$ can be written as

$$\hat{s}_i = \alpha F[E_o(n)A_t(n)] = \alpha \sum_{n=1}^N E_o(n)A_t(n) \exp(jkndu) \quad (2)$$

where the aperture taper $W(n)$ has been chosen as unity.

The image intensity is the product of (2) and its complex conjugate:

$$\begin{aligned} \hat{s}_i(u) \hat{s}_i^*(u) &= \alpha^2 \sum_{n=1}^N \sum_{m=1}^N E_o(n)E_o^*(m)A_t(n)A_t(m) \exp(j(\phi_t(n) - \phi_t(m))) \exp(jk(n-m)du) \\ &= \alpha^2 \left\{ \sum_{n=m}^N E_o(n)E_o^*(n)A_t^2(n) + \right. \\ &\quad \left. \sum_{n \neq m}^N E_o(n)E_o^*(m)A_t(n)A_t(m) \exp(j(\phi_t(n) - \phi_t(m))) \exp(jk(n-m)du) \right\} \end{aligned} \quad (3)$$

The average intensity is

$$\begin{aligned}
\overline{\hat{s}_i(u) \hat{s}_i^*(u)} &= \alpha^2 \left\{ \sum_{n=m}^N E_o(n) E_o^*(n) \overline{A_t^2(n)} + \right. \\
&\quad \left. \sum_{n \neq m}^N E_o(n) E_o^*(m) \overline{A_t(n) A_t(m) \exp(j(\phi_t(n)) \exp(-j\phi_t(m)) \exp(jk(n-m)du))} \right. \\
&= \alpha^2 \left\{ \sum_{n=m}^N E_o(n) E_o^*(n) (\sigma_{A_t}^2 + (\overline{A_t})^2) + \sum_{n \neq m}^N E_o(n) E_o^*(m) (\overline{A_t})^2 \overline{\exp(j(\phi_t)^2)} \exp(jk(n-m)du) \right\} \quad (4)
\end{aligned}$$

where $\overline{A_t(n) A_t(m)} = \overline{A_t(n)} \overline{A_t(m)} = \overline{A_t}^2$ and $\overline{\exp(j\phi_t(n)) \exp(-j\phi_t(m))} = \overline{\exp(j\phi_t(n))} \overline{\exp(-j\phi_t(m))} = \overline{\exp(j\phi_t)^2}$ because of the assumptions 2 and 3, respectively.

$$\begin{aligned}
\overline{\hat{s}_i(u) \hat{s}_i^*(u)} &= \alpha^2 \left\{ \sum_{n=m}^N E_o(n) E_o^*(n) (\sigma_{A_t}^2) + \sum_{n=m}^N E_o(n) E_o^*(n) (1 - \overline{\exp(j(\phi_t)^2)}) (\overline{A_t})^2 \right. \\
&\quad \left. + \overline{A_t}^2 \overline{\exp(j(\phi_t)^2)} \sum_{n=1}^N \sum_{m=1}^N E_o(n) E_o^*(m) \exp(jk(n-m)du) \right\} \quad (5)
\end{aligned}$$

The term $\overline{A_t}^2 \overline{\exp(j(\phi_t)^2)} \sum_{n=m}^N E_o(n) E_o^*(n)$ is added to the second term of (4) resulting in the third term of (5). The same term is subtracted from (4) resulting in the second term of (5).

$$\begin{aligned}
\overline{\hat{s}_i(u) \hat{s}_i^*(u)} &= \alpha^2 \left\{ \sum_{n=m}^N E_o(n) E_o^*(n) (\sigma_{A_t}^2) + \sum_{n=m}^N E_o(n) E_o^*(n) (1 - \overline{\exp(j(\phi_t)^2)}) (\overline{A_t})^2 \right. \\
&\quad \left. + (\overline{A_t})^2 \overline{\exp(j(\phi_t)^2)} \sum_{n=m}^N E_o(n) E_o^*(n) \right\} \quad (6)
\end{aligned}$$

Integration with respect to u on both side of eq. (6) yields

$$\begin{aligned}
&\int_{\text{mainlobe}} \overline{\hat{s}_i(u) \hat{s}_i^*(u)} du + \int_{\text{sidelobe}} \overline{\hat{s}_i(u) \hat{s}_i^*(u)} du \\
&= \alpha^2 \left\{ \int_{\text{mainlobe}} \left[\sum_{n=m}^N E_o(n) E_o^*(n) (\sigma_{A_t}^2) + \sum_{n=m}^N E_o(n) E_o^*(n) (1 - \overline{\exp(j(\phi_t)^2)}) (\overline{A_t})^2 \right] du \right. \\
&\quad \left. + \int_{\text{mainlobe}} (\overline{A_t})^2 \overline{\exp(j(\phi_t)^2)} \sum_{n=m}^N E_o(n) E_o^*(n) du \right. \\
&\quad \left. + \alpha^2 \left\{ \int_{\text{sidelobe}} \left[\sum_{n=m}^N E_o(n) E_o^*(n) (\sigma_{A_t}^2) + \sum_{n=m}^N E_o(n) E_o^*(n) (1 - \overline{\exp(j(\phi_t)^2)}) (\overline{A_t})^2 \right] du \right. \right. \\
&\quad \left. \left. + \int_{\text{sidelobe}} (\overline{A_t})^2 \overline{\exp(j(\phi_t)^2)} \sum_{n=m}^N E_o(n) E_o^*(n) du \right\} \right\} \quad (7)
\end{aligned}$$

$$ER = \frac{\alpha^2 \int \sum_{n=m}^N E_o(n) E_o^*(n) du \{ \sigma_{A_t}^2 + (1 - \overline{\exp(j(\phi_t))^2}) \overline{A_t}^2 \}}{\int_{mainlobe} \hat{s}_h(u) \hat{s}_h^*(u) du} \quad (8)$$

where $\int_{sidelobe} (\overline{A_t})^2 \overline{\exp(j(\phi_t))^2} \hat{s}_h(u) \hat{s}_h^*(u) du$ is small compared with the rest of the sidelobe terms and is dropped from the numerator.

The right side of (8) is $C \{ \sigma_{A_t}^2 + (1 - \overline{\exp(j(\phi_t))^2}) \}$, where

$$C = \frac{\int \sum_{n=m}^N E_o(n) E_o^*(n) du}{\int_{mainlobe} \hat{s}_h(u) \hat{s}_h^*(u) du} \text{ which is related to the source properties only. } \alpha^2 \text{ is}$$

dropped because the energy of the distorted image can be equalized to the energy of the distortion-free image. When the phase error is moderate, $1 - \overline{\exp(j(\phi_t))^2} \approx \sigma_{\phi_t}^2$ and $ER \approx C \{ \sigma_{A_t}^2 + \sigma_{\phi_t}^2 \}$.

REFERENCES

- [1] G. E. Trahey, P. D. Freiburger, L. F. Nock, and D. C. Sullivan "In Vivo Measurements of Ultrasonic Beam Distortion in the Breast," *Ultrason. Imag.* 13, 71-90 (1991).
- [2] M. Moshfeghi, and R.C. Waag, In Vivo and in Vitro Ultrasound Beam Distortion Measurements of a Large Aperture and a Conventional Aperture Focused Transducer, *Ultrasound Med. Biol.* 5, 415-428 (1988).
- [3] B.D.Steinberg, "Scattering from a Multiple Random Phase Screen Model of a Random Inhomogeneous Medium," submitted to J. Acoust. Soc. Am. (1995)
- [4] Q. Zhu and B. Steinberg, "Modelling, Measurements and Correction of Wavefront Distortion Produced by Breast Specimens", *Proc. IEEE Ultrasonic Symp.* 1613-1617(1994).
- [5] S. W. Flax and M. O'Donnell, "Phase Aberration Correction using Signals from Point Reflectors and Diffuse Scatterers: Basic Principles," *IEEE Trans. Ultrason., Ferroelec. and Freq. Contr.*, 35(6),758-767 (1988).
- [6] E. H. Attia and B. D. Steinberg, "Self-Cohering Large Antenna Arrays Using the Spatial Correlation Properties of Radar Clutter," *IEEE Trans. Antennas Prop.*, AP-37(1), 30-38 (1989).
- [7] L. Nock, G. E. Trahey, and S. W. Smith, "Phase Aberration Correction in Medical Ultrasound using Speckle Brightness as a Quality Factor," *J. Acoust. Soc. Am.* 85(5), (1989)
- [8] M. Fink, "Time reversal of ultrasonic fields – part I: basic principles," *IEEE Trans. Ultrason. Ferroelec. Freq. Contr.*, vol. 39, pp. 555-566, 1992.
- [9] D.-L. Liu and R. C. Waag, "Correction of Ultrasonic Wavefront Distortion Using Backpropagation and Reference Waveform Method for Time-shift Compensation," *J. Acoust. Soc. Am.* 96, 649-660 (1994).
- [10] Q. Zhu and B. D. Steinberg, "Large-Transducer Measurements of Wavefront Distortion in the Female Breast," *Ultrason. Imag.*, 14, 276-299 (1992).
- [11] Q. Zhu, and B. D. Steinberg, "First Experiments of Coherent Cancellation of Refractive Artifacts," 39 AIUM Proceeding (1995)

- [12] Q. Zhu and B. Steinberg, "Coherent Cancellation of Refraction Artifacts," 20 Int. Symp. on Ultrasonic Imaging and Tissue Characterization (June 1995).
- [13] M. O'Donnell and S. W. Flax, "Phase Aberration Measurements in Medical Ultrasound: Human Studies," *Ultrasonic Imaging*. 10(1), 1-11 (1988).
- [14] D.-L. Liu and R. C. Waag, "Time-shift Compensation of Ultrasonic Pulse Focus Degradation Using Least-mean-square Error Estimates of Arrival Time, *J. Acoust. Soc. Am.* 95(1), 542-555 (1994).
- [15] Q. Zhu, Q., B. D. Steinberg and R. Arenson, "Wavefront amplitude distortion and image sidelobe levels – parts II, In vivo Experiments, " *IEEE Trans. Ultrason. Ferroelec. Freq. Contr.* 40(6) 754-762 (1993).
- [16] L. M. Hinkelman, D-L. Liu, and R. C. Waag, Q. Zhu, and B.D. Steinberg, "Measurement and Correction of Ultrasonic Pulse Distortion Produced by the Human Breast", *J. Acoust. Soc. Am.* 97(3), 1958-1969 (1995).
- [17] D. Carpenter and G. Kossoff, "Correction of Distortion in US Images Caused by Subcutaneous Tissues: Results in Tissue Phantoms and Human Subjects," *Radiology* (1995): 563-567, (1995).
- [18] Q. Zhu, Q. and B. D. Steinberg , "Wavefront amplitude distortion and image sidelobe levels – parts I, theory, " *IEEE Trans. Ultrason. Ferroelec. Freq. Contr.* 40(6) 747-753 (1993).
- [19] A. Ishimaru, *Wave Propagation and Scattering in Random Media*, Academic Press, New York (1978).
- [20] M. Born and E. Wolf, *Principles of Optics*, Pergamon Press (1980).
- [21] L. M. Hinkelman, D-L. Liu, L.A. Metlay, and R. C. Waag, "Measurements of Ultrasonic Pulse Arrival Time and Energy Level Variations Produced by Propagation through Abdominal Wall," *J. Acoust. Soc. Am.* 95, 530-541 (1994).
- [22] Y. Sumino and R.C. Waag, "Measurements of Ultrasonic Pulse Arrival Time Differences Produced by Abdominal Wall Specimens," *J. Acoust. Soc. Am.*, 90(6), 2924-2930 (1991).
- [23] B. D. Steinberg, *Principles of Aperture and Array System Design* (Hohn Wiley & Sons, New York, 1976).
- [24] B. D. Steinberg, "Radar Imaging from a Distorted Array: The Radio Camera Algorithm and Experiments," *IEEE Trans. Antennas Prop. AP-29*(5), 740-748 (1981).
- [25] F. Wu, J-L. Thomas, and M. Fink, "Time reversal of ultrasonic fields – part II: experimental results," *IEEE Trans. Ultrason. Ferroelec. Freq. Contr.*, vol. 39, pp. 567-578, 1992.
- [26] J. W. Goodman, *Introduction to Fourier Optics* (McGraw-Hill, New York, 1968).
- [27] B. D. Steinberg and H. Subbaram, *Microwave Imaging Techniques*, John Wiley and Sons, New York (1991).
- [28] C. Dorme and M. Fink, "Steering and Focusing Through Distributed Inhomogeneous Layers," *IEEE UFFC*, in press.
- [29] Q. Zhu, B. D. Steinberg and R. Arenson, "Correlation Distance of the Female Breast," *J. Acoust. Soc. Am.* August (1995).
- [30] P. D. Freiburger, D. C. Sullivan, B. H. LeBlanc, S. W. Smith, and G. E. Trahey, "Two Dimensional Ultrasonic Beam Distortion in the Breast: In vivo measurements and effects," *Ultrason. Imag.* 14(4), 398-414 (1992).

Table I. Statistics of increase in -6 dB beamwidth (percent)

Sample size	Classification	Azimuth	Elevation
4	A	130 (std. 131.3)	100(std. 96.5)
3	B	50 (std. 53.3)	30 (std. 30.0)
9	C	30 (std. 33.3)	40 (std. 42.2)

- A. Primarily scatter
 B. More scatter than refraction
 C. Scatter plus well-defined refraction

Table II. Statistics of refracted lobes from 9 *in vitro* breast samples

	Average	Std.Dev.
Number of refractive lobes	2	0.53
Relative peak strength (dB)	10	4.7
Distance from primary lobe (deg)	1.8	0.57

Table III Statistics of mainlobe diffraction shape

Diffraction pattern (dB)		Diffraction pattern after correction (dB)					
w/o correction	TDC	PC	Wideband DSA	BPT	PC & square rooter	BPT & square rooter	PC & 4th rooter
A	-0(0)	-18.8 (1.9)	-19.0 (2.2)	-14.8 (2.6)	-24.3(2.1)	-25.3(3.0)	-29.5(2.7)
B	-5.8(1.3)	-19.7 (2.3)	-19.7 (3.5)	-14.7 (1.5)	-23.7(0.6)	-25.3(2.1)	-29.3(2.3)
C	-6.1(3.5)	-19.3 (2.7)	-19.6 (2.5)	-14.8 (2.5)	-23.9(2.4)	-25.4(2.5)	-29.3(3.0)

Table IV Statistics of ER before and after corrections

w/o Corr.	TDC	PC	Wideband DSA	BPT	PC & square rooter	BPT & square rooter	PC & 4th order
0.58(0.11)	0.23(0.05)	0.18(0.04)	0.28(0.08)	0.11(0.02)	0.09(0.03)	0.04(0.01)	0.03(0.01)

FIGURES

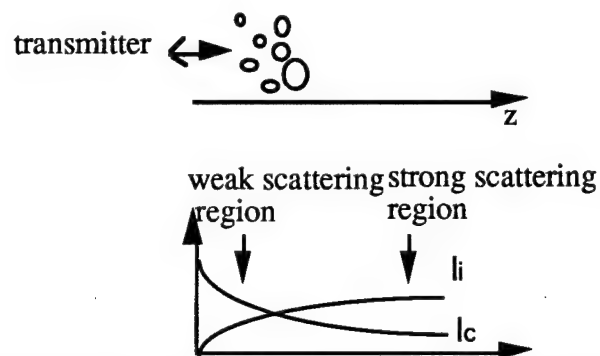


Figure 1. Approximate behavior of the coherent intensity I_c and the incoherent intensity I_i .

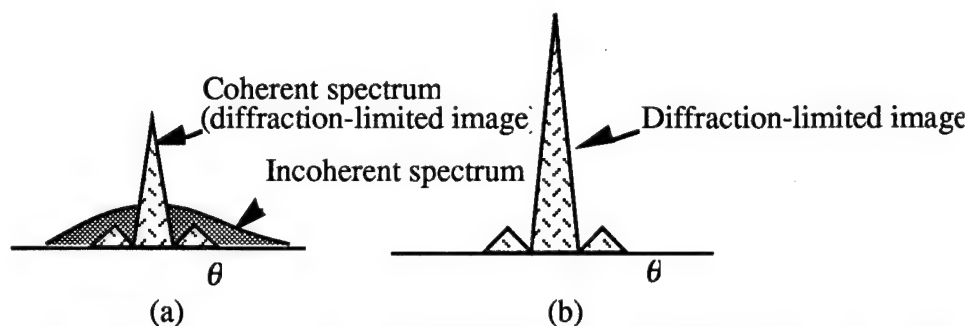


Fig.2. Angular source intensity distribution. Statistical model. (a) Before phase deaberration showing reduced coherent spectrum and of incoherent spectrum. (b) After phase deaberration.

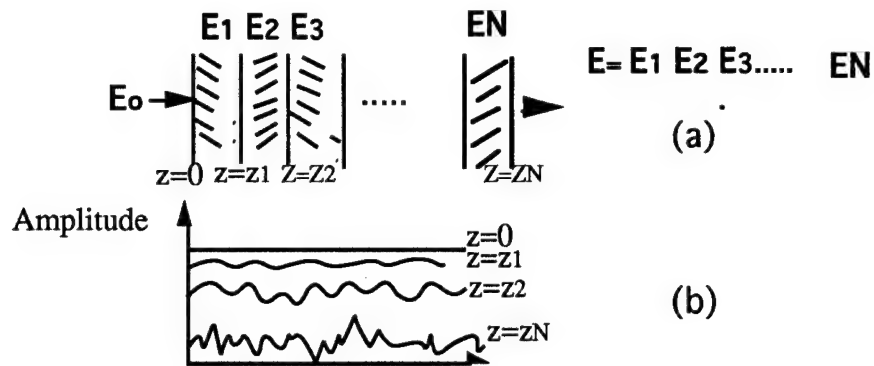


Fig.3 The field is the product of contributions from each layer. Wavefront amplitude fluctuation increases as wave propagates.

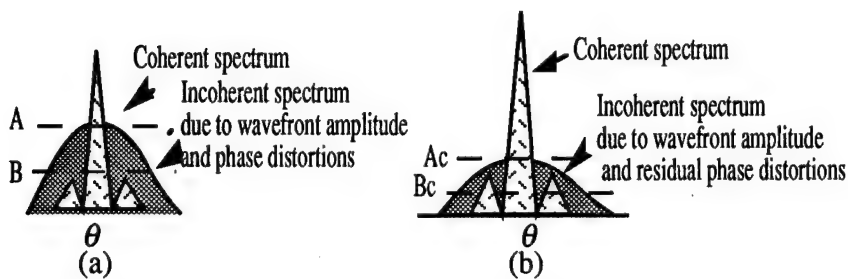


Fig.4. Statistical models of angular source intensity distribution. (a) Before phase correction. (b) After phase correction.

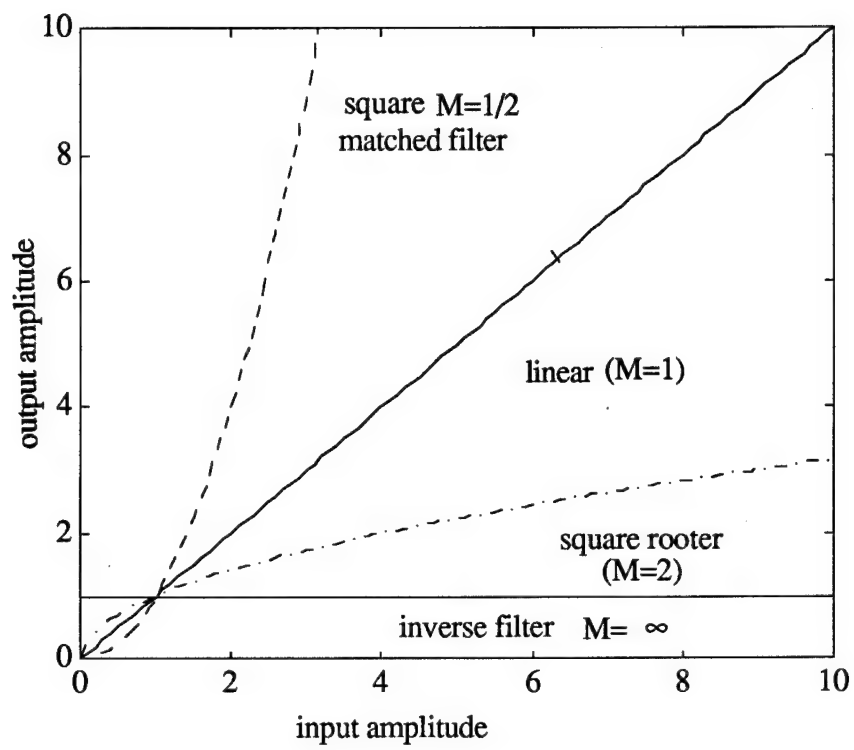


Fig.5. Plots of the input and output amplitude transforms.

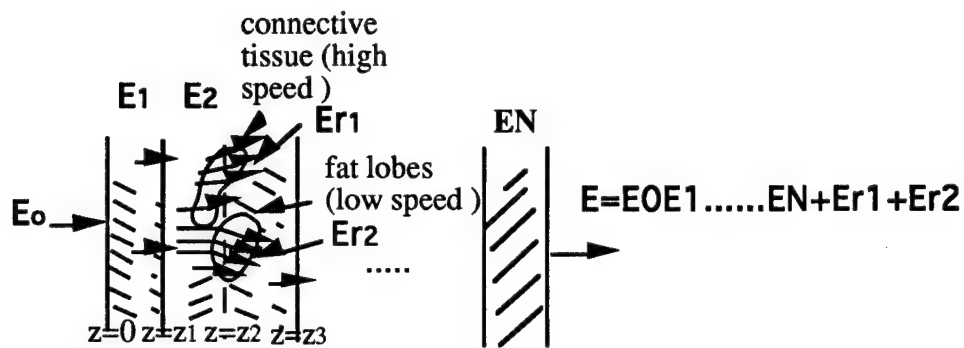


Fig.6 The field is the original field plus refracted fields.

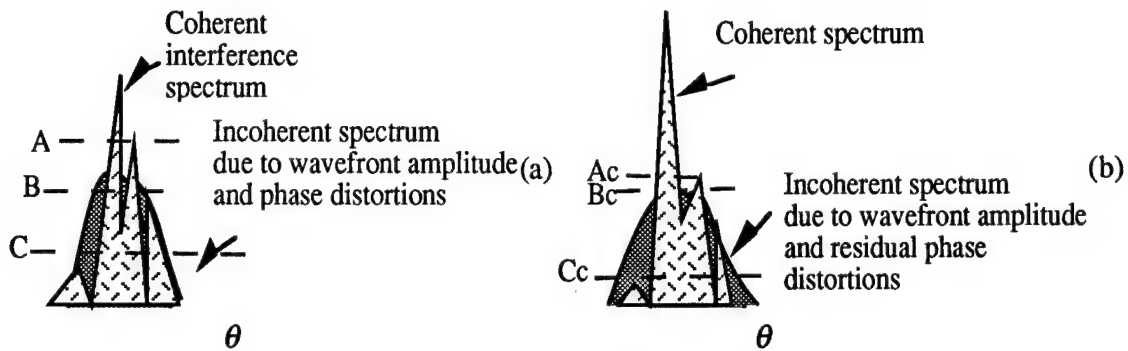


Fig7. (a) Before phase compensation. (b) After.

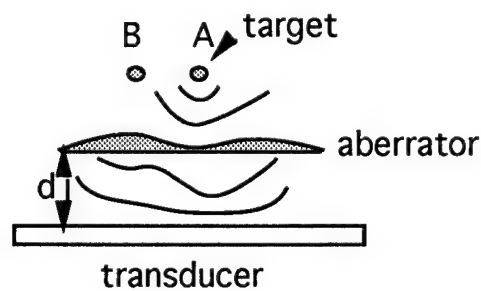


Fig.8. Illustration of scanning configuration.

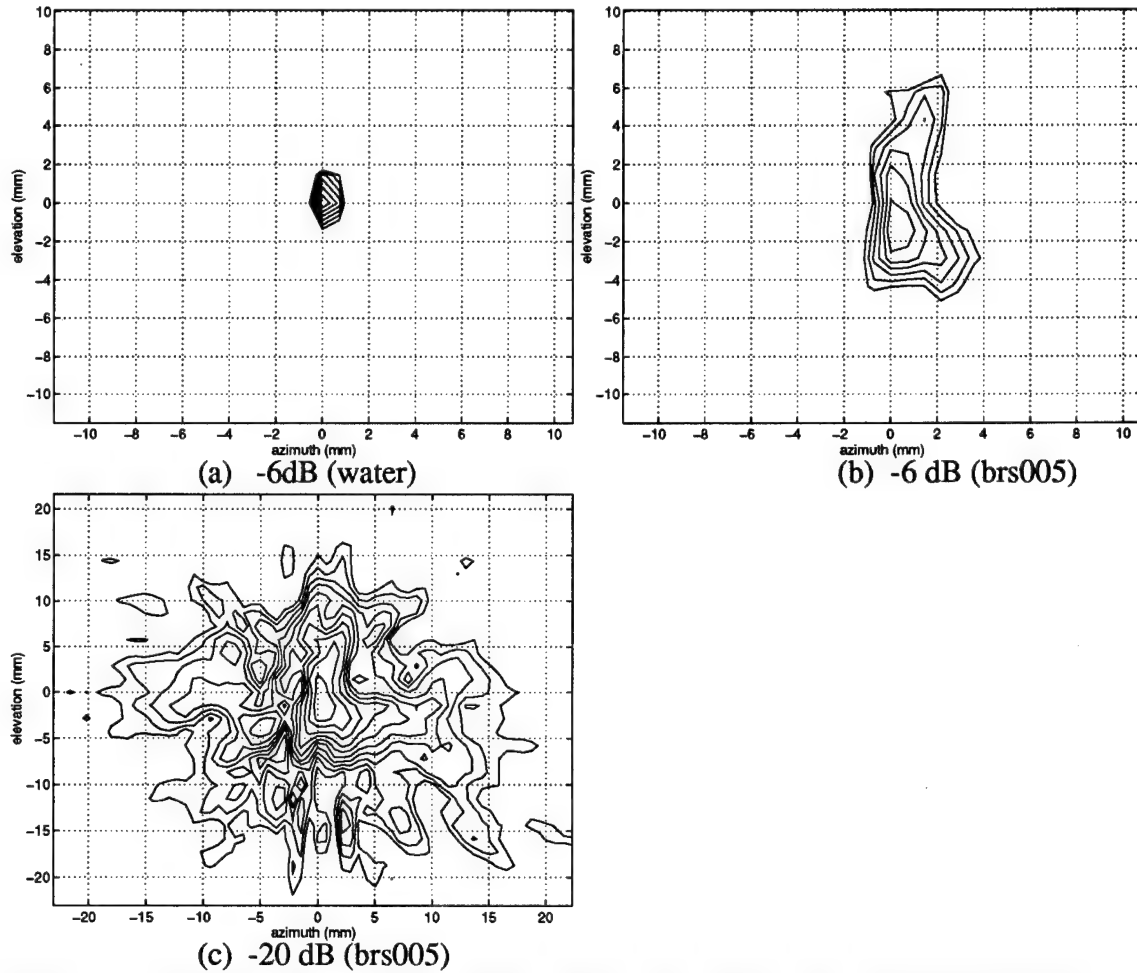


Fig.9. 2-D contour maps of point source images. (a) water data showing diffraction pattern of system. Outer contour is -6 dB level. (b) measured through the 3.5-cm tissue (brs005), showing asymmetric scattering effect. Outer contour is -6 dB level. (c) Image brs005 at -20 dB contour level. The outer contour shows symmetrical scattering pattern. No distinct structure or multipath is observed. Note the change of scale from (a) and (b).

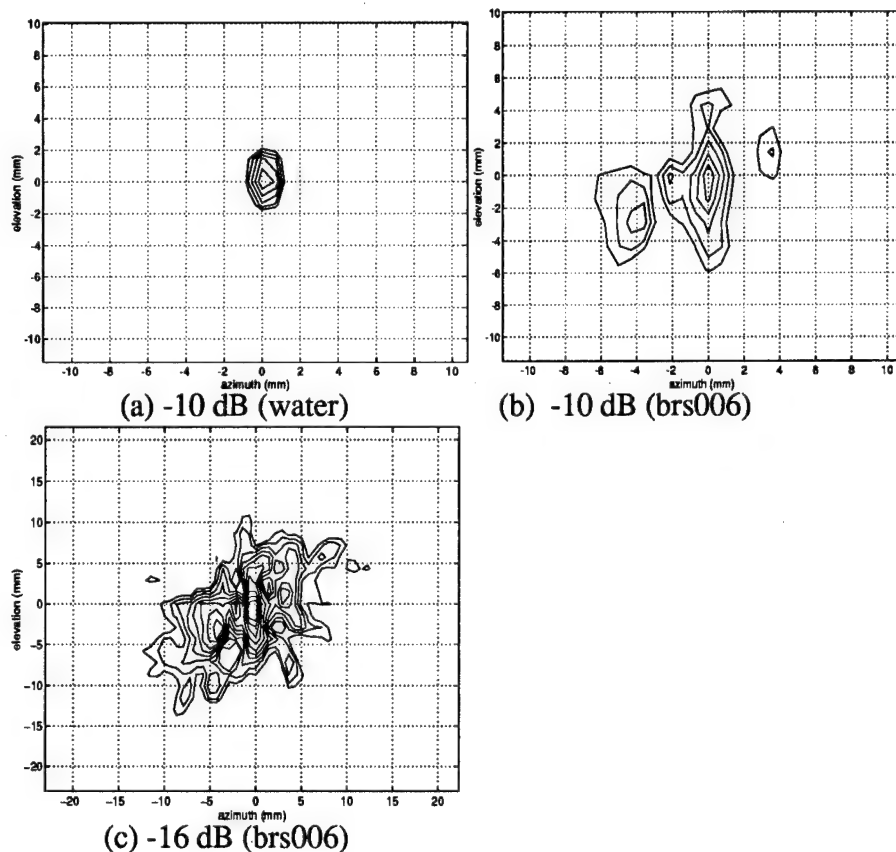


Fig.10. 2-D contour maps of point source images. (a) water data showing diffraction pattern of system. Outer contour is -10 dB level. (b) measured through the 4-cm tissue (brs006), showing highly asymmetric interference pattern. Outer contour is -10 dB level. (c) Image brs006 at -16 dB contour level. The outer contour shows more symmetrical scattering pattern. Note the change of scale from (a) and (b).

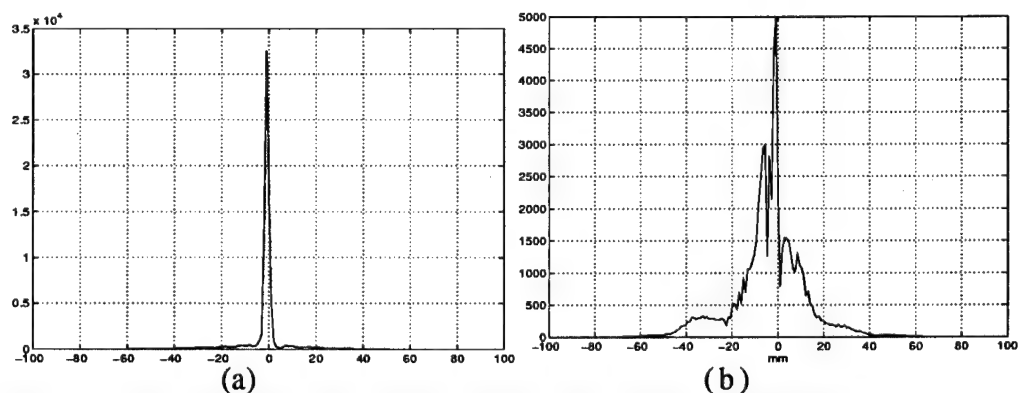


Fig. 11. (a) 45 degree cuts of 2-D images (a) water. (b) brs006.

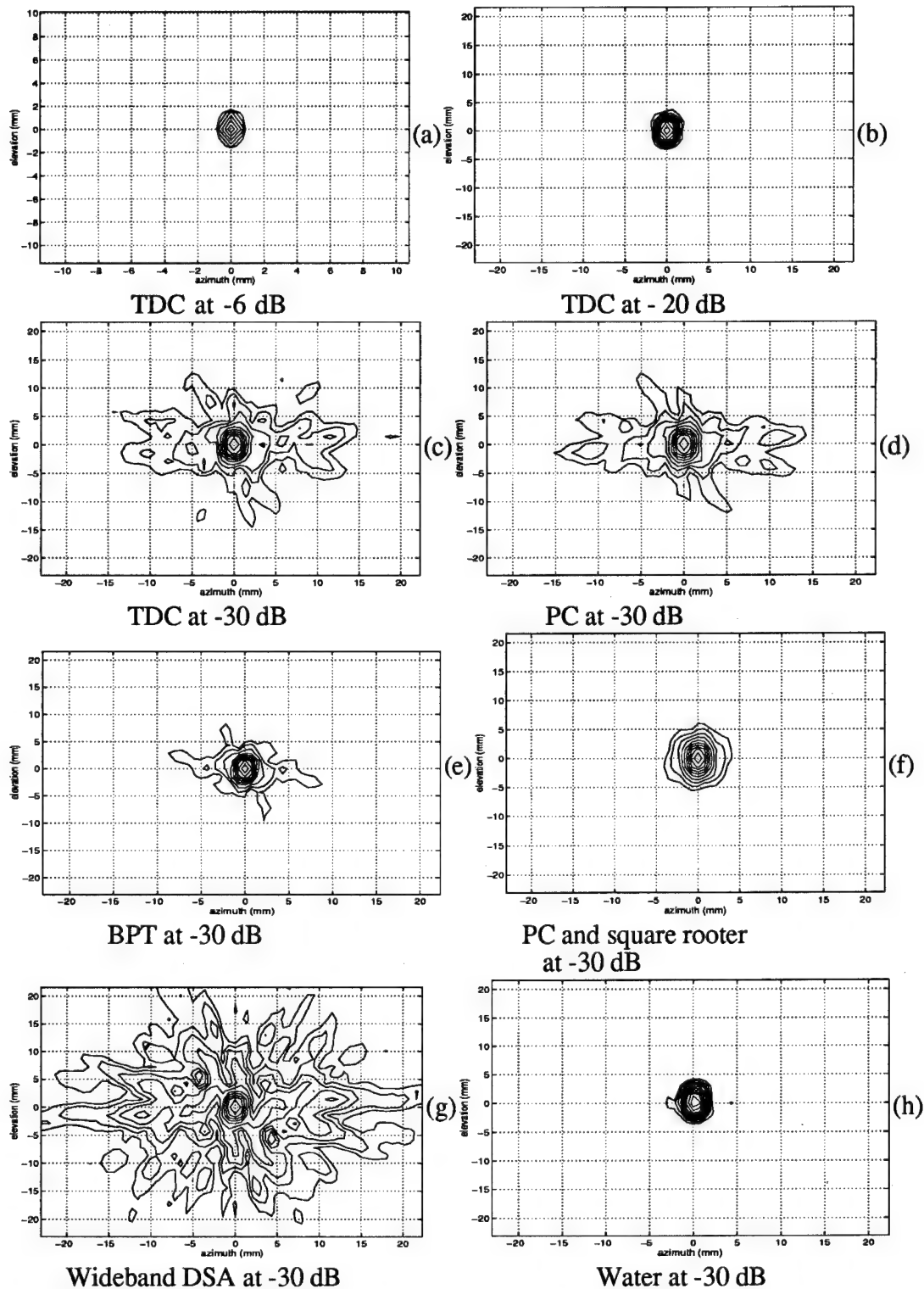
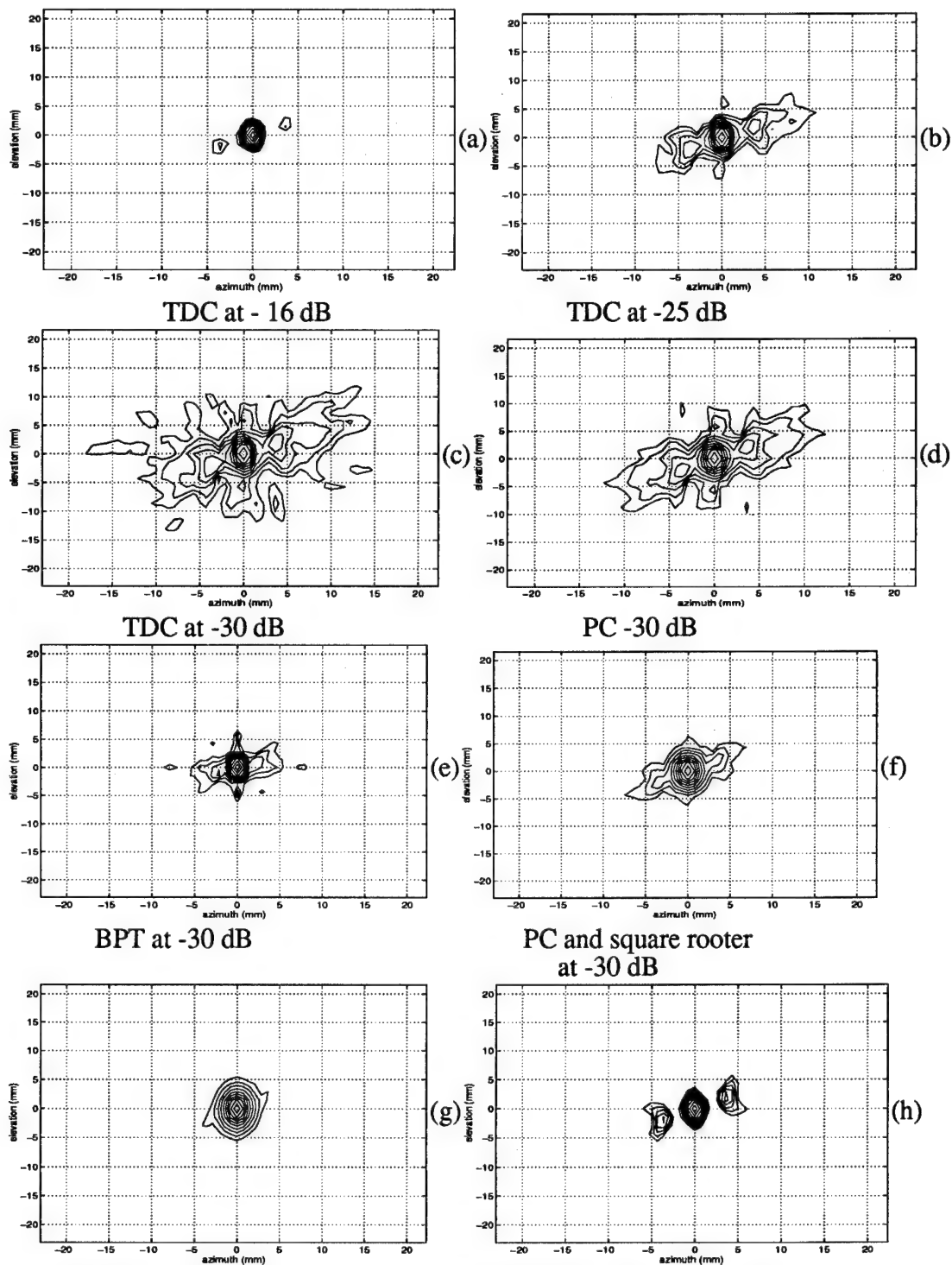
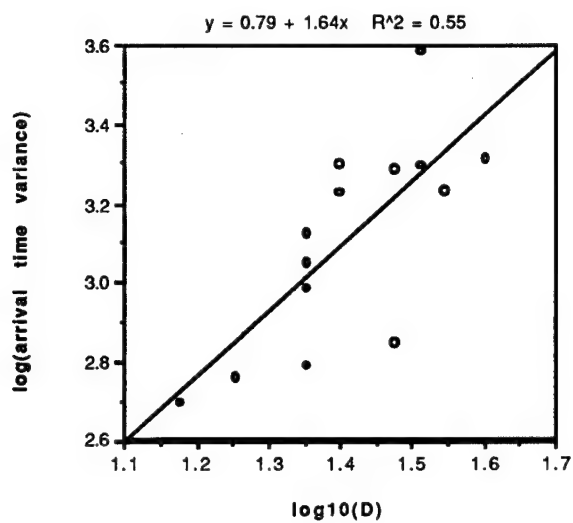


Fig.12. Distortion corrected contour maps of the sample image brs005 (see Fig.9(b) and (c) for comparison) (a) TDC at -6 dB. (b) TDC at -20 dB. (c) TDC at -30 dB. (d) PC at -30 dB. (e) BPT at -30 dB. (f) PC and square rooter at -30 dB. (g) Wideband DSA at -30 dB. (h) Water at -30 dB. Note the scale change of (b)-(h) from (a).

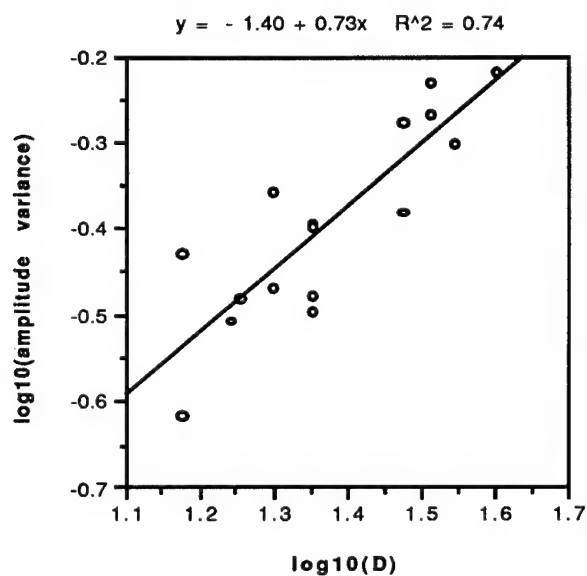


PC and fourth order rooter
at -30 dB

Fig.13. Distortion corrected contour maps of the sample image brs006 (see Fig.10 (b) and (c) for comparison) (a) TDC at -16 dB level. (b) TDC at -25 dB level and (c) TDC at -30 dB level. (d) PC at -30 dB level. (e) BPT at -30 dB. (f) PC and square rooter at -30 dB. (g) PC and fourth order rooter at -30 dB. Wideband DSA at -16 dB. Artifacts are 5 dB higher than time-delayed correction shown in Fig.13(a).



(a)



(b)

Fig.14. Linear regression of (a) $\log(\sigma_{\tau}^2)$ vs. $\log(D)$ and (b) $\log(\sigma_{A_t}^2)$ vs. $\log(D)$. D is in mm, arrival time variance σ_{τ}^2 is in ns^2 and $\sigma_{A_t}^2$ is the normalized amplitude variance (no dimension).

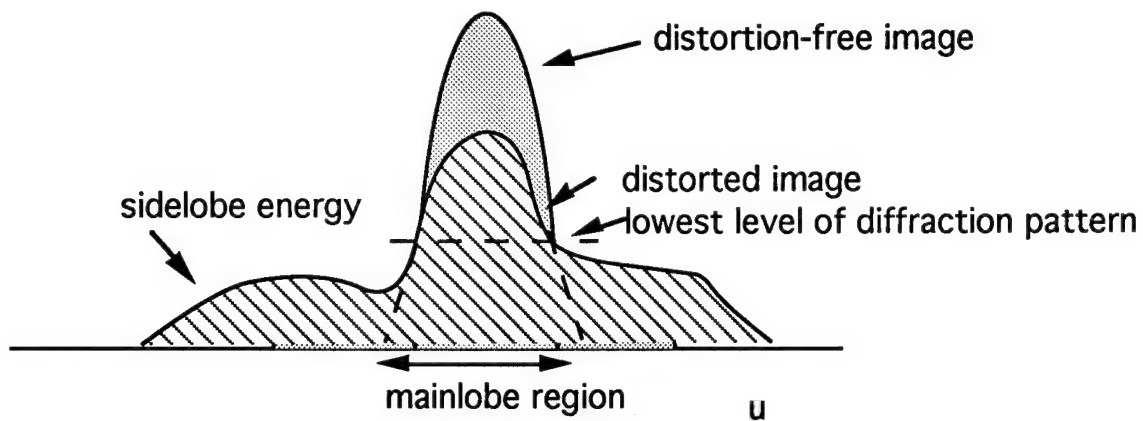


Fig.15. Illustration of ER measurement. Mainlobe region of distorted image is identified by extrapolating between image peak and the lowest level of diffraction pattern (see the two dashed lines). Sidelobe energy of the distorted image is obtained by integrating the energy outside the mainlobe region. The energy inside the mainlobe region of distortion-free image is calculated by finding the mainlobe region of the image and then integrating the energy.

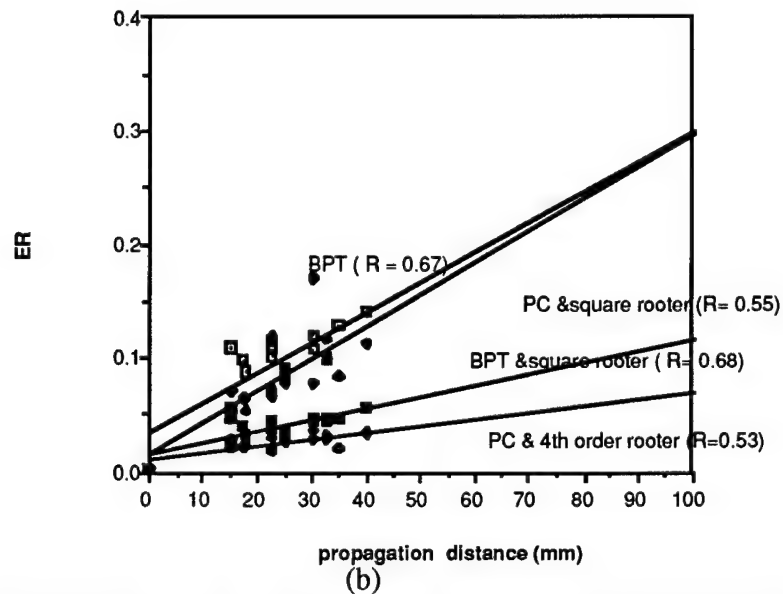
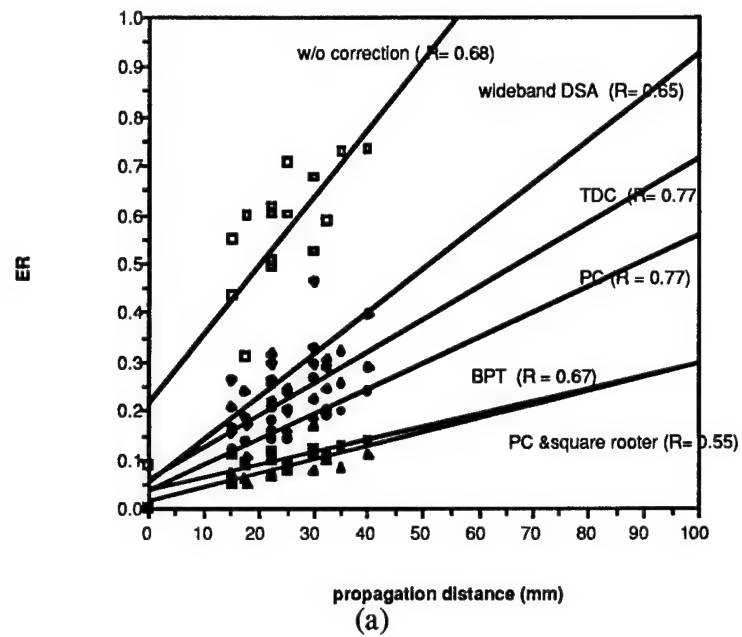


Fig.16. (a) Linear regression curves of ER vs. propagation depth obtained from five correction procedures. (b) Results of ER vs. propagation depth obtained from four correction procedures.

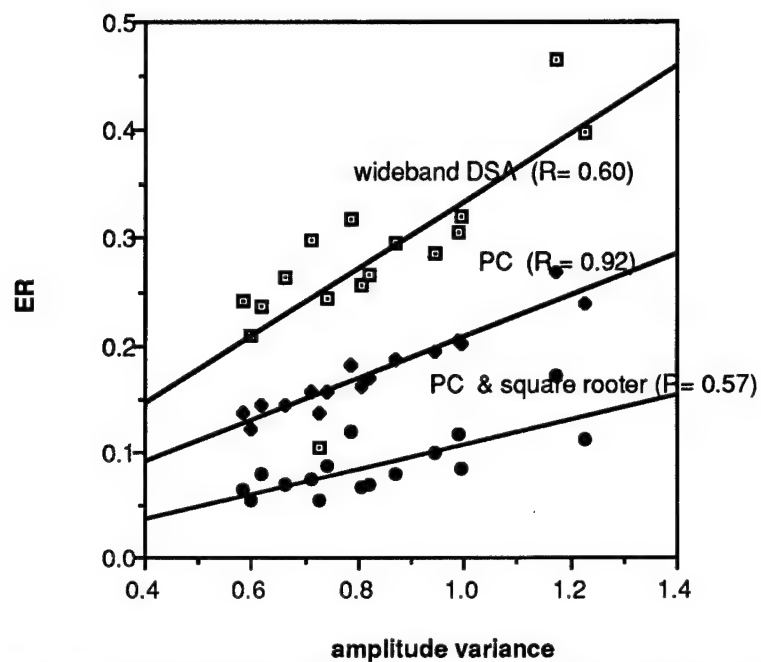


Fig.17. Linear regression plots of ER, after wideband DSA (upper), PC (middle) and PC & square rooter (bottom), vs. wavefront amplitude variance.

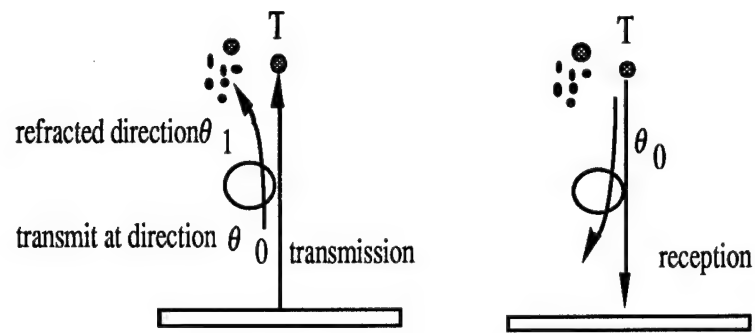


Fig.18. Illustration of effect of refraction upon pulse echo imaging (simplest case with no interference echo signal coming back from targets insonified by subbeam).

Measurement and correction of ultrasonic pulse distortion produced by the human breast

Laura M. Hinkelman and Dong-Lai Liu

Department of Electrical Engineering, University of Rochester, Rochester, New York 14627

Robert C. Waag

Departments of Electrical Engineering and Radiology, University of Rochester, Rochester, New York 14627

Qing Zhu and Bernard D. Steinberg

Valley Forge Research Center, The Moore School of Electrical Engineering, University of Pennsylvania, Philadelphia, Pennsylvania 19104

(Received 29 July 1994; accepted for publication 8 November 1994)

Ultrasonic wavefront distortion produced by transmission through breast tissue specimens was measured in a two-dimensional aperture. Differences in arrival time and energy level between the measured waveforms and references that account for geometric delay and spreading were calculated. Also calculated was a waveform similarity factor that is decreased from 1.0 by changes in waveform shape. For nine different breast specimens, the arrival time fluctuations had an average (\pm s.d.) rms value of 66.8 (\pm 12.6) ns and an associated correlation length of 4.3 (\pm 1.1) mm, while the energy level fluctuations had an average rms value of 5.0 (\pm 0.5) dB and a correlation length of 3.4 (\pm 0.8) mm. The corresponding waveform similarity factor was 0.910 (\pm 0.023). The effect of the wavefront distortion on focusing and the ability of time-shift compensation to remove the distortion were evaluated by comparing parameters such as the -30-dB effective radius, the -10-dB peripheral energy ratio, and the level at which the effective radius departs from an ideal by 10% for the focus obtained without compensation, with time-shift estimation and compensation in the aperture, and with time-shift estimation and compensation performed after backpropagation. For the nine specimens, the average -10-dB peripheral energy ratio of the focused beams fell from 3.82 (\pm 1.83) for the uncompensated data to 0.96 (\pm 0.18) with time-shift compensation in the aperture and to 0.63 (\pm 0.07) with time-shift compensation after backpropagation. The average -30-dB effective radius and average 10% deviation level were 4.5 (\pm 0.8) mm and -19.2 (\pm 3.5) dB, respectively, for compensation in the aperture and 3.2 (\pm 0.7) mm and -22.8 (\pm 2.8) dB, respectively, for compensation after backpropagation. The corresponding radius for the uncompensated data was not meaningful because the dynamic range of the focus was generally less than 30 dB in the elevation direction, while the average 10% deviation level for the uncompensated data was -4.9 (\pm 4.1) dB. The results indicate that wavefront distortion produced by breast significantly degrades ultrasonic focus in the low MHz frequency range and that much of this degradation can be eliminated using wavefront backpropagation and time-shift compensation.

PACS numbers: 43.80.Cs, 43.80.Ev, 43.80.Vj

INTRODUCTION

Widely recognized strengths of ultrasonic imaging techniques for diagnosis and monitoring of breast disease are the nonionizing nature of acoustic waves and the ability to provide good contrast between fluids and parenchymal tissues. However, despite advances in transducer technology, breast ultrasonography has thus far been relegated to ancillary use, largely because resolution is inadequate.^{1,2} This has led to consideration of the limitations imposed on ultrasonic imaging of the breast by wavefront distortion that arises from propagation through breast tissue.

Several researchers have studied ultrasonic distortion produced by the breast and considered how this distortion may be compensated. An early *in vivo* pulse-echo study by Moshfeghi and Waag³ showed that increasing the aperture to $f/1.0$ from $f/2.6$ for breast produced only about $\frac{1}{3}$ the resolution improvement predicted in a homogeneous medium. Trahey *et al.*⁴ made one-dimensional transmission measure-

ments of ultrasonic phase distortion caused *in vivo* by propagation through breast and found an average rms arrival time aberration of 36.1 ns for 22 subjects. The same group later extended their transmission measurements to two dimensions and obtained an rms value of 55.3 ns for seven volunteers.⁵ They concluded that phase distortion should be measured and corrected in two dimensions but did not mention amplitude distortion. In other *in vivo* one-dimensional transmission measurements, Zhu and Steinberg observed severe amplitude distortion, which they attributed to refraction in addition to scattering,^{6,7} and obtained a relation between the average sidelobe floor and the normalized variance of the amplitude distortion produced by the breast.^{8,9} They concluded that large two-dimensional arrays and new algorithms that correct both phase and amplitude distortion in two dimensions may be needed to reduce the effects of distortion produced by the breast.

Two basic algorithms for correction of ultrasonic distor-

tion have been investigated for general imaging applications. The first relies on cross correlation of signals in the aperture for estimation of pulse arrival time,^{10,11} while the other adjusts beamformer delays to maximize signal brightness.^{12,13} However, neither of these methods addresses the problems of amplitude and waveform distortion, since both use only time-shift compensation in the aperture. Another technique has been investigated for the removal of amplitude and waveform distortion as well as time-shift distortion in specialized applications when a point source is present as may be the case in lithotripsy. This technique employs time-reversed signals but is limited because a suitable point source is not generally available in every isoplanatic patch to be imaged.^{14,15} A more recent method developed by Liu and Waag¹⁶ can be used to remove time-shift, amplitude, and waveform distortion in general imaging applications. Their approach models the distorting medium as a phase screen placed some distance from the receiving aperture and removes amplitude and waveform distortion by backpropagation of the wavefront before applying time-shift compensation.

This paper reports a study of ultrasonic wavefront distortion produced by breast and the effectiveness of the back-propagation method in removing the distortion. In the study, wavefronts perturbed by transmission through breast tissue were measured in a two-dimensional aperture. Statistics describing arrival time variations, energy level fluctuations, and wave shape distortion were calculated and compared to values from analogous measurements using abdominal wall.¹⁷ The received waveforms were then focused without compensation, with time-shift estimation and compensation in the measurement aperture, and with backpropagation followed by time-shift estimation and compensation to determine the effectiveness of time-shift compensation with and without wavefront backpropagation for the improvement of focusing.

I. METHOD

Breast tissue specimens were obtained fresh from reduction mammoplasty surgery and were stored frozen if not used immediately for measurements. The specimens came from regions of the breast away from the nipple and consisted of fat, glandular and connective tissue, and a surface covering of skin. Each specimen was essentially planar and had a surface area of at least $7 \times 11 \text{ cm}^2$. The average thickness was 26.9 mm. The tissue donors were women ranging in age from 18 to 65 with a mean age of 34 years.

Measurements were carried out using the procedure detailed in Ref. 17 and summarized here for convenience. A breast tissue specimen was placed in the specimen holder with the skin facing the direction of the receiving transducer and pressurized to 500 psi for 30 min in order to dissolve any gas bubbles present in the tissue. The specimen holder was then mounted in the experimental chamber, which was maintained at $37 \pm 1^\circ \text{C}$ throughout the measurement. Ultrasonic pulses emitted by a hemispheric transducer were received by a 128-element linear array immediately after propagation through the specimen. A two-dimensional area was scanned by translating the array in the elevation direction using an automated stage. At each elevation, the array elements were

accessed sequentially by a multiplexer. The signal from each element was digitized into 12-bit samples for a period of 11.8 μs at a rate of 20 MHz. The signal was recorded 19 times at each element to permit noise reduction through signal averaging. The nominal center frequency was 3.75 MHz for each transducer and the -6-dB bandwidth of the received pulse was about 2.2 MHz. The element pitch in the receiving transducer was 0.72 mm and a reflecting mask reduced the receiving elevation to 1.44 mm. A period of about 35 min was required to record the signals from all 128 array elements at each of 32 elevations spaced 1.44 mm apart for a total of 4096 positions over a $92.16 \times 46.08 \text{ mm}^2$ aperture. The total source-receiver separation was about 165 mm and the specimen-receiver gap was about 8 mm.

Three groups of measurements were made. The primary set consisted of independent measurements using nine different specimens. In addition, two specimens were employed for sequential measurements in which a 1-cm layer was removed from the bottom of the specimen before each subsequent measurement. For two other specimens, a pair of measurements was made with the source in each of two positions located 12 mm apart in the array direction.

Variations in pulse arrival time were calculated using the reference waveform method for arrival time estimation and differences in shape among the received waveforms were quantified using the waveform similarity factor as described in Ref. 16. Energy level fluctuations were calculated as described in Ref. 17. The calculations are outlined here to identify the main steps. A reference waveform was constructed for a set of data as an average of all the waveforms meeting a cross-correlation criterion for similarity. The reference pulse was then cross correlated with each of the original waveforms and an arrival time surface was calculated from the peaks of the correlation functions. Smoothing was done to remove questionable outlying points. A two-dimensional, fourth-order polynomial fit to the estimated arrival times was used to position a window on the original waveforms, and arrival time estimation was repeated using the windowed data. Geometric effects were removed by fitting a two-dimensional, fourth-order polynomial to the newly calculated arrival time surface and subtracting the result to obtain the arrival time fluctuations. Fluctuations in energy level across the received wavefront were calculated by summing the squared amplitudes of the windowed signals at each position, converting the results to decibel units, and subtracting a fitted two-dimensional, fourth-order polynomial from the result. This computation, however, did not employ the 20-dB restriction on the dynamic range as in Ref. 17, since no exceptionally low-energy values occurred. The waveform similarity factor, which ranges from an ideal value of 1 to a minimum of 0 and is insensitive to absolute amplitude and arrival time like a correlation coefficient, was computed for all the windowed waveforms throughout the aperture.

Two forms of compensation for wavefront distortion were applied to compare their effect on focusing. In one, time-shift estimation and compensation were performed directly in the receiving aperture. In the other, time-shift estimation and compensation were performed after the wavefront had been backpropagated to the point of maximum

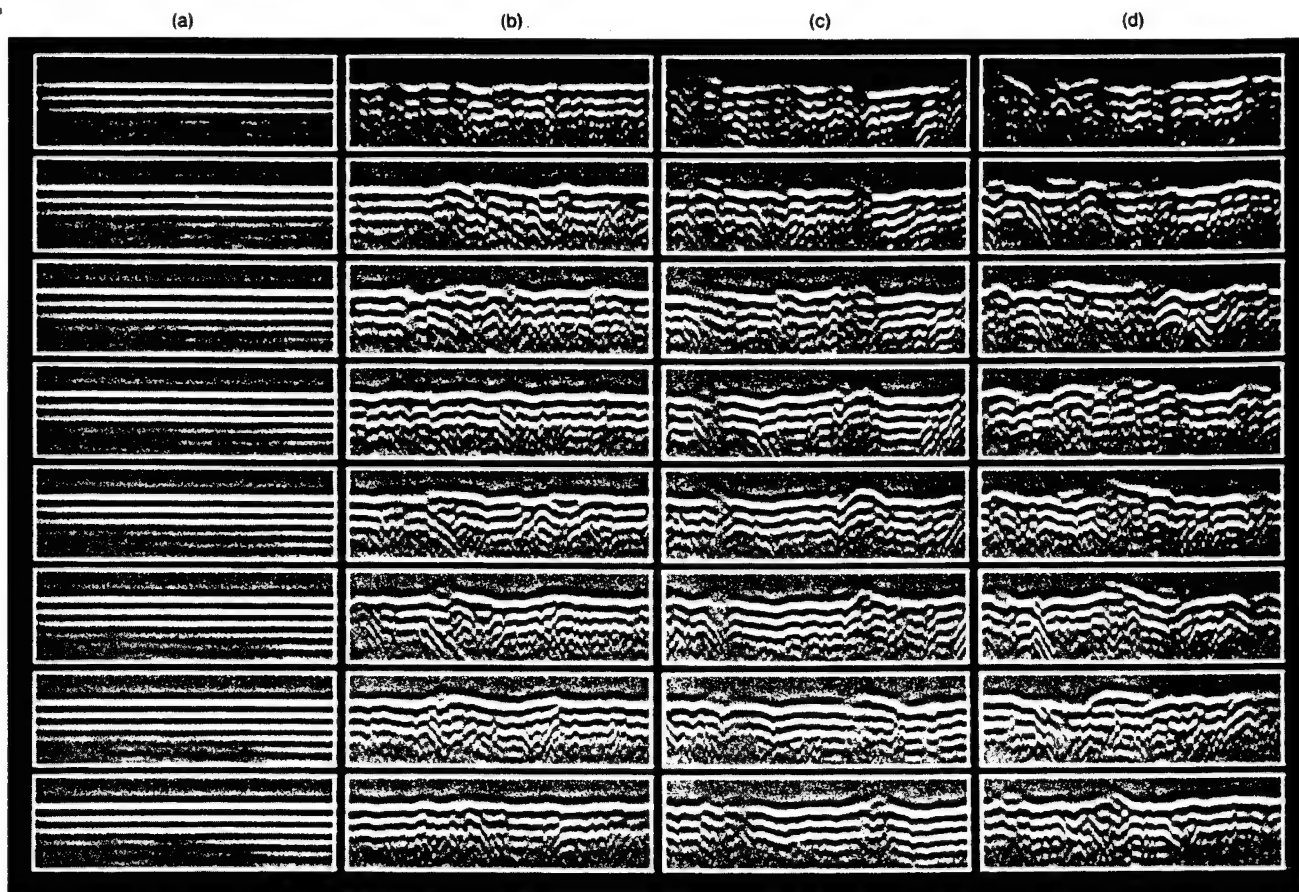


FIG. 1. Representative waveforms compensated for geometric travel time. (a) H_2O . (b) BRS 10. (c) BRS 8a. (d) BRS 8b. Each column of panels shows waveforms at sequential increments of 2.88 mm in elevation across the first half of the 46.08-mm aperture. At each elevation, the horizontal coordinate is the array direction and spans a distance of 92.16 mm in 0.72-mm increments while the vertical coordinate is time and spans an interval of $2.0 \mu s$ in $0.05\text{-}\mu s$ increments. Signal amplitude is shown linearly on a gray scale with the maximum signal in the two-dimensional aperture for each measurement represented by white and the corresponding negative value by black.

waveform similarity. The backpropagation used the angular spectrum method as described in Ref. 16. The reference waveform method was employed in both forms for time-shift estimation.

The efficacy of the two correction procedures, as well as the effect of the original distortion, were evaluated by focusing each set of data at 180 mm via a Fourier transform method as described in Ref. 18. Each focus was described by the -10 , -20 , and -30 dB effective radii, which are half the cube root of the product of the corresponding effective widths in the array, elevation, and time directions. The effective radius several dB down from the peak is a useful measure of point resolution while the effective radius many dB down from the peak is a measure of contrast resolution. The -10 -dB peripheral energy ratio, which is the ratio of energy outside an ellipsoid bounded by the -10 dB effective widths to the energy inside that ellipsoid, was also used to describe each focus quantitatively. Since the energy outside a specified region around the main peak of the focus can be viewed as an integration of sidelobe intensity, the peripheral energy ratio is another measure of contrast resolution. Additionally, each focus was described by the 10% deviation level, which is the level at which the effective radius becomes 10% larger than that produced by ideal waveforms obtained for the data

set by replicating its average time-shift compensated waveform throughout the aperture. This level provides a measure of the degree to which the central region of actual focus is ideal.

II. RESULTS

Representative sets of waveforms recorded after transmission through breast tissue specimens and corrected for geometric arrival time are shown in Fig. 1 with corresponding representative water path waveforms to illustrate the range and combination of distortion levels encountered in this study. The water path waveforms in (a) show minimal arrival time and energy level fluctuation and nearly ideal waveform similarity. The tissue path waveforms in (b) exhibit low arrival time and energy level fluctuation and moderate waveform distortion. The waveforms in (c) have moderate arrival time variation, high energy level fluctuation, and low wave shape distortion. The waveforms in (d) show high arrival time and waveform distortion but moderate energy level fluctuation.

Arrival time fluctuations and energy level fluctuations produced by nine different breast tissue specimens are shown in Fig. 2 and statistics of these data as well as the waveform

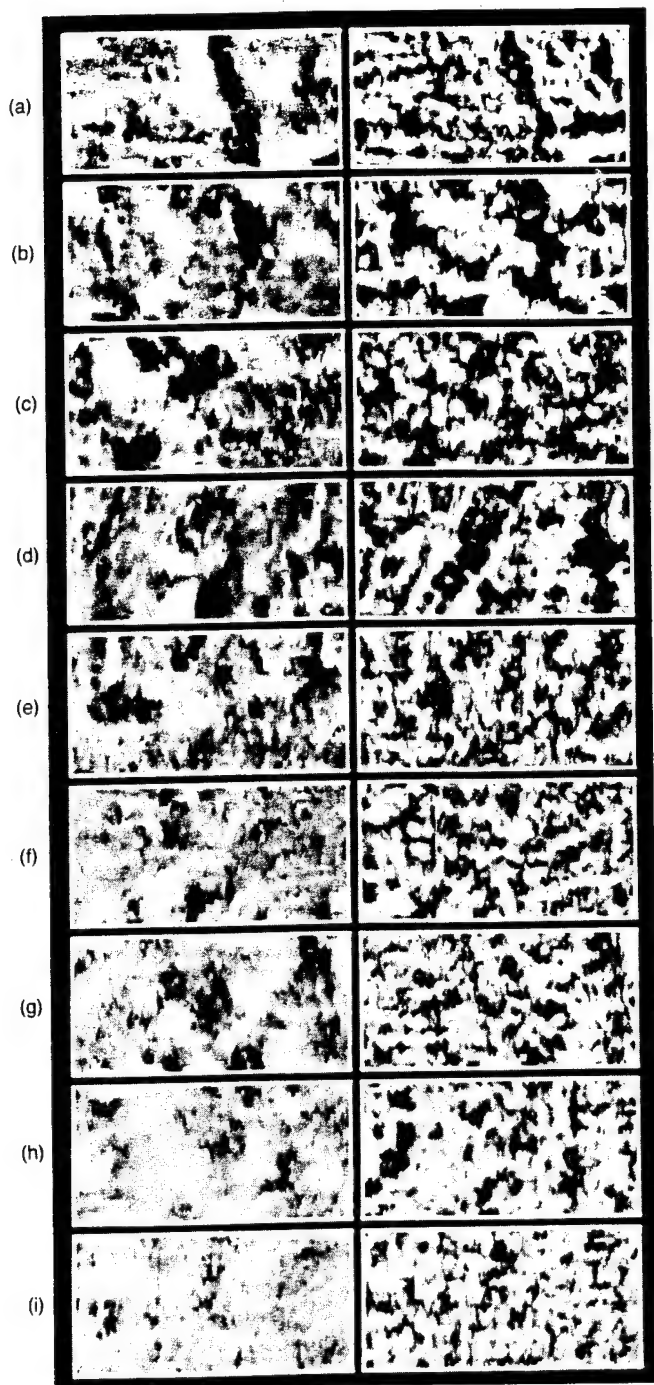


FIG. 2. Breast tissue path arrival time and energy level fluctuations for nine different specimens. (a) BRS 7. (b) BRS 8a. (c) BRS 8b. (d) BRS 9a. (e) BRS 9b. (f) BRS 10. (g) BRS 11. (h) BRS 13. (i) BRS 17. In the left panel of each pair, arrival time difference is shown on a linear scale with a maximum arrival time fluctuation of +150 ns represented by white and a minimum arrival time fluctuation of -150 ns represented by black. In the right panel of each pair, energy level fluctuations are shown on a log scale with a maximum positive excursion of +10 dB represented by white and a maximum negative excursion of -10 dB represented by black. In all panels, the horizontal coordinate is the array direction and spans a distance of 92.16 mm in 0.72-mm increments while the vertical coordinate corresponds to position of the array in elevation and spans a distance of 46.08 mm with points interpolated from measurements at 1.44-mm intervals to produce data at 0.72-mm increments.

similarity factor are given in Table I for each set of measured waveforms. The arrival time and energy level fluctuation patterns produced by a given specimen are roughly similar and the specimen-to-specimen variability is not great. Consistent with these observations, the effective arrival time and energy level fluctuation correlation lengths are similar for each specimen while the average waveform similarity factor has a small standard deviation.

Focal plane amplitude at representative instants of time are shown in Fig. 3 for typical measured waveforms that have been focused without compensation, with time-shift compensation in the aperture, and with time-shift compensation following backpropagation along with the focus obtained with ideal data. The spread of the focus obtained from uncompensated waveforms is large relative to the spread of the focus obtained from ideal data. The focus of the waveforms that have been time-shift compensated is more concentrated than that obtained from uncompensated waveforms and further concentration is obtained in the focus of waveforms that have been time-shift compensated following backpropagation, but the focus of each is not as concentrated as the focus obtained from ideal waveforms.

Effective radius curves of the focus obtained from the same typical measured waveforms for uncompensated, time-shift compensated, backpropagated and time-shift compensated, and ideal cases are shown in Fig. 4. The effective radius of the focus obtained without compensation departs from the ideal case by 10% at a level -5.2 dB below the peak. Time-shift compensation in the aperture reduces the 10% deviation level to -21.4 dB while time-shift compensation following backpropagation has a 10% deviation level of -25.8 dB and has an effective radius that is appreciably narrower at levels 30 to 40 dB below the peak.

The focus obtained with each of the nine different sets of data as well as the improvement in focus obtained using time-shift compensation in the aperture and using time-shift compensation after backpropagation are described by the parameters in Table II. The data show that time-shift compensation in the aperture and time-shift compensation following backpropagation result in an effective radius at the focus that is similar at the -10- and -20-dB levels but that time-shift compensation following backpropagation improves the -30-dB effective radius substantially over that obtained with time-shift compensation in the receiving aperture. This indicates that time-shift compensation with or without backpropagation yields about the same point resolution but that time-shift compensation after backpropagation improves the contrast resolution more than time-shift compensation in the receiving aperture does. The -10-dB peripheral energy ratio obtained with time-shift compensation in the aperture averages about 25% of that without compensation while the -10-dB peripheral energy ratio obtained with time-shift compensation following backpropagation is about 16% of that obtained without compensation. These peripheral energy ratios are another indication that the sidelobe level, and therefore the contrast ratio, is improved more by backpropagation followed by time-shift compensation than by time-shift compensation alone.

The arrival time and energy level fluctuations produced

TABLE I. Breast tissue path statistics of wavefront distortion produced by nine different specimens.

Specimen number	Specimen thickness (mm)	Arrival time fluctuations			Energy level fluctuations			Waveform similarity factor
		rms value (ns)	99.5% value (ns)	Effective corr. len. (mm)	rms value (dB)	99.5% value (dB)	Effective corr. len. (mm)	
7	15-25	63.1	196.2	5.82	4.86	14.21	3.20	0.940
8a	30-35	66.5	222.0	4.88	6.08	16.35	4.85	0.926
8b	30	85.6	252.0	5.16	5.02	12.99	3.41	0.869
9a	40	76.5	225.7	4.81	5.65	15.10	4.25	0.914
9b	35	79.5	276.6	4.20	4.98	13.09	3.04	0.883
10	20-25	59.5	212.8	3.38	4.67	12.75	2.87	0.908
11	20-25	70.7	252.2	4.73	4.77	12.44	2.75	0.903
13	15-20	49.3	160.8	3.36	4.72	13.44	3.39	0.930
17	20-25	50.5	162.3	2.40	4.53	12.46	2.46	0.918
mean	26.9	66.8	217.8	4.30	5.03	13.65	3.36	0.910
s.d.	7.7	12.6	39.9	1.07	0.51	1.33	0.76	0.023

by different thicknesses of tissue for two specimens are shown in Fig. 5 and described statistically in Table III. The arrival time fluctuations, energy level fluctuations, and waveform distortion increase with specimen thickness for all but one measurement. The arrival time and energy level fluctuation patterns for the different thicknesses of the same specimen are seen to vary considerably. The focus characteristics associated with these patterns are given in Table IV.

The arrival time and energy level fluctuations in the aperture and after backpropagation are shown in Fig. 6 for two specimens for each of two source positions 12 mm apart. The features in the fluctuation patterns obtained for each specimen are recognizable but shifted in the patterns obtained after the change in source position. The features are also changed but still identifiable after backpropagation. The similarity of the patterns is indicated quantitatively by the distortion statistics given in Table V and by the focus characteristics presented in Table VI for compensation using the time shifts calculated from the waveforms produced with the source at the focal position. The data in Table VI also show that compensation using the time shifts calculated from waveforms produced with the source 12 mm from the focal position is less effective than compensation using the time shifts from waveforms produced with the source at the position of focus.

III. DISCUSSION

The specimens studied here were sections of breast tissue rather than whole breasts. They came from unusually large breasts and ranged from 15-40 mm in thickness with nearly planar surfaces. Thus while the measurements illustrate elements of distortion produced by the breast, they may not describe conditions typically encountered in the clinic. Nevertheless, the information obtained in this study under precisely controlled experimental conditions adds to the available data about the ultrasonic wavefront distortion produced by the breast and should be useful in the development of imaging instruments with better resolution for improved ultrasonic diagnosis of breast disease.

Refraction at the specimen-water interfaces could contribute to the distortion measured in this transmission study. Prior investigations^{16,17} have shown that this contribution is

negligible for abdominal wall, for which the surfaces are the skin and the peritoneum. The breast tissue specimens, however, had a cut surface on their lower side, so a special experiment was undertaken to investigate the contribution of refraction at this surface to the measured distortion. A thick specimen (BRS 9b) was selected and two measurements were made over approximately the same area, one with the skin side up and the other with the skin side down. Because of the 30-mm difference in propagation distance from the cut surface to the receiver in these measurements, differences in the distortion patterns from these measurements should be evident if refraction at the cut surface were an appreciable source of the distortion. In this experiment, however, the arrival time fluctuation rms values changed by less than 9% while the energy level fluctuation rms values and all correlation length values differed by less than 3%. These changes are within the range expected from reproducibility studies¹⁷ given the uncertainty in the scan position and the differences in propagation path caused by inverting the specimen. The arrival time and energy level fluctuation maps from the two measurements were also remarkably similar. Therefore, the cut specimen surface, which is smoothed by the kapton membrane during measurements, is not considered to contribute significantly to the distortion measured for the breast specimens.

The data processing used to determine the wavefront distortion in this study employed the same calculated fourth-order polynomial references for the determination of arrival and energy fluctuation as were described in the report¹⁷ of wavefront distortion by abdominal wall, but incorporated other improvements and extensions. The polynomial fits, as noted in Ref. 17, avoid the need for accurate knowledge about tissue dimensions and local acoustic characteristics and compensate for small misalignments and low spatial-frequency variations. The adaptive reference waveform method used to estimate arrival time differences in this paper is considered more accurate than the least-mean-square error method employed previously because, on average, fewer than 20% of the cross correlations computed for each abdominal wall data set using the adaptive reference waveform method had a peak value below 0.8, while about 30% of the

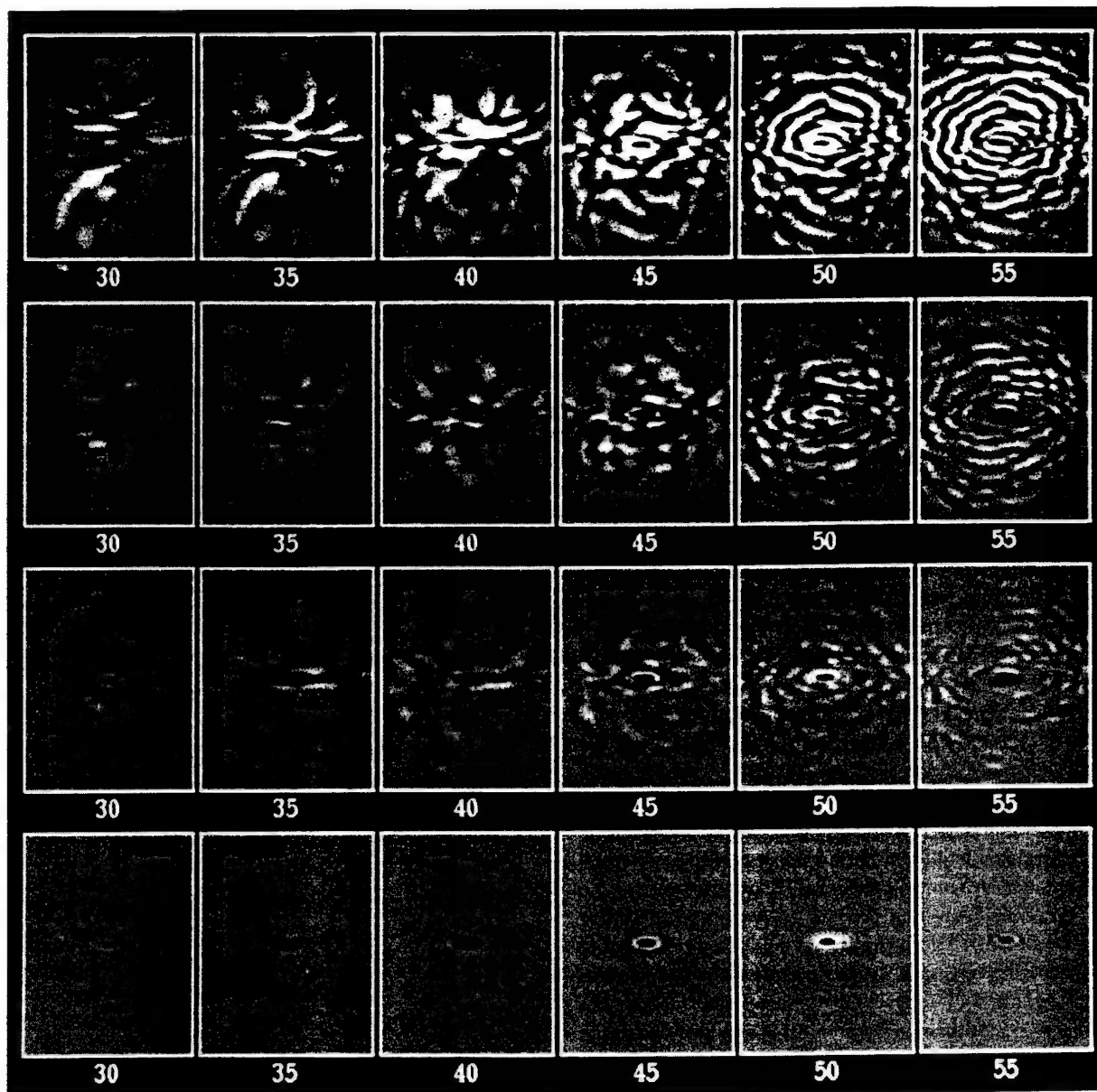


FIG. 3. Focal plane time histories of representative measured data (BRS 7). Each panel shows the bipolar distribution of signal amplitude as a shade of gray on a 50-dB log scale for each polarity in the focal plane at an instant of time. In all the panels, the horizontal coordinate is elevation and spans 37.504 mm while the vertical coordinate is in the array direction and spans 56.256 mm. The number beneath each panel identifies the (zero-origin) instant of time in the 128-point interval employed in the temporal Fourier transform. First row: Uncompensated data. Second row: After time-shift estimation and compensation in the aperture. Third row: After backpropagation of 40 mm followed by time-shift estimation and compensation. Fourth row: Ideal data.

peaks were below 0.8 for the least-mean-square error method. Also, the reference waveform method gives consistently lower estimates of distortion for water paths and yields superior focus characteristics when employed for time-shift compensation. Therefore, the reference waveform method was used in this study and the data in Ref. 16 were reprocessed using the reference waveform method to permit a comparison of the breast results discussed here with the abdominal wall data.

In the nine independent measurements reported here, an average (\pm s.d.) of 2807 (\pm 228) waveforms or 68.5% of the 4096 received waveforms were similar enough to be incorporated into the final reference waveform. The average of the maximum value for correlations between each of the win-

dowed waveforms and the final reference waveform was 0.868 (\pm 0.018). This figure, calculated using all of the waveforms in the aperture before any smoothing, is similar to the average cross-correlation value of 0.86 calculated for neighboring waveforms in the 35 data sets selected for analysis by Freiburger *et al.*⁵ in their two-dimensional study of the breast. An average of 758 (\pm 183) or 18.5% of the calculated delays were deemed unacceptable because they deviated significantly from the overall delay surface. Of these, 495 (about two thirds) were replaced by delays from new peak searches while the remaining 263 (about one third) were corrected by smoothing.

The representative waveforms in Fig. 1 illustrate the variability of the wavefronts from which the characteristics

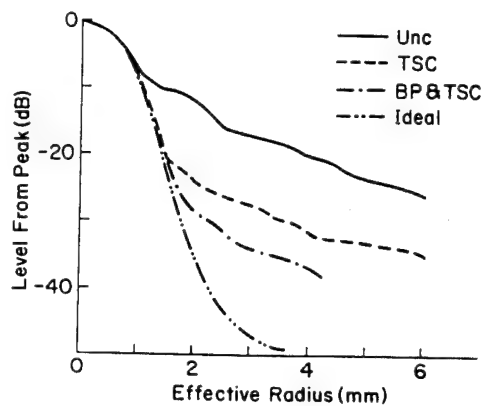


FIG. 4. Effective radius of the focus obtained with representative measured waveform data (BRS 7). Unc=uncompensated data. TSC=time-shift compensation in the receiving aperture. BP & TSC=backpropagation followed by time-shift compensation. Ideal=replication of a single average waveform throughout the receiving aperture.

of wavefront distortion have been found. The uniformity of the water path waveforms indicates that the error introduced by the apparatus is small compared to the fluctuations produced by the tissue path. The presence of tissue creates waveform shape changes which decorrelate the waveforms and introduce uncertainty in the estimation of arrival time. Improvement of arrival time estimation accuracy, and thus the correction of wavefront distortion, necessitates the removal of wave shape distortion and has motivated the introduction of a backpropagation step before time-shift compensation.

The arrival time and energy level fluctuation maps in Fig. 2 for the nine independent breast tissue measurements show the range of ultrasonic wavefront distortion patterns produced by human breast tissue in this study. These patterns have different characteristics from those reported¹⁷ for the abdominal wall. For example, the breast arrival time fluctuation maps contain smaller features than those in the abdominal wall arrival time plots. The backgrounds of the breast arrival time and energy level fluctuation maps are also comprised of larger, more irregular patches than those in the abdominal wall plots. However, as is the case with the abdominal wall patterns, some breast arrival time fluctuation

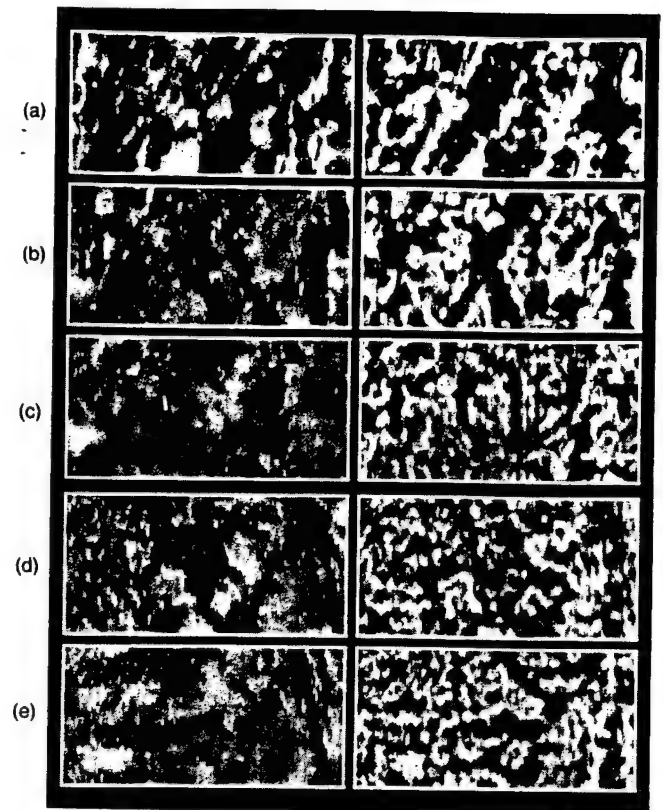


FIG. 5. Breast tissue path arrival time and energy level fluctuations for reductions of specimen thickness. (a)–(c) BRS 9a. (d) and (e) BRS 11. For each specimen, the results are presented from top to bottom in order of decreasing thickness. The format and scales in each pair of panels are the same as in Fig. 2.

map features appear to correlate with energy level fluctuations while others do not.

The bar charts in Fig. 7 compare the arrival time, energy level, and waveform distortion statistics for the nine breast specimen measurements to those in Ref. 17 for abdominal wall after recalculation using the reference waveform method. In general, breast tissue appears to cause more distortion than the abdominal wall. The rms arrival time fluctuations produced by the breast specimens in this study have

TABLE II. Breast tissue path focus characteristics for nine different specimens. r_e =effective radius. PER=peripheral energy ratio. Unc=uncompensated. TSC=time-shift compensation. BP=backpropagation followed by TSC. BP dist=distance of backpropagation for maximum waveform similarity.

Specimen number	BP dist. (mm)	-10 dB r_e			-20 dB r_e			-30 dB r_e			-10 dB PER			10% dev. lev.		
		Unc (mm)	TSC (mm)	BP (mm)	Unc (mm)	TSC (mm)	BP (mm)	Unc (mm)	TSC (mm)	BP (mm)	Unc	TSC	BP	Unc (dB)	TSC (dB)	BP (dB)
7	30	1.38	1.04	1.03	3.94	1.52	1.49	...	3.77	2.60	3.350	0.766	0.524	-5.2	-21.4	-25.8
8a	40	1.48	1.09	1.06	4.39	1.93	1.69	...	4.66	3.44	2.733	0.905	0.629	-1.0	-12.8	-17.0
8b	50	1.67	1.07	1.07	7.60	1.92	1.54	...	5.41	3.24	8.031	1.280	0.595	-0.9	-17.7	-22.0
9a	50	2.16	1.06	1.04	5.02	2.06	1.55	...	4.48	3.76	3.966	1.128	0.654	-4.9	-15.2	-20.9
9b	30	1.52	1.12	1.10	5.73	1.63	1.57	...	6.15	4.49	4.943	1.044	0.742	-1.0	-20.2	-23.7
10	40	1.17	1.04	1.03	3.39	1.59	1.50	...	3.64	2.54	3.957	0.968	0.592	-8.0	-19.4	-22.2
11	30	2.78	1.04	1.02	5.70	1.50	1.47	...	4.34	3.03	2.618	0.962	0.700	-3.4	-22.2	-24.4
13	30	1.16	1.05	1.03	2.71	1.54	1.48	5.92	3.74	2.89	1.766	0.712	0.554	-6.6	-20.1	-23.5
17	30	1.04	1.01	1.00	2.83	1.43	1.40	7.52	4.25	2.57	3.038	0.877	0.631	-13.3	-24.0	-26.1
mean		1.60	1.06	1.04	4.59	1.68	1.52	...	4.49	3.17	3.822	0.960	0.625	-4.9	-19.2	-22.8
s.d.		0.56	0.03	0.03	1.59	0.23	0.08	...	0.83	0.65	1.827	0.176	0.068	4.1	3.5	2.78

TABLE III. Breast tissue path statistics of wavefront distortion for reductions of specimen thickness.

Specimen number	Specimen thickness (mm)	Arrival time fluctuations			Energy level fluctuations			Waveform similarity factor
		rms value (ns)	99.5% value (ns)	Effective corr. len. (mm)	rms value (dB)	99.5% value (dB)	Effective corr. len. (mm)	
9a	40	76.5	225.7	4.81	5.65	15.10	4.25	0.914
	30	58.2	183.6	4.86	5.44	14.79	4.06	0.947
	18	54.6	157.6	5.12	5.01	15.31	2.92	0.965
11	20-25	70.7	252.2	4.73	4.77	12.44	2.75	0.903
	15	56.2	168.1	4.10	4.92	14.67	2.80	0.933

a mean of 66.8 ns, which is about 20% higher than the mean of 55.5 ns for the 14 abdominal wall samples. The rms energy level fluctuations produced by breast in this study have a mean value of 5.03 dB, which is about 39% higher than the mean of 3.62 dB for the abdominal wall. Wave shape distortion is also greater for the breast studies, which have a mean waveform similarity factor of 0.910 versus 0.938 for the abdominal wall.

The difference in the average thickness of breast and abdominal wall specimens may contribute to the difference in the average arrival time fluctuation rms values for the two types of specimens but appears to be a secondary source of the variation in energy level fluctuations. The mean thickness of the breast specimens is 25% larger than that of the abdominal walls and the average arrival time fluctuation of the breast specimens is about 20% larger than that of the abdominal walls. In addition, the arrival time fluctuation rms

values measured for specimens of both types having similar thicknesses were approximately the same. Thus the greater thickness of the breast specimens likely contributed importantly to the greater arrival time fluctuations observed in this study. However, a comparison of similarly thick breast and abdominal wall specimens revealed that the energy level fluctuation rms values of the breast specimens were larger in every case. This suggests that breast tissue produces more energy fluctuation per unit thickness than does abdominal wall tissue, so that the mean rms energy level fluctuation produced by the breast specimens would be greater than that of the abdominal walls even without the difference in their thicknesses.

The spatial distributions of arrival time and energy level fluctuations caused by breast and abdominal wall tissue differ as well. For the breast, the effective correlation length of arrival time fluctuation has a mean of 4.31 mm, which is

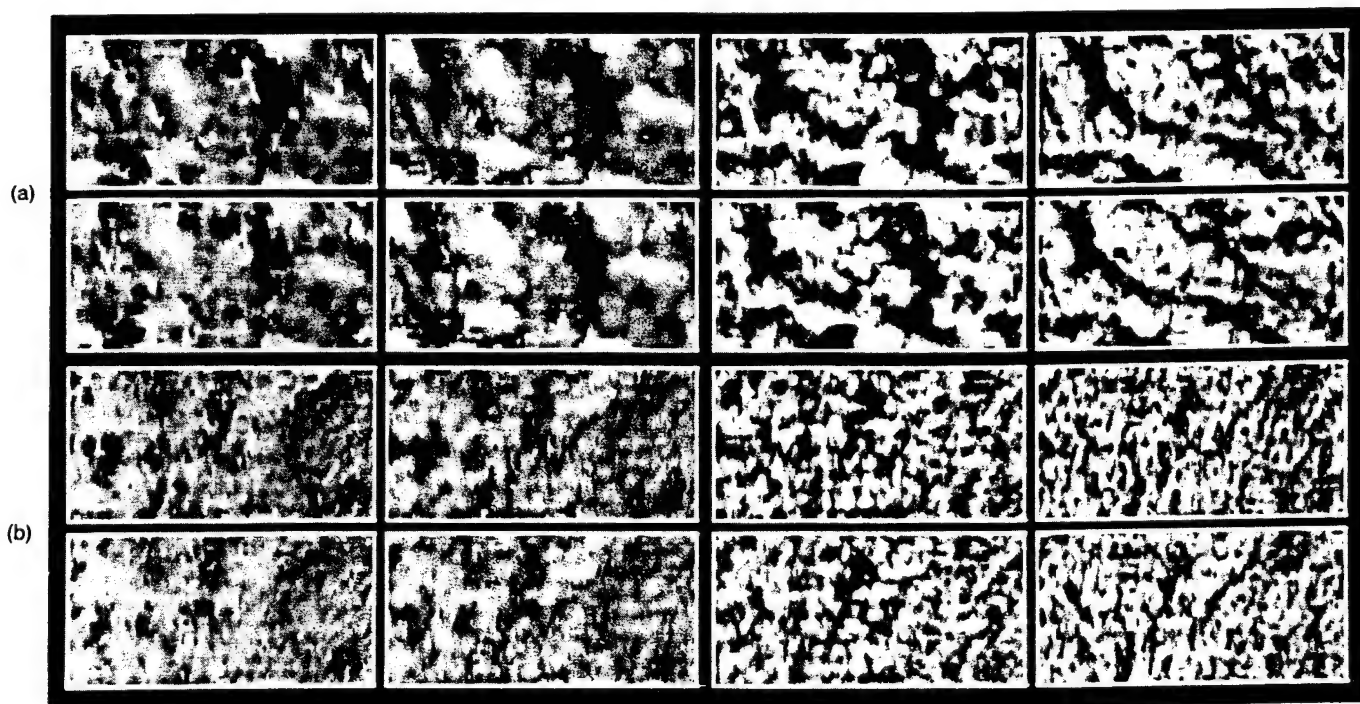


FIG. 6. Arrival time and energy level fluctuations before and after backpropagation for two source positions 12 mm apart. (a) BRS 8a. (b) BRS 17. For each specimen, the four-panel set on the left shows arrival time fluctuations and the four-panel set on the right shows the corresponding energy level fluctuations. In each four-panel set, the upper row shows the fluctuations with the source to the right and the lower row shows the fluctuations with the source to the left, while the left column shows the fluctuations in the measurement aperture and the right column shows the corresponding fluctuations after backpropagation to the distance of maximum waveform similarity. The scales in the panels are the same as in Fig. 2.

TABLE IV. Breast tissue path focus characteristics for reductions of specimen thickness. r_e =effective radius. PER=peripheral energy ratio. Unc=uncompensated. TSC=time-shift compensation. BP=backpropagation followed by TSC. BP Dist=distance of backpropagation for maximum waveform similarity.

Specimen number	BP dist. (mm)	-10 dB r_e			-20 dB r_e			-30 dB r_e			-10 dB PER			10% dev. lev.		
		Unc (mm)	TSC (mm)	BP (mm)	Unc (mm)	TSC (mm)	BP (mm)	Unc (mm)	TSC (mm)	BP (mm)	Unc	TSC	BP	Unc (dB)	TSC (dB)	BP (dB)
9a	50	2.16	1.06	1.04	5.02	1.06	1.55	...	4.48	3.76	3.966	1.128	0.654	-4.9	-15.2	-20.9
	40	1.14	1.04	1.03	3.66	1.73	1.56	7.20	3.82	2.89	2.372	0.830	0.540	-1.0	-17.0	-19.8
	20	1.56	1.03	1.03	4.10	1.49	1.46	8.06	4.21	2.94	2.954	0.673	0.508	-1.0	-22.1	-25.0
11	30	2.78	1.04	1.02	5.70	1.50	1.47	...	4.34	3.03	2.618	0.962	0.700	-3.4	-22.2	-24.4
	20	1.36	1.01	1.01	3.88	1.43	1.41	...	2.99	2.52	2.779	0.831	0.565	-5.6	-22.2	-24.2

26% smaller than the 5.78 mm mean calculated for the abdominal wall. The effective correlation length of energy level fluctuation for the breast has a mean of 3.36 mm, which is 45% larger than the abdominal wall correlation length of 2.31 mm. Consequently, the ratio of the average arrival time fluctuation effective correlation length to the average energy level fluctuation correlation length is 2.5 for the abdominal wall but only 1.3 for the breast specimens. This shows that the arrival time and energy level fluctuation correlation lengths for the breast are more similar to each other than are those for the abdominal wall.

The focus obtained with uncompensated breast tissue waveforms was predictably worse than that obtained with abdominal wall waveforms as is illustrated by the bar charts in Fig. 8 for uncompensated data. For example, the mean -10-dB peripheral energy ratio of the focused breast data was 3.8, nearly twice the average value of 2.1 computed for the abdominal data. Also, although not shown in Fig. 8, the mean -20-dB effective radius for the focused breast data was 4.6 mm while the corresponding value was 3.6 mm for the abdominal wall data. However, both the average breast and abdominal wall data sets first deviate 10% from their ideal effective radius curves at about -5 dB.

Time-shift compensation after backpropagation improves the focus of breast data more than time-shift compensation in the aperture does. However, in neither case is the average focus better than that of abdominal wall data after similar processing. The bar charts in Fig. 8 illustrate these trends. For example, the average 10% deviation level for breast data is reduced to -18.4 dB by time-shift compensation in the aperture and to -22.3 dB by time-shift compensation after backpropagation, but the corresponding values for the abdominal wall data are -23.5 and -26.3 dB, respectively. Similarly, time-shift compensation in the aperture reduces the average -10-dB peripheral energy ratio to 1.0

for the breast measurements and time-shift compensation after backpropagation further reduces it to 0.60, while the corresponding values for the abdominal wall measurements are 0.63 and 0.47. Although both compensation techniques improve the focus of ultrasonic waveforms that have propagated through breast tissue, time-shift compensation is more effective when performed after backpropagation.

The distance of backpropagation for maximum waveform similarity, i.e., the position of the equivalent phase screen in the propagation model employed here, is indicated by the data in Tables I and II (as well as in Tables III-VI) to be usually greater than the specimen thickness. However, as already noted, a distance of about 8 mm is present between the top surface of the specimen and the receiving aperture in the measurements. Adding 8 mm to the mean (\pm s.d.) specimen thickness given in Table II yields 34.9 (\pm 7.7) mm while the mean backpropagation distance is 36.7 (\pm 8.7) mm. Thus the data indicate that the optimum backpropagation distance is approximately the sum of the specimen thickness and the specimen-receiver separation, as in the case of the abdominal wall measurements.¹⁶ The physical origin of this circumstance is currently unknown, although observations and experiments noted earlier indicate that the origin is not refraction at the specimen boundary. Additional studies are needed to provide information about the relation between tissue morphology and ultrasonic aberration.

The plots of arrival time and energy level fluctuations in Fig. 5 and the statistics of Table III show that reducing the tissue path length decreases the severity of the distortion produced in transmitted ultrasonic pulses. For both specimens 9a and 11, the magnitude of the measured arrival time and energy level fluctuations decreases as the tissue thickness is reduced while waveform similarity generally increases. The lack of similarity in the patterns of fluctuations as each specimen decreases in thickness is attributed to configurational

TABLE V. Breast tissue path statistics of wavefront distortion for two source positions 12 mm apart.

Specimen number	Source position	Arrival time fluctuations			Energy level fluctuations			Effective corr. len. (mm)	Waveform similarity factor
		Specimen thickness (mm)	rms value (ns)	99.5% value (ns)	Effective corr. len. (mm)	rms value (dB)	99.5% value (dB)		
8a	Left	30-35	66.5	222.0	4.88	6.08	16.35	4.85	0.926
	Right	30-35	65.2	216.0	4.17	6.01	15.11	4.79	0.916
17	Left	20-25	50.5	162.3	2.40	4.53	12.46	2.46	0.918
	Right	20-25	47.0	150.4	2.27	4.36	11.93	2.44	0.909

TABLE VI. Breast tissue path focus characteristics for two source positions. The numbers in parentheses are values obtained at one source position with waveforms compensated using time-shifts calculated with waveforms from the other source position. r_e =effective radius. PER=peripheral energy ratio. Unc=uncompensated. TSC=time-shift compensation. BP=backpropagation followed by TSC. BP Dist=distance of backpropagation for maximum waveform similarity.

Specimen number	Source position	BP dist. (mm)	-10 dB r_e			-20 dB r_e			-30 dB r_e			-10 dB PER			10% dev. lev.		
			Unc (mm)	TSC (mm)	BP (mm)	Unc (mm)	TSC (mm)	BP (mm)	Unc (mm)	TSC (mm)	BP (mm)	Unc	TSC	BP	Unc (dB)	TSC (dB)	BP (dB)
8a	Left	40	1.48	1.09 (1.13)	1.06 (1.12)	4.39	1.93 (2.41)	1.69 (2.17)	...	4.66 (6.76)	3.44 (6.24)	2.73	0.91 (1.75)	0.63 (1.35)	-1.0	-12.8 (-7.7)	-17.0 (-8.8)
	Right	40	1.43	1.05 (1.09)	1.05 (1.09)	4.61	1.82 (2.47)	1.55 (1.87)	...	4.86 (7.20)	3.74 (6.23)	3.17	1.05 (1.91)	0.67 (1.34)	-1.0	-16.4 (-11.5)	-20.6 (-12.0)
17	Left	30	1.04	1.01 (0.99)	1.00 (1.00)	2.83	1.43 (1.76)	1.40 (1.67)	7.52	4.25 (6.98)	2.57 (5.46)	3.04	0.88 (2.29)	0.63 (1.75)	-13.3	-24.0 (-17.7)	-26.1 (-19.1)
	Right	30	1.06	1.02 (1.01)	1.01 (1.02)	2.86	1.53 (1.75)	1.46 (1.64)	7.07	4.67 (...)	2.31 (5.92)	2.79	0.88 (2.32)	0.63 (1.78)	-12.3	-22.2 (-16.9)	-28.1 (-18.4)

changes that result from removal of tissue slabs, differences in position of the specimen, and deformation from pressure applied when the specimen was sliced.

The nine separate breast measurements show a similar dependence of distortion on specimen thickness. Linear regression establishes significant relationships between breast tissue thickness and both rms arrival time and energy level fluctuation values, with correlation coefficients of 0.729 and 0.724, respectively. The energy level fluctuation correlation lengths are somewhat correlated to thickness as well. For the abdominal wall specimens, the arrival time fluctuation rms and correlation length values are moderately correlated to thickness and the waveform similarity factor is closely correlated, but energy fluctuation rms values and correlation lengths are not correlated to thickness. Since breast tissue consists of a heterogeneous arrangement of fat, glandular, and connective tissue while the abdominal wall is comprised of distinct fat and muscle layers, morphological differences are thought to be the reason for the observed differences in fluctuations produced by breast and abdominal wall.

The arrival time fluctuation maps in Fig. 6 and focus parameters in Table VI for measured wavefronts with different source positions demonstrate that the time shifts that best compensate the focus at one position may be less effective when the desired focus is moved 12 mm laterally and indicate that the use of backpropagation reduces this problem. Compensation in the aperture using the time-shifts calculated for the adjacent source position, i.e., cross compensation, improves the focus in every case, but is far less effective than compensation using the time-shifts calculated for the data set being corrected. Backpropagation increases the peak cross-correlation coefficient of the arrival time fluctuation map pairs to 0.728 from 0.564 for specimen 8a and to 0.568 from 0.426 for specimen 17. Cross compensation is more effective after backpropagation, but still does not achieve the level of focus improvement obtained using regular time-shift compensation in the aperture. This implies a limitation on the size of the region over which a single pattern of compensation is useful. For a related theoretical treatment that yields an expression for the size of the isoplanatic patch, see Ref. 19.

The statistics of the arrival time distortion measured in this study can be compared to the *in vivo* results of Freiburger *et al.* for a two-dimensional array.⁵ Their mean rms phase distortion value of 55.3 ± 14.0 ns obtained for 35 scans on the left breasts of seven volunteers is somewhat lower than the 66.8 ± 12.6 ns determined here for nine breast specimens. However, their tissue paths had a mean length of 78.8 ± 21.4 mm,²⁰ which is much longer than those measured here. As discussed above, a longer path is expected to produce larger fluctuations in arrival time. Also, their receiver elements were 0.51×3.50 mm², which corresponds to a surface area 1.7 times larger than that of the elements used in this study. A larger measurement spot is associated with a decrease in measured arrival time fluctuations because the fluctuations are averaged over the measurement spot, as detailed in a study²¹ that emulated the outputs of elements of various sizes in one-dimensional apertures from the measured outputs of smaller elements in a two-dimensional aperture. Nevertheless, the 4.31 ± 1.08 -mm phase correlation length measured here is similar to the 4.21 ± 1.14 -mm value obtained by Freiburger *et al.*⁵ in the azimuthal direction. The effects of the distortion measured in the two cases on the resulting focus are not comparable because of substantial differences in focusing parameters.

The wavefront distortion and focus degradation found in this study may also be compared with the already cited *in vivo* results of Zhu and Steinberg.⁶⁻⁹ Their observation of severe amplitude distortion accompanying phase distortion in narrow-band measurements is analogous to energy level fluctuations accompanying arrival time fluctuations in the present wideband measurements. The emphasis that Zhu and Steinberg give to the influence of amplitude distortion in their analysis is strongly supported by the new data given here. Zhu and Steinberg also showed representative reconstructions of source profiles that are analogous in the present study to effective width curves of the uncompensated focus in the array direction. The high degradation of the source profiles illustrated in their reports is qualitatively similar to the poor focus characteristics given here for uncompensated data. However, a quantitative comparison of source profile and focus width characteristics is not readily made with the

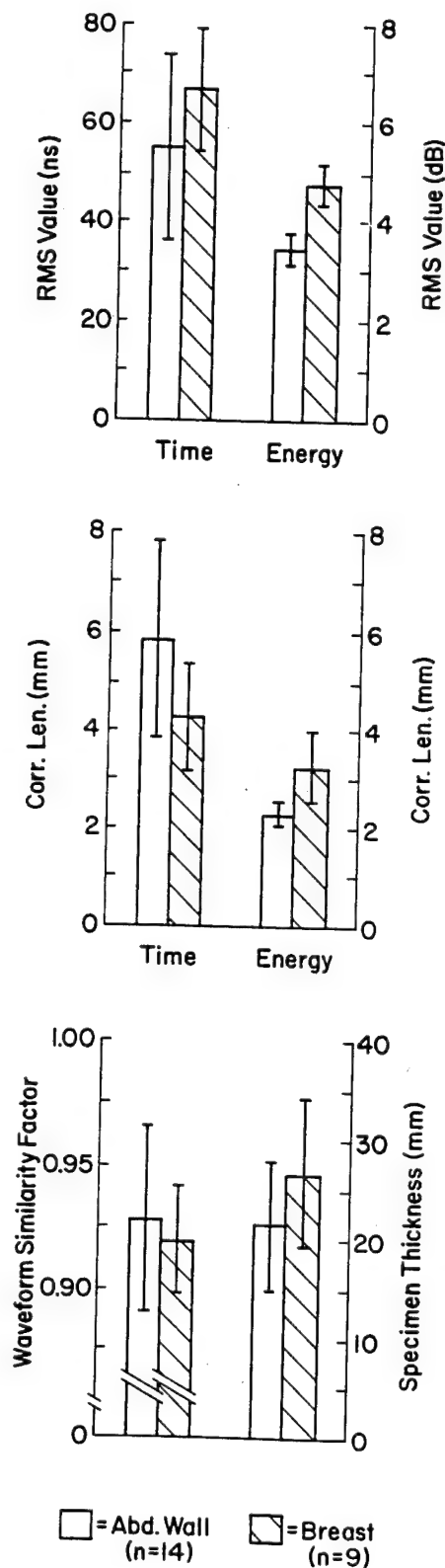


FIG. 7. Comparison of breast and abdominal wall wavefront distortion statistics. In each chart, the average and standard deviation of the measurements within each group are shown.

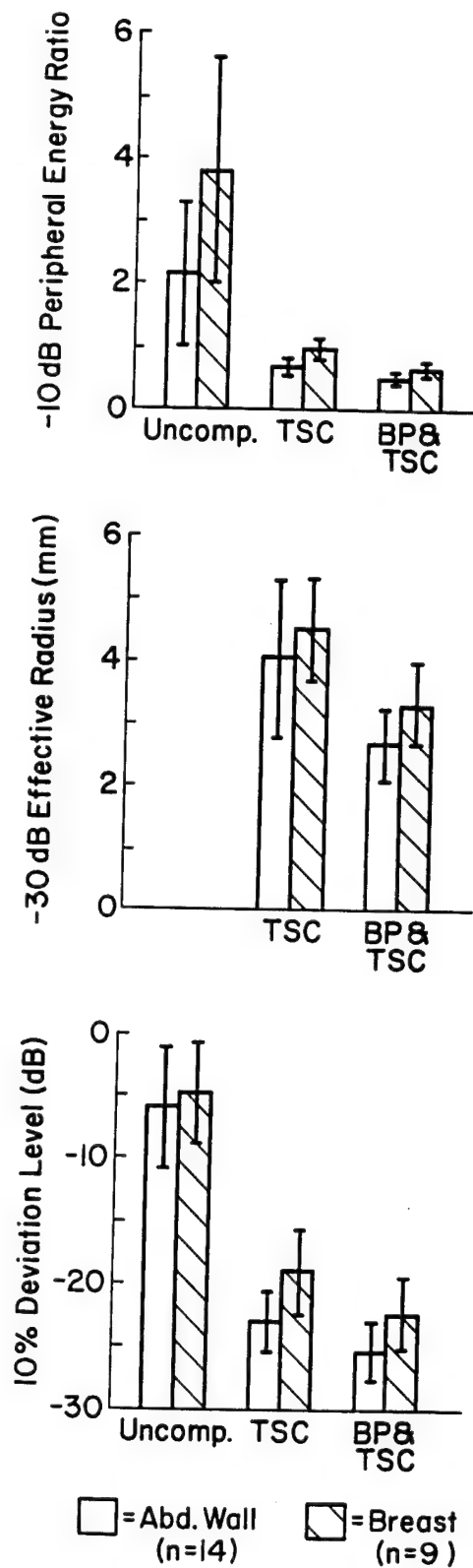


FIG. 8. Comparison of breast and abdominal wall focus statistics. In each chart, the average and standard deviation of the measurements within each group are shown. Uncomp=uncompensated waveforms. TSC=time-shift compensation. BP&TSC=backpropagation before time-shift compensation.

published Zhu and Steinberg data because they employed different focus descriptors, as well as relatively narrow-band pulses, a larger measurement spot size, and significantly longer tissue paths.

IV. CONCLUSION

Ultrasonic wavefront distortion produced by transmission through breast specimens has been investigated by recording and processing pulsed waveforms to obtain maps and statistics of arrival time and energy level fluctuations. The average rms value of the arrival time fluctuations was similar to that for abdominal wall specimens of like thickness while the average rms value of energy level fluctuations was greater than that for similarly thick abdominal wall specimens. The average effective correlation length of the arrival time fluctuations for breast specimens was shorter than that for the abdominal wall while the average effective correlation length of the energy level fluctuations was larger than that for the abdominal wall. The breast tissue waveforms showed more variation than the abdominal wall waveforms. Time-shift compensation in the aperture improved the focus of pulses distorted by breast tissue specimens and time-shift compensation after backpropagation brought the focus closer to the ideal, but the improvement was generally less than that obtained for distortion produced by abdominal wall. Repeated study of specimens with reduction of thickness showed that pulse arrival times, energy levels, and wave shape are increasingly altered as tissue path length increases. Measurements using different source positions indicated that time-shift compensation in the aperture with arrival times estimated when the source was 12 mm away from the focal position produced little improvement in the focus, but that backpropagation made such cross compensation more effective, although still less effective than self-compensation in the receiving aperture. These results demonstrate that ultrasonic propagation through breast tissue produces appreciable arrival time and energy level fluctuations and provide important new information about the variety and range of these fluctuations. They also show that time-shift compensation improves the focus of waveforms distorted by breast tissue, especially when the compensation is applied after wavefront backpropagation.

ACKNOWLEDGMENTS

The authors thank Dr. Elethea Caldwell, Dr. Leon Metlay, and Mick Kazee for their assistance in obtaining and characterizing breast tissue specimens from surgery. Cooperation and assistance from the staff of the Diagnostic Ultrasound Department at the University of Rochester's Strong Memorial Hospital is acknowledged with appreciation as are many useful discussions with Dr. T. Douglas Mast. Funding for this investigation was provided by the University of Rochester Diagnostic Ultrasound Research Laboratory Industrial Associates, NIH grants DK 45533 and HL 50855,

NSF grant BCS92-09680, and U.S. Army Medical Research & Development Command grants DAMD 17-93-J-3014 and DAMD 17-94-J-4384. Computations were performed at the Cornell National Supercomputing Facility, which is supported in part by the National Science Foundation, New York State, and the IBM Corporation.

- ¹ P. M. Jokich, D. L. Monticciolo, and Y. T. Adler, "Breast Ultrasonography," *Radiol. Clin. North Am.* **30**(5), 993-1009 (1992).
- ² W. J. Donegan, "Evaluation of a Palpable Breast Mass," *N. Engl. J. Med.* **327**(13), 937-942 (1992).
- ³ M. Moshfeghi and R. C. Waag, "In-Vivo and In-Vitro Ultrasound Beam Distortion Measurements of a Large Aperture and a Conventional Aperture Focussed Transducer," *Ultrasound Med. Biol.* **14**(5), 417-430 (1988).
- ⁴ G. E. Trahey, P. D. Freiburger, L. F. Nock, and D. C. Sullivan, "In Vivo Measurements of Ultrasonic Beam Distortion in the Breast," *Ultrason. Imag.* **13**(1), 71-90 (1991).
- ⁵ P. D. Freiburger, D. C. Sullivan, B. H. LeBlanc, S. W. Smith, and G. E. Trahey, "Two Dimensional Ultrasonic Beam Distortion in the Breast: In Vivo Measurements and Effects," *Ultrason. Imag.* **14**(4), 398-414 (1992).
- ⁶ Q. Zhu and B. D. Steinberg, "Large-Transducer Measurements of Wavefront Distortion in the Female Breast," *Ultrason. Imag.* **14**(3), 276-299 (1992).
- ⁷ Q. Zhu and B. D. Steinberg, "Wavefront Amplitude Distribution in the Female Breast," *J. Acoust. Soc. Am.* **96**, 1-9 (1994).
- ⁸ Q. Zhu and B. D. Steinberg, "Wavefront Amplitude Distortion and Image Sidelobe Levels—Part I: Theory and Computer Simulations," *IEEE Trans. Ultrason. Ferroelect. Freq. Control* **40**(6), 747-753 (1993).
- ⁹ Q. Zhu, B. D. Steinberg, and Ronald Arenson, "Wavefront Amplitude Distortion and Image Sidelobe Levels—Part II: In Vivo Experiments," *IEEE Trans. Ultrason. Ferroelect. Freq. Control* **40**(6), 754-762 (1993).
- ¹⁰ S. W. Flax and M. O'Donnell, "Phase-Aberration Correction Using Signals from Point Reflectors and Diffuse Scatterers: Basic Principles," *IEEE Trans. Ultrason. Ferroelect. Freq. Control* **35**(6), 758-767 (1988).
- ¹¹ M. O'Donnell and S. W. Flax, "Phase-Aberration Correction Using Signals from Point Reflectors and Diffuse Scatterers: Measurements," *IEEE Trans. Ultrason. Ferroelect. Freq. Control* **35**(6), 768-774 (1988).
- ¹² L. Nock, G. E. Trahey, and S. W. Smith, "Phase Aberration Correction in Medical Ultrasound Using Speckle Brightness as a Quality Factor," *J. Acoust. Soc. Am.* **85**, 1819-1833 (1989).
- ¹³ D. Zhao and G. E. Trahey, "A Statistical Analysis of Phase Aberration Correction Using Image Quality Factors in Coherent Imaging Systems," *IEEE Trans. Med. Imag.* **11**(3), 446-452 (1992).
- ¹⁴ M. Fink, "Time Reversal of Ultrasonic Fields—Part I: Basic Principles," *IEEE Trans. Ultrason. Ferroelect. Freq. Control* **39**(5), 555-566 (1992).
- ¹⁵ F. W. Wu, J.-L. Thomas, and M. Fink, "Time Reversal of Ultrasonic Fields—Part II: Experimental Results," *IEEE Trans. Ultrason. Ferroelect. Freq. Control* **39**(5), 567-578 (1992).
- ¹⁶ D.-L. Liu and R. C. Waag, "Correction of Ultrasonic Wavefront Distortion Using Backpropagation and a Reference Waveform Method for Time-Shift Compensation," *J. Acoust. Soc. Am.* **96**, 649-660 (1994).
- ¹⁷ L. M. Hinkelman, D.-L. Liu, L. A. Metlay, and R. C. Waag, "Measurements of Ultrasonic Pulse Arrival Time and Energy Level Variations Produced by Propagation through Abdominal Wall," *J. Acoust. Soc. Am.* **95**, 530-541 (1994).
- ¹⁸ D.-L. Liu and R. C. Waag, "Time-Shift Compensation of Ultrasonic Pulse Focus Degradation Using Least-Mean-Square Error Estimates of Arrival Time," *J. Acoust. Soc. Am.* **95**, 542-555 (1994).
- ¹⁹ B. D. Steinberg and A. K. Luthra, "Simple Theory of the Effects of Medium Turbulence upon Scanning with an Adaptive Phased Array," *J. Acoust. Soc. Am.* **71**, 630-634 (1982).
- ²⁰ P. D. Freiburger (personal communication, 20 April 1994).
- ²¹ D.-L. Liu and R. C. Waag, "A Comparison of Wavefront Distortion and Compensation in One-Dimensional and Two-Dimensional Apertures," *IEEE Trans. Ultrason. Ferroelect. Freq. Control* (in press).

Correlation distance measurements of the female breast

Qing Zhu and Bernard D. Steinberg

Valley Forge Research Center, The Moore School of Electrical Engineering, University of Pennsylvania,
Philadelphia, Pennsylvania 19104

Ronald Arenson^{a)}

Department of Radiology, Hospital of the University of Pennsylvania, Philadelphia, Pennsylvania 19104

(Received 10 December 1992; revised 29 November 1994; accepted 21 March 1995)

Ultrasonic waves propagating through soft tissue experience wavefront distortion. Adaptive wavefront compensation algorithms attempt to correct such distortion. A valuable design parameter is the isoplanatic patch size of the imaging medium. Its lateral extent is the FWHM of the correlation function. The range extent is defined similarly. The significance of the isoplanatic patch is that a new wavefront correction vector must be obtained whenever the ultrasound beam is moved a patch length. This paper reports measurements of wavefront correlation functions as well as statistics of the lateral correlation distance ρ_d (half the FWHM) within the female breast obtained from a population of 22 women (44 breasts) and measured at 3 and 4 MHz with a large acoustic aperture (9.6 cm). A set of complex wavefronts radiated from single pointlike sources was measured from the opposing side of the breast. The propagation distance was 12 cm. ρ_d is the distance between two sources at which the correlation between their wavefronts drops to 0.5. The mean value at 3 MHz was found to be less than 1.5 mm for the premenopausal dense breast, 2.5 mm for the premenopausal fatty breast, and 2.0 mm for the postmenopausal breast. The mean value dropped by a factor of 2 at 4 MHz for a group consisting of premenopausal fatty and postmenopausal breasts. © 1995 Acoustical Society of America.

PACS numbers: 43.80.Cs, 43.80.Ev, 43.80.Vj

INTRODUCTION

Commercial ultrasound instruments assume constant sound speed, typically 1540 m s^{-1} in soft tissue, throughout the field of view. Delays to steer and focus the ultrasonic beam and to convert the round trip echo time into range assume fixed speed. However, the constant speed assumption is violated when the refractive index varies with position in the imaging tissue. The main phenomena experienced are refraction, diffraction, and weak scattering. All three induce wavefront distortion; the first two affect the wavefront primarily by coherent interference and the latter by perturbing the phasefront of the propagating wave. Diffraction-limited imaging, in which the lateral resolution at the focal distance is $\lambda R/L$ (wavelength times focal distance divided by aperture size), becomes difficult (or impossible) when wavefronts are distorted and the imaging aperture exceeds the scale of the distortion.

Several investigators have studied the effects of breast tissue inhomogeneities upon focusing of ultrasonic beams when aperture size is increased. Foster and Hunt¹ measured one-way beam patterns *in vitro* of propagating waves in the focal zones of different f -number lenses and found general improvement in focusing with f number down to about $f/3$ in several breast samples. Moshfeghi and Waag² measured two-way beam patterns *in vivo* and *in vitro* by using $f/2.6$ and $f/1.0$ apertures and reported that resolution improvement with increasing aperture size was only $2/3$ of that found

without distortion. In the *in vivo* experiment with the compressed breast, they found unusually high sidelobes (greater than -10 dB). Our work with *in vivo* wavefront measurements of the female breast with a large phased array (5–9.6 cm) over a 12-cm propagation path shows that focusing through a large breast is difficult to achieve.³ Refraction and strong scattering appear to be significant contributors to the focusing degradation.⁴

In vivo time-of-flight measurements have been reported in Refs. 5–7. Trahey *et al.*⁵ measured arrival time profiles of the female breast by using a 1.4-cm phased array and reported $2.1 (\pm 0.74) \text{ mm}$ average FWHM of correlation curves of arrival time profiles (after removal of the linear component). The same group later extended their measurement to two dimensions⁶ with a 1.4- by 1.6-cm array and reported 4.21-mm average FWHM (after removal of the planar component) in azimuth; the elevation measurement was not reported. Durbin *et al.*⁷ reported 0.98 correlation between breast time-of-flight profiles measured with a 2-cm, 1-D array in which the sources were spaced by 3 mm. The average correlation of point spread functions after maximum amplitude projection along the time axis from the same sources was 0.66. Recently, Hinkelman *et al.*⁸ measured correlation curves of breast-sample arrival time profiles with a 2-D array 46 by 92 mm and reported $4.3 (\pm 1.1) \text{ mm}$ average FWHM.

These data suggest that wavefront distortion can cause significant focusing degradation especially when the imaging aperture becomes large and the frequency becomes high. Adaptive wavefront compensation algorithms, developed in several fields,^{9–18} have the potential to improve focusing (and therefore image quality) in the breast by self-cohering

^{a)}Currently with the Department of Radiology, University of California, San Francisco, CA 94143.

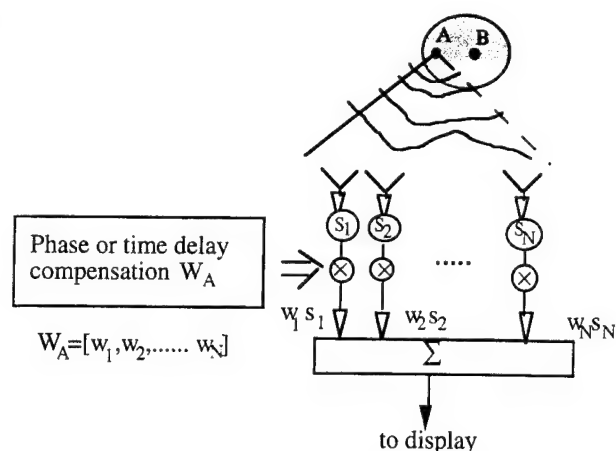


FIG. 1. Weight vector W_A compensates for phase distortion from A but not from B.

the distorted phasefront or wavefront. These algorithms create compensation weight vectors to compensate for the distortion by (1) capturing the time-delay or phasefront distortion information from cross-correlation measurements of the wavefront^{9,11-16} (the image brightness algorithm^{9,15} is equivalent to the cross-correlation algorithm^{13,14} when phase error or arrival time fluctuation is estimated not only by cross-correlating adjacent elements but also by cross-correlating certain distant elements¹⁹), (2) capturing the wavefront distortion information by conjugating the received wavefront in a narrow frequency band¹⁰ or at every frequency component within the signal band,¹⁷ and (3) back-propagating the received wavefront to the position where procedure (1) is most effective.¹⁸

Focusing studies through *in vivo* breast after applying phase deaberration algorithms^{10,13-15} has been conducted by several groups.^{5,6,8,20} The procedure consists of (1) measuring the wavefront at the receiving array due to a point source or a single transducer element, (2) calculating the weight vector by cross-correlating adjacent received waveforms or by conjugating the received wavefront, and (3) time-delay or phase compensating at each element to form a focused, retrodirective beam on the source. The question to be asked is over how large an area (2-D case) or volume (3-D case) can this adaptively formed beam be scanned to form a good image? Figure 1 illustrates the pertinent issue in the 2-D case. Source or target A radiates or reradiates to the receiving array. A weight vector w_A is adaptively created from the radiation field received from A so as to focus the array on source A. Source (or target) B located in the neighborhood of A radiates or reradiates to the same receiving array. The wavefront from B is not shown in Fig. 1. A weight vector w_B is created similarly. The similarity or correlation between w_A and w_B , defined as the Hermitian inner product $w_A w_B^H$, determines whether w_A can be used to form a good image of B. Define the isoplanatic patch as the area over which a single aperture weight vector will form a good image. This area will depend on the geometry of the aberrators of the imaging medium. Acoustically inhomogeneous tissue has a smaller isoplanatic patch than homogeneous tissue. A small isoplanatic patch, as implied by the small wavefront

correlation-distance measurements of a few mm reported in this paper, for large breasts and large apertures, poses a severe problem in system design. It implies that a single wavefront correction will not suffice over a large area. Instead the system will have to compute or update a new weight vector for every isoplanatic patch and will have to coherently combine the subimages from them to form a final image.

This paper provides correlation information of complex wavefront propagated 12 cm through female breasts of 22 women (44 breasts) and measured with a large aperture (9.6 cm). Complex wavefronts were radiated from a sequence of single pointlike sources introduced at one side of the breast. It is shown that the correlation of complex wavefronts is mathematically equal to that of complex images of the same sequence of single sources. Without medium-induced distortion the correlation function is close to unity for approximately 6 mm. This is demonstrated by measurements made in an oil bath without tissue. With medium-induced distortion, the wavefront (and therefore the image) changes when obtained from a slightly different portion of the breast and correlation drops in a few mm. A common measure of the decorrelation is the correlation distance ρ_d , defined as the distance between two sources at which their wavefront correlation drops to 0.5. Thus ρ_d is half the FWHM of the correlation function. It is an indicator of how often the weight vector has to be changed in azimuth to compensate for the distortion.

This paper is organized as follows: Section I defines and derives the correlation of the complex wavefront and its complex image correlation equivalent. Section II describes the *in vivo* experimental method used to measure the wavefronts from a sequence of single sources radiating through the female breast. Section III reports experimental ρ_d result for 22 women (44 breasts). The population was divided into three nearly equal groups based upon mammographic observations. They are premenopausal dense, premenopausal fatty, and postmenopausal. Measurement quality is discussed in Sec. IV. A comparison of the correlation result reported in this paper with other groups' results is in Sec. V. The significance of correlation distance is discussed in Sec. VI. The summary is in Sec. VII.

I. BASIC PRINCIPLE

The following derivations are valid for cw and can be used as an approximation for the wideband case.

A. Complex radiation field and image

Let $s(u)$ represent the complex angular source distribution in one dimension, where $u = \sin(\theta)$ and θ is the angle from the array normal. Its complex radiation field on the axis of the receiving array, when the medium is homogeneous, after correcting for near-field curvature, is the inverse Fourier transform of $s(u)$

$$v(x) = F^{-1}(s(u)) = \int s(u) \exp\left(-j \frac{2\pi}{\lambda} xu\right) du, \quad (1)$$

where λ is the wavelength and x represents position in the array. The measured field at the finite receiving aperture is

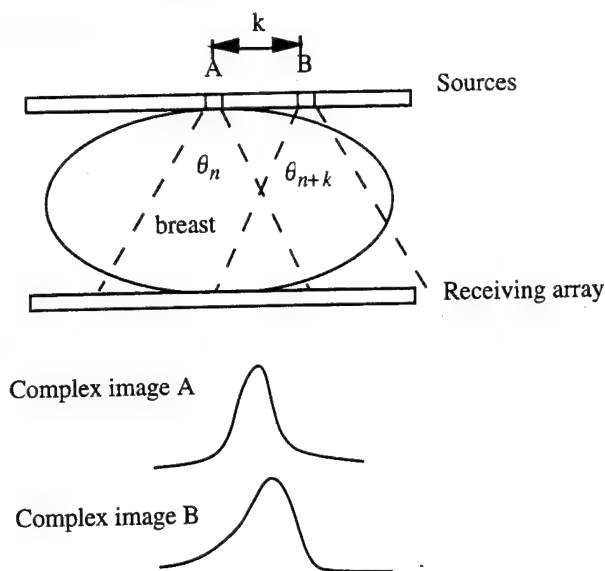


FIG. 2. Illustration of wavefront correlation. Source A is at position n in the transmitting array. Source B is at $n+k$. Wavefronts from each are measured in the receiving array, and images are calculated. Because the focusing vector is separately applied to each source, the optical axis of each image is the same.

$$i(x) = w(x)v(x), \quad (2)$$

where $w(x)$ is the receiving aperture weighting function.

When the medium is inhomogeneous, the measured radiation field at the receiving array, after correcting for near-field curvature, is

$$i(x) = \alpha w(x)v(x)m_\theta(x), \quad (3)$$

where $m_\theta(x) = a_\theta(x)e^{j\beta_\theta(x)}$ is the complex medium-induced distortion with amplitude $a_\theta(x)$ and phase $\beta_\theta(x)$. Subscript θ indicates an expected angular sensitivity of $m(x)$ because waves arriving from different directions pass through different portions of the medium and therefore experience different wavefront perturbations. α is a constant that accounts for signal loss. In general, it is also a function of θ . The complex image is

$$\hat{s}(u) = \alpha F[w(x)v(x)m_\theta(x)] = \alpha f(u)*s(u)*F[m_\theta(x)], \quad (4)$$

where $F[m_\theta(x)] \triangleq \mu_\theta(u)$ is the angular impulse response of the medium. Equation (4) is a general expression; it includes the homogeneous case for which $\mu_\theta(u) = \delta(u)$ and $\alpha=1$.

B. Correlation function (cf) of a complex radiation field

The cf of the complex radiation field is calculated from a set of radiation fields measured through the distorting medium. Figure 2 sketches the geometry. Source A located in the focal zone of the receiving array radiates ultrasonic waves through the medium and the received complex field is, from (4), $i_n(x) = \alpha_n w(x)v(x)m_{\theta_n}(x)$, where n is the position index of source A. θ_n is the angular sector that the waves from A encounter. α_n is a constant that accounts for energy loss. Next, waves radiating from source B encounter

angular sector θ_{n+k} , which may have a portion in common with θ_n , where $n+k$ is the position index of source B. The k th correlation is defined as

$$\begin{aligned} & \int i_n(x)i_{n+k}^*(x)dx \\ &= \alpha_n \alpha_{n+k} \int |w(x)|^2 |v(x)|^2 m_{\theta_n}(x)m_{\theta_{n+k}}^*(x)dx. \end{aligned} \quad (5)$$

The superscript $*$ denotes complex conjugate.

In a homogeneous medium $\int i_n(x)i_{n+k}^*(x)dx = \int |i(x)|^2 dx = \text{constant}$ for all n and k . In an inhomogeneous medium, $\int i_n(x)i_{n+k}^*(x)dx$ attains its maximum when $\alpha_n = \alpha_{n+k}$ and $m_{\theta_n}(x) = m_{\theta_{n+k}}(x)$ (Schwartz inequality). Thus $\int i_n(x)i_{n+k}^*(x)dx$ measures the similarity between two complex fields radiated from two sources spaced by k and consequently reflects the extent of the tissue homogeneity within the joint angular sector. To obtain the cf we average this quantity over all measurements at fixed k and normalize to unity at the origin. Because the measurements are made at discrete locations the continuous variable x is replaced by the discrete variable p and the integral by a sum

$$\rho[k] = C \left| \frac{1}{M-n} \sum_{n=1}^{M-n} \left(\sum_{p=1}^N i_n[p]i_{n+k}^*[p] \right) \right|. \quad (6)$$

N is the total number of array elements and M is the total number of sources used. Correlation distance ρ_d is defined as the distance between two sources at which the correlation coefficient ρ drops to 0.5. Equation (6) can be written as a Hermitian inner product:

$$\rho[k] = C \left| \frac{1}{M-n} \sum_{n=1}^{M-n} i_n i_{n+k}^H \right|. \quad (7)$$

Because the measured radiation field (3) and the complex image (4) are a Fourier pair, it is not surprising that complex image correlation is identical to wavefront correlation. This is shown in Appendix A, namely, that

$$\begin{aligned} \rho[k] &= C \left| \frac{1}{M-n} \sum_{n=1}^{M-n} i_n i_{n+k}^H \right| \\ &= C \left| \frac{1}{M-n} \sum_{n=1}^{M-n} \int \hat{s}_n(u) \hat{s}_{n+k}^*(u) du \right|. \end{aligned} \quad (8)$$

II. EXPERIMENTAL METHOD

The experiment was designed to measure the wavefronts radiating from a sequence of single sources through the female breast. The measured wavefronts are first focused on their sources. Then Fourier transformations yield complex images of the sources. From either the images or the focused wavefronts, correlation coefficients can be calculated and the correlation distance estimated.

A. Complex wavefront measurements

Measurements were made using the procedure given in Ref. 20 and summarized here for convenience. A single transducer element in the transmitting array radiates ultrasonic waves through the breast to a linear receiving array at

a distance of 120 mm. The transmitting frequencies were 3 and 4 MHz. The width of the source T was 1.49 mm and the beamwidths λ/T were approximately 0.5 and 0.4 rad at these frequencies. The receiving element spacing was 1.5 mm. Element height was 10 mm. Sixty-four elements extending over 96 mm formed the receiving array. Transmission was a sequence of 64, 16- μ s pulses spaced by 200 μ s. The transmitter voltage was controllable from 0 to 50 V. Reception across the entire array was by synthetic aperture. At each receiving element, the received rf pulses, after propagating through the medium, were coherently demodulated by multiplication with an internal oscillator. The analog in-phase and quadrature values were integrated for 18 μ s and digitized by 8-bit A/D converters. In this way the complex wavefront across the receiving aperture was measured. A total of 64 complex values is called a single source profile (SSP). The acquisition time per SSP is $200 \times 64 \mu\text{s} = 0.0128$ s. Three SSP measurements were averaged to increase the signal-to-noise ratio (SNR). So as to measure the wavefront distortion properties through various angular sectors of the breast, an SSP was obtained for each of 38 adjacent transmitter elements located in the middle region of the transmitting array. The total data-acquisition time of a set of 38 SSPs was $38 \times 3 \times 0.0128 \text{ s} = 1.46$ s. A second set of transmissions from each site immediately followed to assess possible subject motion during the measurement. The second set was sparse to reduce the data-acquisition time. The result is discussed in Sec. IV C.

For the bulk of the measurements the spectral width of the signal was about 60 kHz. This narrow-band waveform avoided any frequency selective effects upon wavefront distortion. Many 1-MHz bandwidth measurements were also made, using a 1- μ s short pulse and 1- μ s receiving window, so as to test the effect of pulse-length-dependent multipath upon the complexity of the wavefront. No significant difference was observed between narrow-band and wideband measurements.⁴

For the wideband experiment, one SSP was obtained from each of nine transmitters located in the middle of the transmitting array. Because the speed of sound was uncertain, 18 of these sequences were repeated to ensure reception in at least one of the 1- μ s receiving windows. The total data-acquisition time for nine wideband SSPs is $9 \times 0.0128 \mu\text{s} = 0.1152 \mu\text{s}$.

A stepping motor was used to translate the transducer assembly in the elevation direction. The intervals were either 1/2 or 1 cm. At each level, the data-taking sequence described above was repeated. The female breast was inserted into the reservoir between the source and the array. Baby oil [sound speed 1430 m s⁻¹ (see Ref. 22)] was used for the reservoir liquid to match the speed of sound of subcutaneous fat (1440 m s⁻¹) and consequently to reduce refraction at the skin surface. The same sequence of SSPs through oil alone was also taken for each experiment for system calibration and focusing.

B. Near-field focusing of wavefront and image formation

Wavefronts (SSPs) were measured for each near-field source through oil and tissue. The focusing vector w_f was the conjugate of the phase profile measured through oil. w_f contains the near-field geometry of the source as well as system errors which arise from geometrical and electrical errors in array elements and circuitry. Thus the SSPs used in the correlation experiments were not only focused but were free of all system errors. Fourier transforms of the focused SSPs are the complex source images.

Figure 3 shows measured wavefronts (SSPs) and images of single sources through oil (dashed) and through breast ID 55L. Amplitude profiles, which are wavefront moduli, are shown in (a). The oil profile is smooth and shows the far-field diffraction pattern of the transducer element, while the tissue profile is jagged and has nulls in the high-energy region which are likely to have been caused by phase cancellations. (b) shows the phase profiles, unwrapped to show their difference. The quadratic phase profile through oil reflects the near-field curvature of the transmitter relative to the receiving array, while the phase profile through tissue contains linear components (steering factor), superimposed on the near-field curvature, and perturbations. Focusing the array through oil is equivalent to subtracting the oil phase from the oil SSP, a procedure called phase conjugation. The images shown in (c) and (d) are moduli of the complex oil images. Because of the diffraction pattern of the source, the wavefront across the receiving aperture is tapered. As a result, the oil images show very low sidelobe levels. On the average, the peak sidelobe level is less than -31 dB and the average background level is less than -38 dB.²⁰ Focusing through tissue is accomplished by subtracting the oil phase from the tissue phase; the phase difference is due to the intervening tissue. The image is the modulus of the Fourier transform of the focused tissue data. Images through tissue of two adjacent transmitting elements (1.5-mm separation) are shown in (c) and (d) (solid). Both are badly distorted, which implies that focusing is not achieved. The oil images (dashed) are almost the same while the tissue images are only slightly similar. The difference is attributable to the different angular impulse responses of adjacent angular sectors in the breast.

C. Volunteer selection

Forty-three volunteers were measured at the Hospital of the University of Pennsylvania (HUP). One-third were x-ray mammography patients and two-thirds were hospital staff who had x-ray mammography during the experimental period. A consent form was signed by each volunteer. Of the 43 women, 22 (44 breasts) were selected for the correlation study. Selection was based on breast size. Large breasts both in length and in cross section were chosen to ensure good contact between transducers and tissue. This choice minimized the effect of refraction due to breast curvature (Sec. IV D).

Fourteen of the women were premenopausal and eight were postmenopausal. The former were further categorized

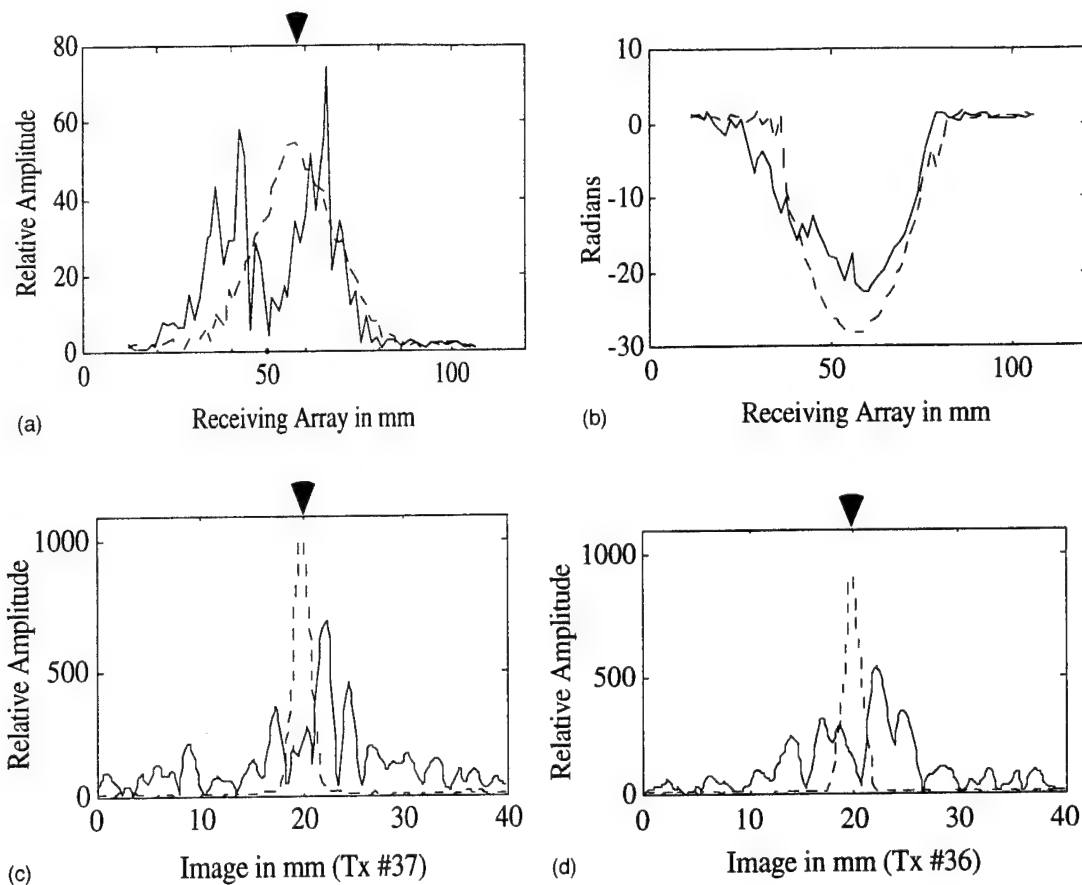


FIG. 3. Oil and tissue wavefront profiles and images of two adjacent sources spaced by 1.5 mm. 9.6-cm receiving array. 3-MHz transmitting frequency. The source direction is indicated by arrows. Tissue propagation path length is 12 cm. Path is through an extremely large breast, ID 55L, at approximately 3 cm from the chest wall. (a) Amplitude profiles received through oil (dashed) and breast. (b) Unwrapped phase profiles received through oil (dashed) and breast. (c) Images of transmitter element 37 through oil (dashed) and through breast. (d) Images of adjacent element 36 through oil (dashed) and breast. The dissimilarity between the two breast images is evident.

as premenopausal dense (7) and premenopausal fatty (7), based upon whether glandular tissue or fat predominated. Glandular tissue and fat are the two primary components of the female breast. The former is acoustically more heterogeneous than the latter.²³ Thus the image quality for a breast with a significant amount of glandular tissue is generally poor, especially when the wavefront is viewed by a large receiving array. Such a breast is clinically called a dense breast; it often occurs in premenopausal women who have few or no children.²⁴ Determination of the category was based on x-ray mammogram readings.

The average ages of the premenopausal dense, premenopausal fatty, and postmenopausal groups were 38.7, 48.3, and 57 yr.

III. EXPERIMENTAL RESULTS

A. Examples of cf and correlation distance

Figure 4 shows a cf of complex wavefront measurements obtained from a premenopausal dense breast at 3 MHz and also from the oil bath without the breast. The breast propagation path is approximately 2.5 cm below the chest wall. The correlation distance ρ_d is about 2.2 mm, while for oil it is 20 mm, and the correlation remains close to unity for about 6 mm. Because the oil correlation is essentially unity

in the 3- to 4-mm region where ρ_d is measured for breast, we can assume that the measurement is a good estimate of the actual correlation distance. Figure 5 shows breast cfs obtained from a postmenopausal breast at 3 and 4 MHz. ρ_d is 4.0 and 3.0 mm, respectively. The oil correlation distances are 20 and 16 mm. Again the measured ρ_d values in breast are sufficiently smaller than the oil measurements to be considered realistic estimates.

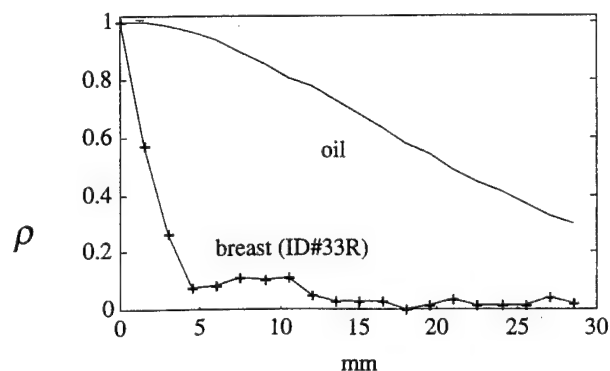


FIG. 4. Correlation function of wavefront obtained at 3 MHz through a breast slice approximately 3 cm below the chest wall of premenopausal breast ID 33R. The correlation distance is about 2.2 mm. Oil cf is also shown.

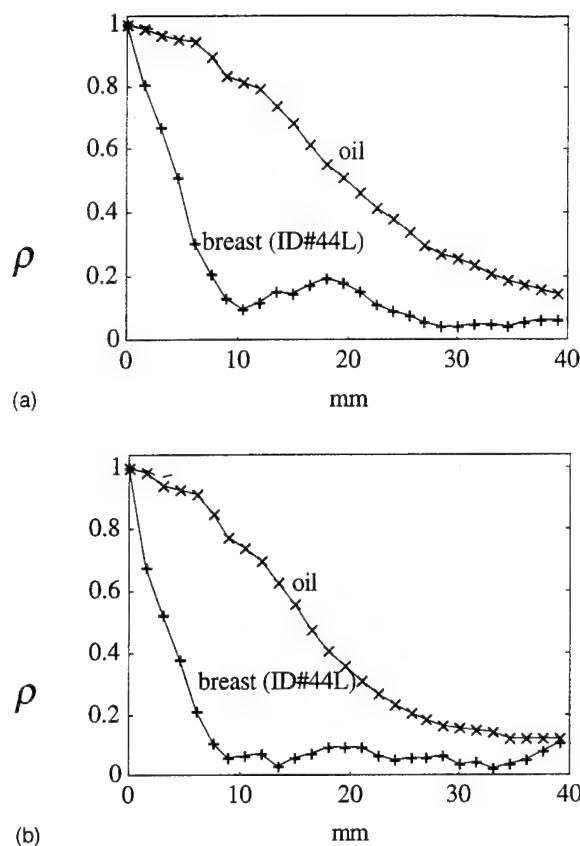


FIG. 5. cfs of postmenopausal breast ID 44L approximately 2.5 cm below the chest wall, and of oil. (a) 3 MHz, $\rho_d = 4.0$ mm. (b) 4 MHz, $\rho_d = 3.0$ mm.

B. Statistics of cf and correlation distance

Composite cfs of the three groups are given in Fig. 6. The sample sizes of the composite curves are 35, 52, and 56. Standard deviations are shown by error bars. The average ρ_d for the premenopausal dense breast is less than 1.5 mm, and is 2.4 and 1.9 mm for premenopausal fatty and postmenopausal breasts. Table I summarizes the composite data.

Statistics of 184 correlation distances versus distance of the propagation path from the chest wall, obtained from 44 breasts at 3 MHz, are given in Table II. Column 1 lists the subject's ID number (L for left breast, R for right). Age, menopausal status, type of breast, and average sample size are given in column 2. Columns 3–7 list measured values of ρ_d for paths from 2 to 4 cm below the chest wall. The average ρ_d and standard deviation for each breast are given in columns 8 and 9. Table III shows the mean correlation distances and standard deviations of the three populations.

The average correlation distance at 4 MHz is about 1/2 as large. Some selection was required to estimate this decrease. Because of the higher tissue attenuation at 4 MHz, we had inadequate signal strength for most of the premenopausal dense breasts and some of the premenopausal fatty and postmenopausal breasts. We selected ten breasts (five women) with good 4-MHz data and with higher than average correlation distance at 3 MHz for measurement and comparison. Table IV shows the data. The average ratio of average ρ_d at 3–4 MHz is 1.9 with 0.53 standard deviation.

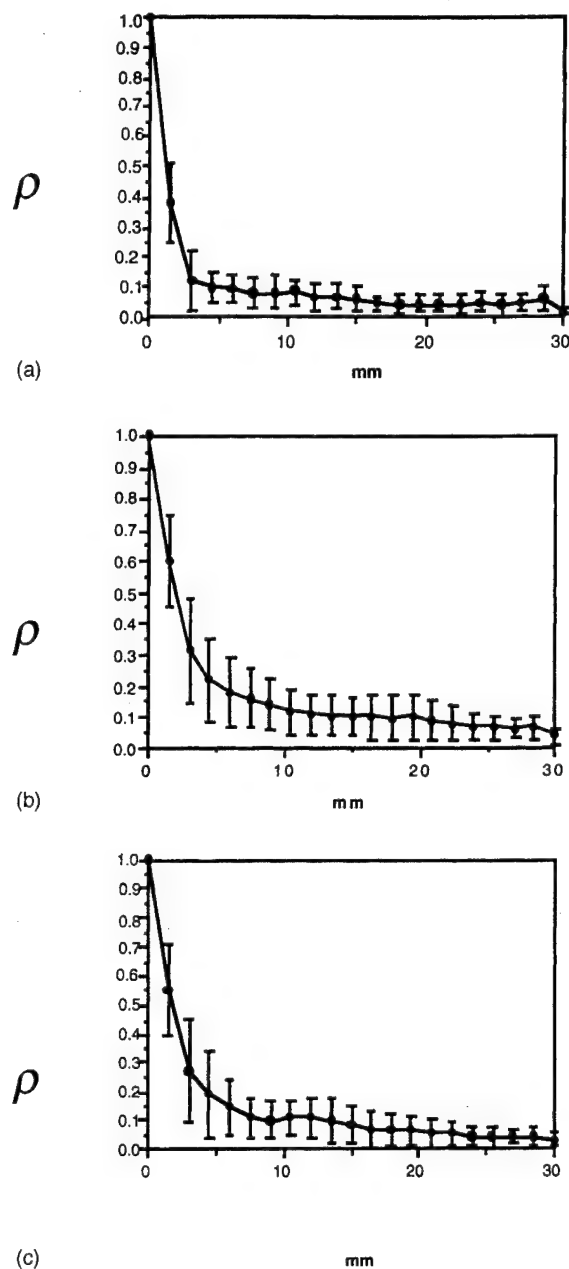


FIG. 6. Composite cfs of 3-MHz wavefronts obtained from (a) premenopausal dense, (b) premenopausal fatty, and (c) postmenopausal groups. 12-cm propagation path.

C. Comparison of narrow-band and wideband cfs

Composite cfs of complex wavefronts obtained from both narrow-band and wideband measurements at 3 MHz are shown in Fig. 7. Four large premenopausal fatty breasts are used for the comparison. All composites are formed from 9 cfs, each of which is calculated from 9 SSPs. cfs of oil are

TABLE I. Correlation distances of composite cfs (Fig. 6) of three subpopulations at 3 MHz over 12-cm paths.

Category	ρ_d (mm)
Premenopausal dense	<1.5
Premenopausal fatty	2.4
Postmenopausal	1.9

TABLE II. Statistics of breast correlation distance at 3 MHz over 12-cm path length.

ID number	Age, menopausal status, and type of breast, sample size ^a		Approximate distance from the chest wall					Average correlation distance ^b	Standard deviation
			2.0 cm	2.5 cm	3.0 cm	3.5 cm	4.0 cm		
ID 33L	36, pre-dense	(17)	0.9* ^c	0.95*	1.1	1.3	1.3	1.2	0.12
R		(17)	1.6	1.5*	1.7	1.6*	1.2*	1.7	0.07
ID 34L	38, pre-dense	(17)	1.0	1.2*	1.2*	1.1	1.1	1.1	0.06
R		(24)	2.2	2.1	2.4	2.0	1.5	2.0	0.34
ID 35L	43, pre-dense	(17)	1.1*	1.0*	1.0	1.0*	1.1	1.1	0.07
R		(17)	1.3*	1.0	1.1*	1.0*	1.1	1.1	0.07
ID 36L	39, pre-dense	(17)	1.0	1.1*	1.1*	1.1*	1.1	1.1	0.07
R		(17)	1.0*	1.1*	1.0*	1.1	1.1	1.1	0.0
ID 37L	36, pre-dense	(27)	1.1*	1.2*	1.1	1.3*	1.6*	1.1	0.0
R		(27)	1.1*	1.2	1.0	0.9	1.1	1.1	0.13
ID 46L	38, pre-dense	(17)	1.4*	1.3*	1.1	1.0		1.1	0.07
R		(17)	1.3	1.2	1.5			1.3	0.15
ID 60L	41, pre-dense	(17)	1.3		1.5*		0.9*	1.3	0.0
R		(17)	1.3		1.5		1.7	1.5	0.20
ID 32L	56, pre-fatty	(17)	1.4	1.4	1.4	1.5	1.9	1.5	0.22
R		(17)	2.4	1.9	2.4	1.7	2.3	2.1	0.32
ID 40L	38, pre-fatty	(27)	2.4	2.1	2.5	1.6	1.7	2.1	0.40
R		(27)	2.6	2.4	2.4	2.4	2.1	2.4	0.18
ID 48L	50, pre-fatty	(15)	1.2	0.9*	0.9	1.1	1.1*	1.1	0.15
R		(17)	1.3	1.3	1.0*	1.1*		1.3	0.0
ID 52L	50, pre-fatty	(17)	4.1*	2.2	1.6	1.7	2.1*	1.8	0.32
R		(17)	4.0	4.4*	4.5	4.4	5.1*	4.3	0.26
ID 55L	52, pre-fatty	(17)	2.6	2.1	2.1	1.4*	2.1	2.2	0.25
R		(27)	4.1	4.4	4.5	2.4	2.5	3.6	1.04
ID 66L	49, pre-fatty	(17)	1.8		1.3		1.3	1.5	0.29
R		(17)	1.3		1.3		1.9	1.5	0.35
ID 67L	43, pre-fatty	(17)	2.0		1.9		1.9	1.9	0.06
R		(17)	4.2		2.5		3.0	3.2	0.87
ID 44L	67, post-	(17)	3.6	4.5	4.6	2.9	2.9	3.7	0.83
R		(17)	2.9	3.2	4.6	4.9	5.2	4.2	1.04
ID 49L	68, post-	(15)	1.1	1.3	1.5*	1.7	1.6	1.4	0.28
R		(17)	1.9	1.5	2.1	2.5	2.4*	2.0	0.42
ID 50L	53, post-	(17)	1.8	1.2	1.8	1.4	1.2	1.5	0.30
R		(17)	1.0	1.1	1.1	1.5	1.7	1.3	0.30
ID 56L	61, post-	(15)	1.4	2.0	1.3			1.6	0.38
R		(21)	1.3	1.3	1.2			1.3	0.06
ID 58L	50, post-	(22)	1.2*		4.2		3.0	3.6	0.85
R		(21)	2.1		2.1		2.2	2.1	0.06
ID 64L	49, post-	(24)	1.2		1.3		2.6	1.7	0.78
R		(26)	1.3		1.4		2.6	1.8	0.72
ID 69L	50, post-	(22)	1.5		1.5		1.7	1.6	0.12
R		(20)	1.2		1.7		1.5	1.5	0.25
ID 71L	58, post-	(17)	1.9*		1.5		1.3	1.4	0.14
R		(17)	2.1		2.2		1.1	1.8	0.61

^aAverage sample size per elevation level. In general the number of samples at 2 cm is 1–3 larger than at 4 cm.

^bThese data are not corrected for subject motion, which was found to be significant (0.3 mm) only for prefatty breast (see Sec. IV C).

^cThe asterisk indicates that this value of ρ_d is not included in the calculation of the average correlation distance (column 8) because the phase variation caused by subject motion exceeds 0.3 rad (discussed in Sec. IV C).

shown for comparison. Geometric focusing based on constant speed (1430 m s^{-1}) is used for the wideband case. The cfs are similar. Both ρ_d 's are 2.0 mm. This implies that the complexities of the wavefronts received within the 18- μs window (from the 16- μs pulse) and the 1- μs window (from the 1- μs pulse) do not differ significantly. The conclusion is that the long transmitting pulse and long receiving window used for most of the experimental work had little if any effect upon the correlation distance measurements.

TABLE III. Mean correlation distances and standard deviations of three subpopulations at 3 MHz over 12-cm paths. Data from Table II. Premenopausal fatty mean value corrected for subject motion.

	Mean (mm)	Standard deviation (mm)
Premenopausal dense	1.2	0.27
Premenopausal fatty	2.5	0.93
Postmenopausal	2.0	0.93

TABLE IV. Statistics of breast correlation distance at 3 and 4 MHz over 12-cm path length.

ID number	Average correlation distance (mm) and standard deviation	
	3 MHz	4 MHz
ID 44L	3.7(0.83)	2.1(0.81)
ID 44R	4.2(1.04)	2.0(0.75)
ID 52L	1.8(0.32)	1.5(0.54)
ID 52R	4.3(0.26)	1.5(0.13)
ID 55L	2.5(0.37)	1.8(0.53)
ID 55R	3.6(1.04)	1.8(0.44)
ID 58L	3.6(0.85)	2.0(0.50)
ID 58R	2.1(0.06)	1.1(0.12)
ID 67L	1.9(0.15)	1.3(0.07)
ID 67R	3.7(1.84)	1.4(0.28)

IV. MEASUREMENT QUALITY

A. Correlation procedure

In the theory of Sec. I A, isotropic transmit and receive elements were implicitly assumed. The measured signal

strength at each element $i_n[p]$, however, included a transmit-receive pattern-gain product G_{np} . An example of this function is the single-element pattern shown in Fig. 3(a) (dashed). The correlation distances reported in this paper are not affected by G_{np} because correlation coefficients in water are close to unity for approximately 6 mm while correlation distances are less than 4 mm in all tissue cfs. The same process appears to be the case for cfs (e.g., Figs. 4–7) which extend considerably beyond 4 mm and hence their measurements could be affected by G_{np} . However, deconvolution of a tissue cf by its water cf shows that the effect is insignificant. The reason is that the tissue cf drops to 0.1–0.2 within 8–10 mm and deconvolution only increases it by 2%–8%, which will not change the cf significantly.

B. System noise

The fact that the composite cfs in Fig. 6 become very small within a few mm raises a question about the effect of noise in the measurements. Uncorrelated noise, in principle, could partially contribute to the precipitous drop of the correlation within a few sample points, because the zero-lag correlation coefficient is the sum of the signal and noise powers. To assess this possibility, SNRs were evaluated for the three breast groupings. SNR was calculated as the ratio of the product of the mean signal power and the length of the signal region to the product of the mean noise power and that portion of the length of the receiving aperture in a SSP that was free of signal. Thus the mean noise power was calculated outside the signal region. The average SNR values are 12.9, 16.4, and 14.3 dB for the three groups, respectively. The standard deviations are 3.7, 3.9, and 3.6 dB. The numbers of SSPs used were 173, 397, and 347. The SSPs were randomly selected from the 2752 available SSPs used to calculate cfs. The average SNR measurements indicate that noise contributes 4.9%, 2.2%, and 3.6% to the zero-lag correlation coefficients of the three groups and hence does not materially affect the measured cfs.

Cross-talk measurements were made between adjacent elements when one was transmitting and all others were receiving.²⁵ The level was found to be in the noise and therefore insignificant.

C. Subject motion

The experiment was designed to minimize the effect of subject motion upon the cf measurement. A sparse set of 38 transmissions/receptions was taken immediately after each 38-SSP set. This data set was compared with a subset of the 38-SSP set obtained from the same propagation paths. The standard deviations of the amplitude and phase differences of the pair of data sets were calculated. 2π jumps in the phase difference were removed. Because of the central role that phase plays in imaging, the standard deviation of the phase difference was the measure used to determine whether or not subject motion affected the measurements. When the rms phase difference exceeded 0.3 rad the data were discarded. The remainder were used to calculate the average correlation curves of Fig. 6 and the average correlation distance of Table

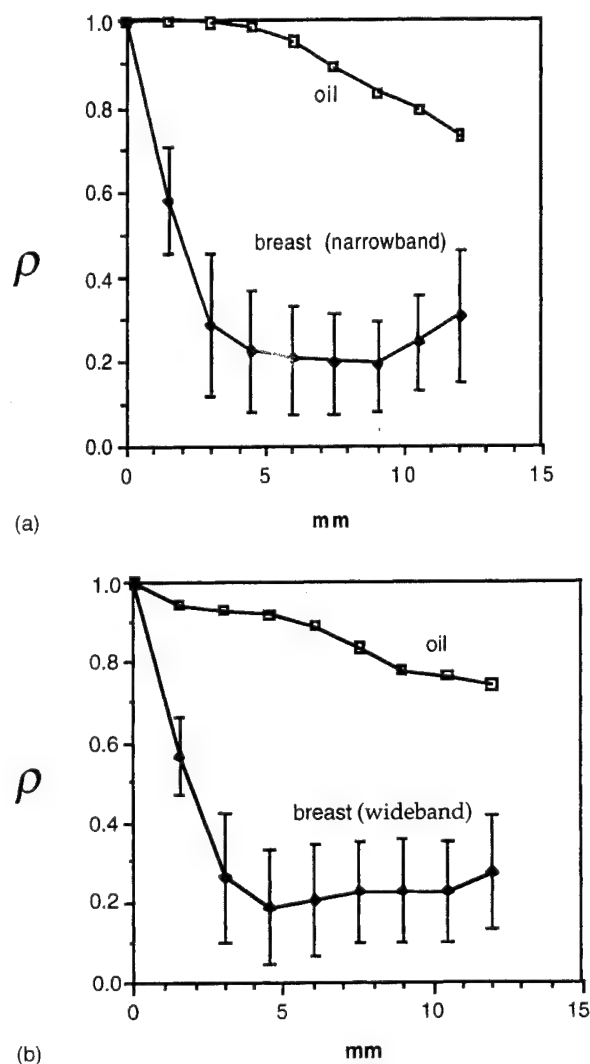


FIG. 7. Comparison of (a) wideband and (b) narrow-band cfs at 3 MHz. Wavefronts obtained from four large premenopausal fatty breasts.

TABLE V. Standard deviations of phase and amplitude differences of pairs of data sets.

	Phase (rad) Standard deviation (rad)	Amplitude Standard deviation
Predense	0.235	0.15
Prefatty and post-	0.167	0.1

II, column 8. Average standard deviations of phase and amplitude differences of the three groups are given in Table V.

To assess the residual effect of subject motion upon correlation distance we compared first and second lag correlation measurements with special measurements of $\rho[1]$ and $\rho[2]$ for which the data were taken over intervals too small (25 and 66 ms) for motion to be a concern. These $\rho[1]$ and $\rho[2]$ standards were estimated by using two SSPs obtained from two adjacent sources and two of every other source, respectively. The data-acquisition time for standard $\rho[1]$ is 25 μ s if the last repeated SSP of one source and the first repeated SSP of the next adjacent source are used, while acquisition time for standard $\rho[2]$ is 66 μ s. Thus the effect of subject motion upon these standard $\rho[1]$ and $\rho[2]$ is negligible. Pairs of SSPs of two adjacent sources and of every other source were randomly selected for each population to measure $\rho[1]$ and $\rho[2]$. Figure 8 shows these standard values (labeled motion-free) and the first two correlation coefficients obtained from composite cfs (labeled possible motion) for the three groups. ρ_d is unchanged for the first and third groups, but reduced by 0.3 mm for the second group. The values of ρ_d in Tables I and III for the premenopausal fatty group indicate a correction of this amount.

D. Liquid path versus contact measurements

To ensure good contact between transducers and breast for the purpose of reducing refraction at the skin surface,

three efforts were made. First, to minimize refraction at the subcutaneous fat and glandular tissue interface, we selected large breasts which filled almost the entire reservoir, and we instructed all volunteers to push their breasts against the transmitting array to partially flatten one side of the breast. The result was that the breasts were partially flattened against both transducer arrays. This insured high quality measurement, particularly near the chest wall where the breast cross section is largest. The possibility existed that the quality of the measurement degraded away from the chest wall where the cross section was smaller. Observations show no significant change in the correlation distance when the sampled level varies from 2 to 4 cm for 42 breasts. Only two exceptions were found. Thus, generally speaking, the correlation measurement is not degraded by the liquid bath assembly. Additional evidence is that among the 44 large breasts selected, 6 breasts are extremely large, for their breasts barely fit into the reservoir. These breasts belong to the premenopausal fatty group. No significant difference in correlation distance was found between these six breasts and the rest of the premenopausal fatty breasts.

Second, we used baby oil instead of water to match the speed of subcutaneous fat so as to minimize refraction at the interface between the liquid and the breast. The effect of matching is very difficult to quantify because it depends upon the thickness of subcutaneous fat layer, which is a variable from breast to breast. In general, premenopausal fatty and postmenopausal breasts have significant amounts of subcutaneous fat and matching to oil results in lower sidelobe levels, as compared with water-path matching, while premenopausal dense breasts have very thin layers of subcutaneous fat and oil matching does not help much.

Third, the transmitters used were selected from the middle elements of the transmitting array to ensure close to normal incidence of the ultrasonic rays at the skin surface.

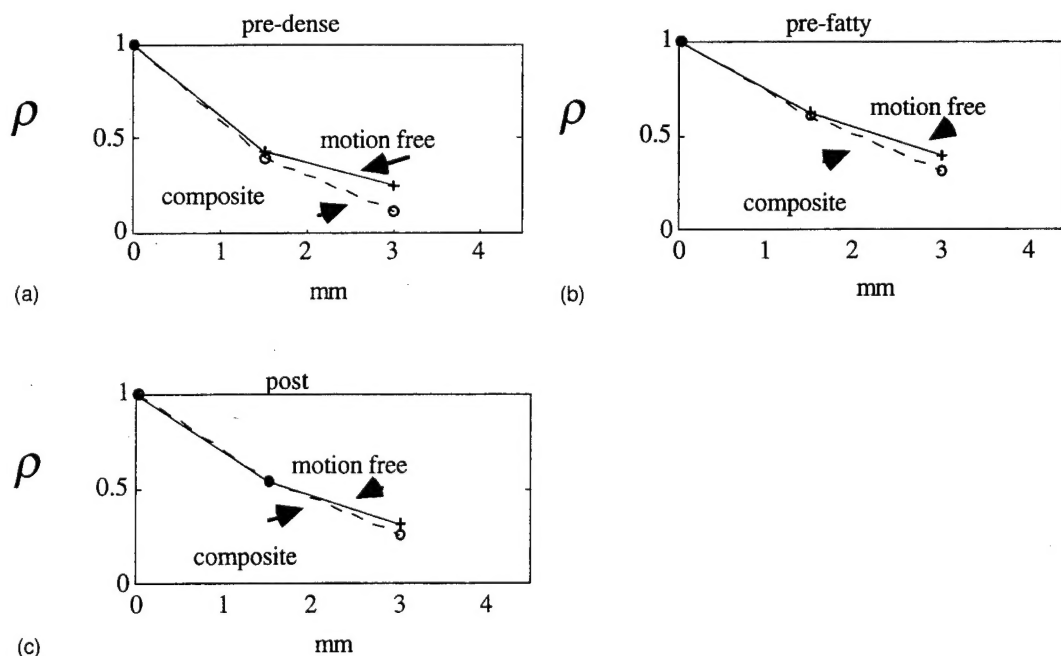


FIG. 8. Test for possible motion effect in cfs. Comparison of motion free $\rho[1]$ and $\rho[2]$ with first two correlation coefficients of composite cfs of Fig. 6.

Because of the general shape of the breast, wavefronts measured from relatively lateral sources sometimes have curvatures associated with non-normal incidence. Decorrelation of wavefronts due to this phenomenon was minimized by the procedure used.

In conclusion, the correlation results, we believe, can be used to predict correlation in semicontact but not in a compressed environment.

E. 1-D vs 2-D measurement

Our measurements were made with a 1-D array having a typical elevation dimension of 10 mm. Thus the results given in this paper are generally relevant to 1-D large-aperture echo scanning.

The only published data on the effect of integration over elevation upon wavefront measurement is in Ref. 26. In Ref. 26, arrival time and energy level fluctuations of wavefronts in 1-D and 2-D apertures have been compared by using measurements of abdominal wall transmission data in a large 2-D aperture and, from them, emulating measurements in a 1-D aperture to study the effects of spatial averaging in elevation. The authors found that integration reduces arrival time and energy level fluctuations by an average of 18% and 29% for an elevation of 11.5 mm and 47% and 50% for an elevation of 46.1 mm. The implication is that correlation distances with a large 2-D aperture will be smaller than those reported in this paper. However, the fact that Ref. 8 reports 2-D measurements on fatty breasts only 5% smaller on the average than those reported here indicates that the elevation integration effect on ρ_d may be small.

F. Path length

The propagation distance in the experiment was approximately 12 cm of tissue, which is an unusually long path length. Hence it is pertinent to assess the relevance of the ρ_d data reported in this paper to shorter distances. In an experimental paper by Hinkleman *et al.*,⁸ correlation distance was measured for several depths and found to be unrelated to propagation distance. Supporting this observation is a theoretical paper by Steinberg²⁷ on scattering in an inhomogeneous medium which predicts and explains this phenomenon. We conclude, therefore, that the long path length did not bias the results.

G. Effect of propagation speed used in focusing upon correlation measurements

Commercial scanners use 1540 m s^{-1} for focusing. Our data were focused with 1430 m s^{-1} (see Sec. II B). To address the question of how sensitive the cf measurement is to focusing speed, we measured cfs of 9 sets of wavefronts from four breasts with focusing speeds of 1500 and 1430 m s^{-1} . Wideband wavefronts were used. 1500 m s^{-1} is the measured average propagation speed of the breasts. The average cfs for the two focusing speeds are shown in Fig. 9. The curves are indistinguishable. Therefore, the correlation data from our experiment are also relevant for commercial scanners.

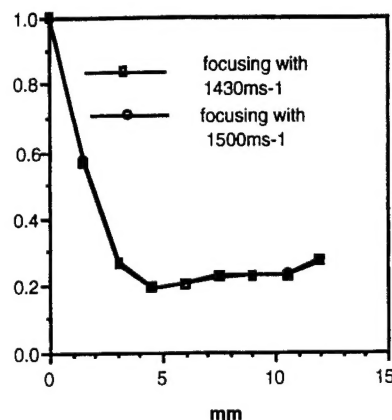


FIG. 9. Comparison of cfs with different focusing speeds. Averages of nine wideband measurements from four breasts.

V. COMPARISON WITH OTHER DATA

It is interesting to note that the reported data agree very well with the results obtained by Hinkelmann *et al.*⁸ (see the Introduction). Although the calculation procedures for obtaining the correlation functions were different, it is easy to show (Appendix B) that they are mathematically equivalent. Trahey *et al.*,^{5,6} however, removed linear (1-D) and planar (2-D) components from their time-of-flight data, a procedure that decreases the measured correlation distance. Consequently, it is impossible to make a direct comparison. It is also impossible to make a quantitative comparison with Durbin *et al.*⁷ (see the Introduction). This group reported grossly different correlations based on time of arrival measurements and on point spread functions calculated by detecting the maximum amplitude along the time axis. While interesting, these measurements bear little upon estimation of correlation distance. There are two reasons. First, time of arrival measurements ignore wavefront amplitude, which as we have demonstrated plays a highly significant role in the point spread function.^{20,21} Second, maximum projection is a nonlinear operation and therefore the correlation coefficient of point spread functions calculated from maximum projection has some unknown relation to correlation distance.

VI. SIGNIFICANCE OF CORRELATION DISTANCE MEASUREMENTS

Small correlation distance has significant impact upon wavefront deaberration algorithms.^{28,29} The area of the isoplanatic patch is about $4\rho_d\rho_d$, where the subscripts l and r distinguish between the correlation distance laterally and in range. On physical grounds $\rho_{d_l} = \rho_{d_r}$. Therefore the patch size is $4\rho_d^2$. A correction weight vector formed by an adaptive deaberration algorithm from data from some arbitrary location in the sector will compensate only for the wavefront distortion from an area ρ_d^2 in that neighborhood. A new or modified or updated vector will be required for all other such areas. Thus if A is the area of the scanning sector, the number of weight vectors to be calculated is $N_w = A/4\rho_d^2$. Assume, for example, that the imaging depth is 10 cm, the angular sector is 1 rad, and ρ_d is a few mm in both dimensions, as is reported in this paper; then N_w would be a few hundred.

Further, one subimage is calculated for each isoplanatic patch, using the compensating vector for that patch. These subimages must be combined coherently to build up a composite, high-resolution image of the sector. Thus the number of isoplanatic patches in the scanning sector of an imaging system is an important design parameter of adaptive wavefront deaberration algorithms for imaging system. If the number is small, adaptive wavefront deaberration is practical, whereas if it is large, the procedure may be too costly and time consuming.

VII. SUMMARY

Composite correlation functions of complex wavefronts are measured for 22 women who belong to three populations: premenopausal dense, premenopausal fatty, and postmenopausal breasts. A quantitative measure is the 50% correlation distance ρ_d which is half the FWHM of a cf. This information is valuable for image formation because it indicates how often the receiving weight vector has to be changed to incorporate the effects of changes in the propagation medium with scanning. The mean correlation distance of the complex wavefront is calculated for each of 44 breasts at 3 MHz. The average of the sample means of the first group is less than 1.5 mm, and are 2.5 and 2.0 mm for the later two groups, respectively. The standard deviations of the latter two groups are 0.93 and 0.93 mm. For ten premenopausal fatty and postmenopausal breasts at 4 MHz the mean and standard deviations are 1.6 and 0.34 mm. The average ratio of average correlation distance of complex wavefronts obtained at 3 and 4 MHz is 1.9 with 0.53 standard deviation. Thus, on the average, the correlation distance is reduced by a factor of 2 when the transmitting frequency is changed from 3 to 4 MHz.

ACKNOWLEDGMENTS

The authors wish to express sincere appreciation to all anonymous volunteers who have participated in this study, and to the Commonwealth of Pennsylvania, Interspec, Inc., an ultrasound imaging firm in Ambler, PA (now a division of ATL), the National Science Foundation (BCS92-09680), and the Army Medical Research and Development Command (DAMD) 17-93-J-3014 and DAMD 17-94-J-4133) for their funding of the work. Invaluable consultation was freely offered by Dr. Kai Thomenius, Director of Research of Interspec. The heart of the electronic system, a Vingmed SM-20, was donated by Interspec and the two linear arrays were given by Dr. Clyde Oakley, then Manager of R&D of Echo Ultrasound, Lewistown, PA, a division of Interspec. (Dr. Oakley is now with Tetrad Corp.) We are very grateful for the equipment contributions. Special thanks to Dr. Richard J. Pauls for his hardware design and construction of the experimental system used in the paper. The authors appreciate the administrative help of Bruce Carey, research coordinator, of the Department of Radiology of HUP.

APPENDIX A: EQUIVALENCE OF $\rho[k]$ DEFINED IN EQ. (7) AND CORRELATION COEFFICIENT OF COMPLEX IMAGE

The following derivations show that $\rho[k]$ defined in Eq. (7) is mathematically equivalent to the k th correlation coefficient of a complex image.

The Fourier transforms of sampled radiation fields, i_n and i_{n+k} , transmitted from sources n and $n+k$ are

$$\hat{s}_n(u) = \alpha_n \sum_{p'=1}^N \nu(p') m_{\theta_n}(p') \exp(jkp' du), \quad (A1)$$

$$\hat{s}_{n+k}(u) = \alpha_{n+k} \sum_{p=1}^N \nu(p) m_{n+k}(p) \exp(jkp du). \quad (A2)$$

The aperture weighting function $w(x)$ is chosen to be unity.

The k th correlation coefficient of the complex images is

$$\begin{aligned} & \int \hat{s}(u)_n \hat{s}(u)_{n+k}^* du \\ &= \alpha_n \alpha_{n+k} \sum_{p'=1}^N \nu(p') m_{\theta_n}(p') \\ & \quad \times \sum_{p=1}^N \nu^*(p) m_{\theta_{n+k}}^*(p) \int \exp\left(j \frac{2\pi}{\lambda} (p' - p) du\right) du. \end{aligned} \quad (A3)$$

The integral $\int \exp[j(2\pi/\lambda)(p' - p)du] du$ is a constant, denoted as c , when $p' = p$ and equals 0 when $p' \neq p$. Therefore

$$\begin{aligned} & \int \hat{s}(u)_n \hat{s}(u)_{n+k}^* du \\ &= c \alpha_n \alpha_{n+k} \sum_{p'=1}^N \nu(p') m_{\theta_n}(p') \nu^*(p') m_{\theta_{n+k}}^*(p'). \end{aligned} \quad (A4)$$

Since $i_n^H = \alpha_n \alpha_{n+k} \sum_{p'=1}^N \nu(p') m_{\theta_n}(p') \nu^*(p')$
 $\times m_{\theta_{n+k}}^*(p')$,

$$\int \hat{s}(u)_n \hat{s}(u)_{n+k}^* du = c i_n^H i_{n+k}.$$

Therefore Eq. (8) holds.

APPENDIX B: EQUIVALENCE OF cf DEFINED IN EQ. (7) AND SPATIAL CORRELATION OF ARRIVAL TIME FLUCTUATION

The following derivations show that cf defined in Eq. (7) is mathematically equivalent to the spatial correlation function of the complex wavefront, which is equivalent to spatial correlation of arrival time fluctuation.

Assuming that all i_n 's used to calculate $\rho[k]$ in Eq. (7) are from the same population, $\rho[k] = E[i_n^H i_{n+k}]$. Further assuming that components $i_n(p)$ of i_n and $i_{n+k}(p)$ of i_{n+k} are from the same population, $\rho[k]$ is then equal to $E[i_n^H i_{n+k}] = E[\sum_{p=1}^N i_n(p) i_{n+k}^*(p)] = E[i_n(p) i_{n+k}^*(p)]$, where p is the index of the receiver element. As shown in Fig. B1, $i_n(p) i_{n+k}^*(p)$ (right) is the dual measurement of $i_n(p) i_{n+k}^*(p + k)$ (left), when a single source radiates to the medium. Therefore, our correlation measurement is equivalent.

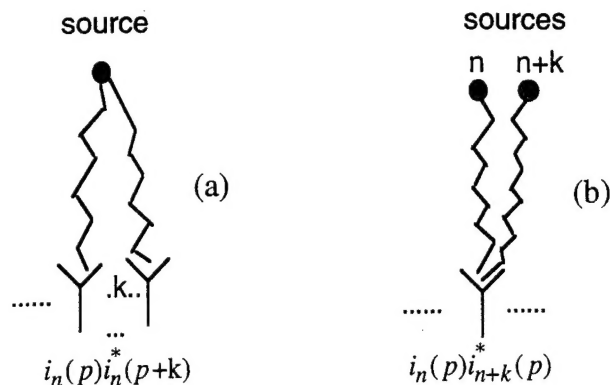


FIG. B1. (a) Wavefront correlation. Single source radiates through medium. cf of complex wavefront is estimated as an average of cross product of two signals received by two elements separated by k . (b) Two sources spaced by k radiate through medium. cf is the average of cross product of two signals received from two complex wavefronts at one element.

lent to the measurements reported by other groups where spatial correlation of arrival time fluctuation is used.

- ¹ F. S. Foster and J. W. Hunt, "Transmission of ultrasound beams through human tissue—Focusing and attenuation studies," *Ultrasound Med. Biol.* **3**, 257–268 (1979).
- ² M. Moshfeghi and R. C. Waag, "In vivo and in vitro ultrasound beam distortion measurements of a large aperture and a conventional aperture focused transducer," *Ultrasound Med. Biol.* **5**, 415–428 (1988).
- ³ Q. Zhu and B. D. Steinberg, "Large-transducer measurements of wavefront distortion in the female breast," *Ultrason. Imaging* **14**, 276–299 (1992).
- ⁴ Q. Zhu and B. D. Steinberg, "Wavefront amplitude distribution of the female breast," *J. Acoust. Soc. Am.* **96**, 1–9 (1994).
- ⁵ G. E. Trahey, P. D. Freiburger, L. F. Nock, and D. C. Sullivan, "In vivo measurements of ultrasonic beam distortion in the breast," *Ultrason. Imaging* **13**, 71–90 (1991).
- ⁶ P. D. Freiburger, D. C. Sullivan, B. H. LeBlanc, S. W. Swith, and G. E. Trahey, "Two dimensional ultrasonic beam distortion in the breast: In vivo measurements and effects," *Ultrason. Imaging* **14**, 398–414 (1992).
- ⁷ H. W. Durgin, P. D. Freiburger, D. C. Sullivan, and G. E. Trahey, "Large aperture phase error measurement and effects," *Proceedings of IEEE Ultrasonic Symposium* (IEEE, New York, 1992).
- ⁸ L. M. Hinkelman, D.-L. Liu, Q. Zhu, B. D. Steinberg, and R. C. Waag, "Measurement and correction of ultrasonic pulse distortion produced by the human breast," *J. Acoust. Soc. Am.* **97**, 1959–1969 (1995).
- ⁹ R. A. Muller and A. Buffington, "Real-time correction of atmospherically degraded telescope images through image sharpening," *J. Opt. Soc. Am.* **64**, 1200–1210 (1974).

- ¹⁰ B. D. Steinberg, "Radar imaging from a distorted array: The radio camera algorithm and experiments," *IEEE Trans. Antennas Propag.* **AP-29**, 740–748 (1981).
- ¹¹ A. C. S. Readhead, "Radio astronomy by very long baseline interferometry," *Sci. Am.* **53**–61 (1982).
- ¹² T. J. Cornwell, "The application of closure phase to astronomical imaging," *Science* **245**, 4915 (1989).
- ¹³ E. H. Attia and B. D. Steinberg, "Self-cohering large antenna arrays using the spatial correlation properties of radar clutter," *IEEE Trans. Antennas Propag.* **AP-37**, 30–38 (1989).
- ¹⁴ S. W. Flax and M. O'Donnell, "Phase aberration correction using signals from point reflectors and diffuse scatterers: Basic principles," *IEEE Trans. Ultrason. Ferroelectr. Freq. Control* **35**, 758–767 (1988).
- ¹⁵ L. Nock, G. E. Trahey, and S. W. Smith, "Phase aberration correction in medical ultrasound using speckle brightness as a quality factor," *J. Acoust. Soc. Am.* **85**, 1819–1833 (1989).
- ¹⁶ B. D. Steinberg and H. Subbaram, *Microwave Imaging Techniques* (Wiley, New York, 1991), Chaps. 8 and 9.
- ¹⁷ M. Fink, "Time reversal of ultrasonic fields—Part I: Basic principles," *IEEE Trans. Ultrason. Ferroelectr. Freq. Control* **39**, 555–566 (1992).
- ¹⁸ D.-L. Liu and R. C. Waag, "Correction of ultrasonic wavefront distortion using backpropagation and reference waveform method for time-shift compensation," *J. Acoust. Soc. Am.* **96**, 649–660 (1994).
- ¹⁹ B. D. Steinberg, "Self-calibration of large phased-array antennas for radar," *Int. J. Imaging Technol.* **4**, 275–284 (1992).
- ²⁰ Q. Zhu, B. D. Steinberg, and R. Arenson, "Wavefront amplitude distortion and image sidelobe levels—Part II: In vivo experiments," *IEEE Trans.*
- ²¹ Q. Zhu and B. D. Steinberg, "Wavefront amplitude distortion and image sidelobe levels—Parts I, Theory," *IEEE Trans. Ultrason. Ferroelectr. Freq. Control* **40**, 747–753 (1993); *Ultrason. Ferroelectr. Freq. Control* **40**, 754–762 (1993).
- ²² A. R. Selfridge, "Approximate material properties in isotropic materials," *IEEE Trans. Son. Ultrason.* **SU-32**, 381–394 (1985).
- ²³ F. S. Foster, M. Strban, and G. Austin, "The ultrasound macroscope: Initial studies of breast tissue," *Ultrason. Imaging* **6**, 243–261 (1984).
- ²⁴ G. Kossoff, E. K. Fry, and J. Jellins, "Average velocity of ultrasound in the human female breast," *J. Acoust. Soc. Am.* **53**, 1730–1736 (1973).
- ²⁵ R. J. Pauls, "Design of an ultrasonic experiment to measure wavefront distortion properties in soft tissue," Master thesis, University of Pennsylvania, The Moore School of Electrical Engineering, 1989.
- ²⁶ D.-L. Liu and R. C. Waag, "A comparison of wavefront distortion and compensation in one-dimensional and two-dimensional apertures," *IEEE Trans. Ultrason. Ferroelectr. Freq. Control* (in press).
- ²⁷ B. D. Steinberg, "Contrast and resolution as affected by scattering in homogeneous medium," *AIUM Proceedings*, 1994.
- ²⁸ B. D. Steinberg and A. K. Luthra, "A simple theory of the effects of medium turbulence upon scanning with an adaptive phased array," *J. Acoust. Soc. Am.* **71**, 630–634 (1982).
- ²⁹ B. D. Steinberg, *Microwave Imaging with Large Antenna Arrays: Radio Camera Principles and Techniques* (Wiley, New York, 1983), Chap. 3, pp. 213–231.